CERN-SPSC-2013-022 / SPSC-I-242
08/08/2013

Letter of Intent to the CERN SPSC

The International Axion Observatory
IAXO

IAXO Collaboration
August 7, 2013

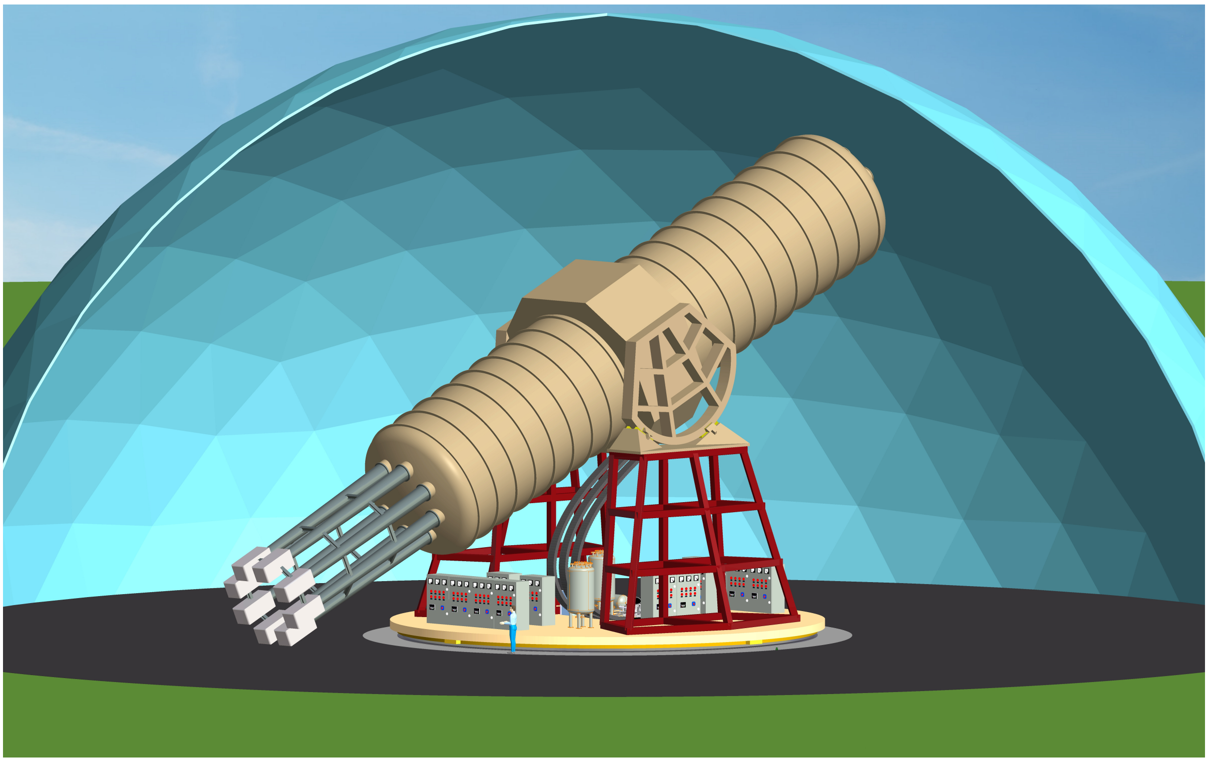

Letter of Intent to the CERN SPSC

The International Axion Observatory IAXO

E. Armengaud[1], F. T. Avignone[2], M. Betz[3], P. Brax[4], P. Brun[1], G. Cantatore[5], J. M. Carmona[6], G. P. Carosi[7], F. Caspers[3], S. Caspi[8], S. A. Cetin[9], D. Chelouche[10], F. E. Christensen[11], A. Dael[1], T. Dafni[6], M. Davenport[3], A.V. Derbin[12], K. Desch[13], A. Diago[6], B. Döbrich[14], I. Dratchnev[12], A. Dudarev[3], C. Eleftheriadis[15], G. Fanourakis[16], E. Ferrer-Ribas[1], J. Galán[1], J. A. García[6], J. G. Garza[6], T. Geralis[16], B. Gimeno[17], I. Giomataris[1], S. Gninenko[18], H. Gómez[6], D. González-Díaz[6], E. Guendelman[19], C. J. Hailey[20], T. Hiramatsu[21], D. H. H. Hoffmann[22], D. Horns[23], F. J. Iguaz[6], I. G. Irastorza[6,*], J. Isern[24], K. Imai[25], A. C. Jakobsen[11], J. Jaeckel[26], K. Jakovčić[27], J. Kaminski[13], M. Kawasaki[28], M. Karuza[29], M. Krčmar[27], K. Kousouris[3], C. Krieger[13], B. Lakić[27], O. Limousin[1], A. Lindner[14], A. Liolios[15], G. Luzón[6], S. Matsuki[30], V. N. Muratova[12], C. Nones[1], I. Ortega[6], T. Papaevangelou[1], M. J. Pivovaroff[7], G. Raffelt[31], J. Redondo[31], A. Ringwald[14], S. Russenschuck[3], J. Ruz[7], K. Saikawa[32], I. Savvidis[15], T. Sekiguchi[28], Y. K. Semertzidis[33], I. Shilon[3], P. Sikivie[34], H. Silva[3], H. ten Kate[3], A. Tomas[6], S. Troitsky[18], T. Vafeiadis[3], K. van Bibber[35], P. Vedrine[1], J. A. Villar[6], J. K. Vogel[7], L. Walckiers[3], A. Weltman[36], W. Wester[37], S. C. Yildiz[9], K. Zioutas[38]

[1]CEA Irfu, Centre de Saclay, F-91191 Gif-sur-Yvette, France

[2]Physics Department, University of South Carolina, Columbia, SC, USA

[3]European Organization for Nuclear Research (CERN), Genève, Switzerland

[4]IPHT, Centre d'Études de Saclay (CEA-Saclay), Gif-sur-Yvette, France

[5]Instituto Nazionale di Fisica Nucleare (INFN), Sezione di Trieste and Università di Trieste, Trieste, Italy

[6]Laboratorio de Física Nuclear y Altas Energías, Universidad de Zaragoza, Zaragoza, Spain

[7]Lawrence Livermore National Laboratory, Livermore, CA, USA

[8]Lawrence Berkeley National Laboratory, USA

[9]Dogus University, Istanbul, Turkey

[10]Physics Department, University of Haifa, Haifa, 31905 Israel

[11]Technical University of Denmark, DTU Space Kgs. Lyngby, Denmark

[12]St. Petersburg Nuclear Physics Institute, St. Petersburg, Russia

[13]Physikalisches Institut der Universität Bonn, Bonn, Germany

[14]Deutsches Elektronen-Synchrotron DESY, Hamburg, Germany

[15]Aristotle University of Thessaloniki, Thessaloniki, Greece

[16]National Center for Scientific Research "Demokritos", Athens, Greece

[*]Spokesperson. E-mail: irastorz@unizar.es

[17]Instituto de Ciencias de las Materiales, Universidad de Valencia, Valencia, Spain
[18]Institute for Nuclear Research (INR), Russian Academy of Sciences, Moscow, Russia
[19]Physics department, Ben Gurion Uiversity, Beer Sheva, Israel
[20]Columbia Astrophysics Laboratory, New York, USA
[21]Yukawa Institute for Theoretical Physics, Kyoto University, Kyoto, Japan
[22]Technische Universität Darmstadt, IKP, Darmstadt, Germany
[23]Institut für Experimentalphysik, Universität Hamburg, 22761 Hamburg, Germany
[24]Institut de Ciències de l'Espai (CSIC-IEEC), Facultat de Ciències, Campus UAB, Bellaterra, Spain
[25]Advanced Science Research Center, Japan Atomic Energy Agency, Tokai-mura, Ibaraki-ken, Japan
[26]Institut für theoretische Physik, Universität Heidelberg, Philosophenweg 16, 69120 Heidelberg, Germany
[27]Rudjer Bošković Institute, Zagreb, Croatia
[28]Institute for Cosmic Ray Research, University of Tokyo, Tokyo, Japan
[29]University of Rijeka, Croatia
[30]Research Center for Low Temperature and Materials Sciences, Kyoto University, Kyoto, 606-8502 Japan
[31]Max-Planck-Institut für Physik, Munich, Germany
[32]Department of Physics, Tokyo Institute of Technology, Tokyo, Japan
[33]Physics Department, Brookhaven National Lab, Upton, NY, USA
[34]Department of Physics, University of Florida, Gainesville, FL 32611, USA
[35]Department of Nuclear Engineering, University of California Berkeley, Berkeley, CA, USA
[36]University of Cape Town, South Africa
[37]Fermi National Accelerator Laboratory, Batavia, IL, USA
[38]Physics Department, University of Patras, Patras, Greece

Contents

1 Executive summary

Axions appear in very well motivated extensions of the Standard Model (SM) including the Peccei-Quinn mechanism proposed to solve the long-standing strong-CP problem. Together with the weakly interacting massive particles (WIMPs) of supersymmetric theories, axions are also a favored candidate to solve the Dark Matter (DM) problem. Their appeal comes from the fact that, like WIMPs, they are not an *ad hoc* solution to the DM problem. Mixed WIMP-axion DM is one possibility favored in some theories. More generic axion-like particles (ALPs) appear in diverse extensions of the SM (e.g., string theory). ALPs could also be the DM and are repeatedly invoked to explain some astrophysical observations.

For the time being, there is no hint of supersymmetry at the LHC, nor is there a clear signature of WIMPs in direct detection experiments. Progress is continuous, and in the next decade the WIMP hypothesis may be completely probed by direct WIMP detectors, combined with accelerators and indirect searches. These facts, taken together with recent advances in theory and phenomenology, make the search for axions increasingly compelling and timely.

The diverse experimental approaches to search for axions are complementary on many levels [1]. Among these approaches the axion helioscope stands out as the most mature, technologically feasible and capable of being scaled in size. The CERN Axion Solar Telescope (CAST) has been the third generation axion helioscope, and the first one to reach, and slightly surpass, the astrophysical limit on the axion-photon coupling $g_{a\gamma} \lesssim 10^{-10}$ GeV^{-1} in a wide mass range and to probe the ALP parameter space relevant for astrophysics.

This Letter of Intent (LoI) describes IAXO, the International Axion Observatory, a proposed 4th-generation axion helioscope. As its primary physics goal, IAXO will look for axions or ALPs originating in the Sun via the Primakoff conversion of the solar plasma photons. In terms of signal-to-background ratio, IAXO will be about **4−5 orders of magnitude more sensitive** than CAST, which translates into a factor of ∼20 in terms of the axion-photon coupling constant $g_{a\gamma}$. That is, this instrument will reach the few $\times 10^{-12}$ GeV^{-1} regime for a wide range of axion masses up to about 0.25 eV.

IAXO has potential for the discovery of axions and other ALPs, since it will deeply enter into completely unexplored parameter space. At the very least it will firmly exclude a huge region of this space. Needless to say, the discovery of such particles and the consequent evidence for physics at very high energy scales would be a groundbreaking result for particle physics.

IAXO follows the conceptual layout of an enhanced axion helioscope, in which all the magnet aperture is equipped with focusing optics. The stated sensitivity relies on the construction of a large superconducting 8-coil toroidal magnet optimized for axion research. Each of the eight 60 cm diameter magnet bores is equipped with x-ray optics focusing the signal photons into ∼0.2 cm^2 spots that are imaged by ultra-low background Micromegas x-ray detectors. The magnet will be built into a structure with elevation and azimuth drives that will allow solar tracking for ∼12 hours each day. All the enabling technologies for IAXO exist, there is no need for development. IAXO will also benefit from the invaluable expertise and knowledge gained from the successful operation of CAST for more than a decade.

More specifically, at high masses this experiment would explore a broad range of realistic axion models that accompany the Peccei-Quinn solution of the strong CP problem. Its sensitivity would cover axion models with masses down to the few meV range, superseding the SN 1987A energy loss limits on the axion mass. Axion models in this region are of high cosmological interest: they are favored dark matter candidates and could compose all or part of the cold dark matter of the Universe. In non-standard cosmological scenarios, or in more generic axion-like frameworks, the range of parameters of interest as dark matter (DM) is enlarged and most of the region at reach by IAXO contains possible DM candidates.

At much lower masses, below $\sim 10^{-7}$ eV, the region attainable by IAXO includes ALP parameters invoked repeatedly to explain anomalies in light propagation over astronomical distances. IAXO would provide a definitive test of this hypothesis.

Additional physics cases for IAXO include the possibility of detecting more specific models of axions or ALPs from the Sun. Most remarkable is the possibility to detect the flux of solar axions produced by axion-electron coupling g_{ae} induced phenomena. Although the existence of these production channels for standard axions is model-dependent, axions with a g_{ae} of few $\sim 10^{-13}$ have been invoked to solve the anomalous cooling observed in white dwarfs (WD). IAXO could be sensitive, for the first time, to the solar flux of axions produced by the very same mechanism invoked for WD, reaching g_{ae} values to test the hypothesis that the cooling of WD is enhanced by axion emission. Similarly IAXO will test models of other proposed particles at the low energy frontier of particle physics, like hidden photons, or chameleons, scalars with an environment-dependent mass proposed in the context of Dark Energy models, all of them potentially produced at the Sun. Although still at an early stage of theoretical development, it is intriguing that this type of setups could evolve into the first particle physics experiments directly testing Dark Energy. In addition, IAXO could directly detect relativistic axions/ALPs potentially composing the Dark Radiation for some relevant models. Finally, IAXO offers the possibility of implementing additional experimental programs, which effectively turn it into a multipurpose facility for generic axion and ALP research.

The physics potential of IAXO is highly complementary to the prospects of other axion/ALP search techniques, like haloscopes and light-shinning-through-wall (LSW) experiments. In particular, axion haloscopes (e.g., ADMX) enjoy high sensitivity but for a narrow mass range around a few μeV, assuming axions are the totality of the DM. The realistic prospects of both haloscopes at low masses and helioscopes at high masses still leaves a window at the sub meV level which is extremely challenging to explore experimentally and is highly motivated theoretically. New ideas are being put forward that could combine elements from both haloscopes and helioscopes (and other) searches. The IAXO magnet has been designed to easily accommodate new equipment (e.g., microwave cavities or antennas), and it is intriguing to consider that the facility constructed for IAXO could support axion searches using both the helioscope and haloscope techniques. This possibility is at an early stage of development, but has enormous potential, given the size and geometry of the IAXO magnet. The collaboration aims at consolidating a DM program with IAXO that could complement and extend the helioscope baseline program, and eventually access the remaining axion parameter space.

2 Physics case

2.1 The strong CP problem and axions

The recent likely discovery of the Higgs boson would complete the experimental confirmation of the particle content of the very successful Standard Model (SM) of particle physics. However, it is known that the SM is incomplete by itself, as it does not explain some basic features of our Universe (e.g., the nature of Dark Matter and Dark Energy, or the matter-antimatter unbalance), and does not provide satisfactory explanations for a number of parameters and facts of the SM itself. One of the latter is the so-called *strong-CP problem*, or why the strong interactions seem not to violate the charge-parity (CP) symmetry [2].

Indeed, the lagrangian of Quantum Chromodynamics (QCD) includes a CP-violating term:

$$\mathcal{L}_{\bar{\theta}} = \bar{\theta}\frac{\alpha_s}{8\pi}G^{\mu\nu a}\tilde{G}_{\mu\nu a} \tag{1}$$

where G is the gluon field and $\tilde{G}$ its dual, and α_s the strong coupling constant.

One of the experimental consequences of the term $\mathcal{L}_{\bar{\theta}}$ would be the existence of electric dipole moments (EDMs) for protons and neutrons. The non-observation of the neutron EDM [3] puts a very strong limit on the magnitude of the $\bar{\theta}$ parameter in (1) of about $|\bar{\theta}| \lesssim 10^{-10}$. But the problem is more than the unexplained smallness of an arbitrary SM parameter. The $\bar{\theta}$-angle is actually the sum of two contributions, which are in principle unrelated. The first is the angle characterizing the QCD vacuum and the second is the common phase of the matrix of SM quarks –coming from the Higgs Yukawa couplings which are known to violate CP sizeably. Thus, the smallness of $\bar{\theta}$ requires that two completely unrelated terms of the SM (from two different sectors) cancel each other with a precision of at least 10^{-10}. The strong CP problem constitutes a very serious fine-tuning issue that remains unexplained in the SM.

The most compelling solution of the strong CP problem is the Peccei-Quinn (PQ) mechanism, proposed in 1977 [4, 5]. It postulates a new U(1) global symmetry (the PQ symmetry) that is spontaneously broken at a high scale f_a. This implies the existence of a new field a which appears as the pseudo-Nambu-Goldstone boson of the new symmetry. This symmetry has to be exact at the classical level but broken by the color anomaly, i.e. by quantum effects. Therefore, the term $\mathcal{L}_{\bar{\theta}}$ ends up absorbed in a new term of the type $G^{\mu\nu}\tilde{G}_{\mu\nu}a/f_a$ where a is now a dynamical variable, which can relax to a CP-conserving minimum. This solves the fine-tuning problem dynamically, for any value of f_a. The main observational consequence of the PQ mechanism, as was first pointed out by Weinberg and Wilczek [6, 7], is that the quantum excitations of this field –albeit very weakly coupled– are potentially observable as new particles: axions.

The PQ mechanism fixes some of the properties of the axion [8, 9]. The most important is the axion mass m_a, acquired via mixing with the pseudoscalar mesons,

$$m_a \simeq \frac{m_\pi f_\pi}{f+a}\frac{\sqrt{m_u m_d}}{m_u + m_d} \simeq 6\,\mathrm{meV}\frac{10^9\ \mathrm{GeV}}{f_a} \tag{2}$$

where $m_\pi = 135$ MeV is the pion mass, $f_\pi \approx 92$ MeV the pion decay constant and $m_{u,d}$ the light quark masses. Model independently, axions interact with hadrons and photons via the same mixing. All the axion couplings are suppressed by the PQ symmetry scale f_a, which is not determined by theory.

More concrete axion properties depend on the specific implementation of the PQ symmetry and its relation with the SM fields. Originally it was identified with the weak scale, but accelerator data quickly ruled out this possibility constraining it to be higher than about 10^5 GeV. If the fermions of the SM do not have PQ charge, axions do not couple with them at tree level. These are called "hadronic axions", of which the KSVZ [10, 11] model is an often quoted example. Other models, like the DSFZ [12, 13], feature tree-level coupling with SM fermions, e.g., the axion electron coupling g_{ae}.

Axion coupling to photons

The most relevant for this proposal is the axion-two-photon coupling $g_{a\gamma}$

$$\mathcal{L}_{a\gamma} \equiv -\frac{g_{a\gamma}}{4} a F^{\mu\nu}\tilde{F}_{\mu\nu} = g_{a\gamma}\,\mathbf{E}\cdot\mathbf{B}\,a\,, \tag{3}$$

where F is the electromagnetic field-strength tensor and $\tilde{F}$ its dual, while $\mathbf{E}$ and $\mathbf{B}$ are the electric and magnetic fields. The coupling $g_{a\gamma}$ has units of energy^{-1}. It can be computed in any specific axion model as

$$g_{a\gamma} = \frac{\alpha}{2\pi f_a} C_\gamma, \quad ; \quad C_\gamma \equiv \frac{E}{N} - \frac{2}{3}\frac{4m_d + m_u}{m_d + m_u} \simeq \frac{E}{N} - 1.92 \tag{4}$$

The loop factor $\alpha/2\pi f_a$ reflects the fact that this is a coupling generated from the electromagnetic anomaly. C_γ is a coefficient of order 1 with two contributions: a model-independent one due to the axion mixing with pseudoscalar mesons and a model dependent one E/N which arises if the PQ symmetry is not only color-anomalous but also has a non-zero electromagnetic anomaly (E and N are the electromagnetic and color anomalies of the PQ symmetry). In general, a broad range of values for E/N is possible, depending of the axion model (e.g. for DFSZ $E/N = 8/3$ and $C_\gamma \simeq 0.75$, whereas for KSVZ $E/N = 0$ and $C_\gamma \simeq -1.92$, if the new heavy quarks are taken without electric charge).

Because the axion-photon interaction is generic and because photons offer many experimental options, most axion search strategies are based on this interaction. Axions mix with photons in the presence of external magnetic fields, leading to axion-photon oscillations [14, 15], similar to the well known neutrino oscillations, and to changes in the polarization state of photons propagating in a magnetic field [15, 16]. The $a\gamma\gamma$ coupling also leads to the Primakoff conversion of plasma photons into axions within stellar cores, the main axion emission channel of the Sun. The Primakoff conversion is also behind the detection principle of axion helioscopes, haloscopes [14] as well as LSW experiments, as discussed later on. The results of these searches are therefore represented in the parameter space ($g_{a\gamma}$,m_a) that is shown in Fig. 1. Because $g_{a\gamma}$ and m_a are linked for a specific axion model (both are inversely proportional to f_a), an axion model is represented by a straight diagonal line in such plot (the green line in Fig. 1 correspond to the KSVZ model). The overall spread of axion models resulting from the possible values of E/N in (4) is represented by the width of the yellow band of Fig. 1.

Axion coupling to electrons

In a very wide and interesting class of implementations of the PQ mechanism, the axion couples to leptons at tree level. This is most importantly the case of models in which the SM is embedded in a Grand Unified Theory, where color and electroweak interactions are unified in a larger non-abelian symmetry. This does not have to be the case, however, the original PQ model had coupling to electrons and aimed no grand unification. The coupling to electrons can be written in two forms, equivalent for our purposes,

$$\mathcal{L}_{ae} = C_{ae}\frac{\partial_\mu a}{f_a}\bar{\psi}_e\gamma^\mu\gamma^5\psi_e \leftrightarrow g_{ae}a\bar{\psi}_e\gamma^5\psi_e \tag{5}$$

where C_{ae} is again a coefficient of order 1 given by specifics of the model. The equivalent Yukawa coupling is $g_{ae} = C_{ae}m_e/f_a$ where m_e is the electron mass. For instance in the DSFZ model [12, 13] $C_{ae} = \frac{1}{3}\cos^2\beta$ where $\tan\beta$ is the ratio of the v.e.vs of the two Higgses present in the theory. When C_{ae} is zero at tree-level, a non-zero value is generated by radiative corrections, but being loop-suppressed is typically irrelevant.

The coupling to electrons drives the most efficient axion-production reactions in young stars when C_{ae} is $\mathcal{O}(1)$. This holds for the case of the Sun, low-mass red giants and white dwarf stars.

Summary of relevant constraints

Since it was first proposed, the axion has been thoroughly studied for its implications in astrophysics, cosmology and particle physics. The most relevant limits on its properties have been drawn from astrophysical considerations [17]. The emission of axions from the Sun is nowadays best constrained from the increase they imply in the solar neutrino flux with respect to the standard one without axions [18]. The axion flux originated from the Primakoff effect constrains the coupling $g_{a\gamma} \lesssim 0.7 \times 10^{-9}$ GeV^{-1} and the axio-Bremsstrahlung in electron collisions (and other reactions involving electrons) constrains $g_{ae} < 2.5 \times 10^{-11}$. The population of low-mass horizontal-branch (HB) stars and red-giants (RG) in globular clusters gets decreased and increased respectively when axions are freely emitted from their interiors. Fitting the observed population to numerical simulations one derives the limits $g_{a\gamma} \lesssim 10^{-10}$ GeV^{-1} (mostly from the impact on HBs) [17, 19] and $g_{ae} < 4.7 \times 10^{-13}$ at 95% C.L. (from the tip of the RG branch in the cluster M5) [20]. Recently, it has been argued that the Primakoff flux of axions from $g_{a\gamma} > 0.8 \times 10^{-10}$ GeV^{-1} will shorten so much the helium-burning phase (so called blue loop) of *massive stars* that Cepheids could not be observed [21], and thus it is excluded. Observations and theory of white dwarf cooling fit to the extent that they can exclude values of the electron coupling $g_{ae} > 3 \times 10^{-13}$ [22, 23, 24, 25]. However, as we shall comment later on, some observables such as the luminosity function and the period decrease of the variable ZZ Ceti star G117-B15A seem to prefer some slight extra cooling.

Axions couple to protons and nucleons via model-independent mixing with the pseudoscalar mesons. These couplings also receive model-dependent corrections of $\mathcal{O}(1)$ in different models. Due to these couplings, axions can be efficiently emitted from the core of a Type-II supernova shortening the neutrino pulse. From the observation of the $\sim$10 s duration neutrino burst of SN1987A, which fits the expectations without extra axion cooling, one can derive the limit to the axion-proton Yukawa-like coupling $g_{ap} \lesssim 10^{-9}$ [26]. In general we have $g_{ap} = C_{ap}m_p/f_a$. For hadronic axions $C_{ap} \sim 0.4$ and thus $f_a > 4.8 \times 10^8$ GeV or, equivalently, $m_a < 16$ meV. For DFSZ axions C_{ap} tends to be smaller and the constraints weaker, but not much because then the axion-neutron coupling becomes relevant. Similar bounds for $f_a \gtrsim 10^9$ GeV arise from neutron star cooling [27, 28]. Despite a lot of effort that has gone into understanding the axion emission rate, theoretical simulations and observations, these limits remain fairly rough estimates.

Other astrophysical, cosmological and experimental bounds, some of them commented on later, further constrain the allowed axion parameter space. However, not only have these bounds not rejected the axion, but the motivation for the existence of axions, beyond the strong CP problem, has grown on several fronts. The axion is a candidate for the dark matter of the Universe, and several tantalizing hints in astrophysics could be the result of axion-like particles at play. More recent theoretical advances are defining a more generic category of light fundamental particles, the weakly interacting slim particles (WISPs), of which the axion is the most outstanding prototype, appearing in other well-motivated extensions of the SM, like string theory. After 35 years, the axion not only remains associated with the

the most compelling solution to the strong CP problem, but it is recognized as one of the best motivated experimental portals to physics beyond the SM.

2.2 Axions as dark matter candidate

The recent high precision cosmological data are well described by what is called the standard cosmological model [29]. Its most remarkable trait is the need for at least two new components not accounted for by the Standard Model of particle physics: Dark Energy —which can be explained as a cosmological constant, vacuum energy or a quintessence field— and Dark Matter (DM) —non-relativistic particles that interact feebly with standard particles and among themselves. The particle interpretation of DM thus requires new fields beyond the SM.

A popular example is the "weakly interacting massive particle" (WIMP) typically appearing in supersymmetric extensions of the SM, and actively searched for in underground experiments. However, for the time being there is no hint of supersymmetry at the LHC and also no clear signature for WIMPs in direct-detection experiments whose sensitivity to the WIMP-nucleon cross-section has advanced by an amazing four orders of magnitude over the last decade.

It has been known since the early 80s that the PQ mechanism provides a very compelling scenario for relic axion production. As shown below, axions are just as attractive a solution to the DM problem as WIMPs. As the latter, they appear in extensions of the SM that are independently motivated and also provide a valid DM candidate (i.e. they are not conceived *ad hoc* for that purpose). Moreover, the possibility of a mixed WIMP-axion DM is not only not excluded, but theoretically appealing [30, 31]. Conventionally, both axion and WIMP cold DM are thought to behave identically at cosmological and astrophysical scales, so there is no hint from cosmology to prefer one or the other (or both). However, although still speculative, some potentially discriminating signatures have been proposed. It has been recently suggested [32] that cold axions form a Bose-Einstein condensate, and this would produce a peculiar structure in DM galactic halos (caustic rings) for which some observational evidence seems to exist [33]. This fact would be applicable to any WISP cold DM population, but not to WIMPs.

Relic axions can be produced thermally by collisions of particles in the primordial plasma, just like WIMPs. However, being quite light particles, this axion population contributes –like neutrinos– to the hot DM component. This production mechanism is more important for larger m_a. Cosmological observations constraining the amount of hot DM, can be translated into a upper bound on the axion mass of $m_a \lesssim 0.9$ eV [34, 35].

Most interesting from the cosmological point of view is the non-thermal production of axions: the *vacuum-realignment* mechanism and the decay of topological defects (axion strings and domain-walls), both producing non-relativistic axions and therefore contributing to the cold DM [36, 37].

In the very early universe, when the temperature drops below $\sim f_a$, the axion field appears in the theory and sets its initial value differently in different causally connected regions. Later, at the QCD phase transition, the axion potential rises and only then does the axion acquire its mass m_a. Then the axion field relaxes to its CP conserving minimum, around which it oscillates with decreasing amplitude (thus solving the strong CP problem dynamically). These oscillations represent a population of non-relativistic axions, with a density that depends on the unknown initial value of the field before the start of the oscillations (initial misalignment angle $\theta_0 \equiv a_0/f_a \in (-\pi, \pi)$). Moreover, because a/f_a is an angle variable, discrete domains, differing in 2π naturally form after QCD transition and at their borders topological defects, i.e., strings and walls, form too. These defects soon decay radiating a large amount of non-relativistic axions which add up to the realignment population. While the realignment population density is relatively easily calculable (although dependent on the value of θ_0), the population from the decay of topological defects suffers from significant uncertainties.

In general, two main cosmological scenarios can be considered, depending on whether inflation happens after (case 1) or before (case 2) the PQ phase transition (or if the PQ symmetry is restored by reheating after inflation). In case 1, the axion field is homogenized by inflation, the value of θ_0 is thus unique in all the observable Universe, and the topological defects are diluted away. In that case the axion cold DM density is easily determined, as only the realignment mechanism contributes to it. Expressed as the ratio of axion DM to the observed value $\Omega_{\rm DM,obs}h^2 = 0.111(6)$ is [38, 39]

$$\frac{\Omega_a}{\Omega_{\rm DM,obs}} \sim \theta_0^2 F \left(\frac{f_a}{5\times 10^{11}\,\rm GeV}\right)^{1.184} \simeq \theta_0^2 F \left(\frac{12\,\mu\rm eV}{m_a}\right)^{1.184} . \tag{6}$$

Here $F = F(\theta_0, f_a)$ is a correction factor accounting for anharmonicities, the delay of the oscillations when θ_0 is large and any effects of non-standard cosmologies (the above expression is computed assuming radiation domination during the QCD phase transition).

Contrary to thermal production, this mechanism is more important for lower m_a. For typical values of $\theta_0 \sim \mathcal{O}(1)$, m_a should exceed $\sim$10 μeV to have a relic axion density not exceeding the known CDM density. Much smaller masses could still give the correct amount of DM if by some means θ_0 is accidentally small, something that could be justified for instance by anthropic reasons [40]. Axion masses up to $m_a \sim$ meV can still give the right relic density for large θ_0. Note that F is normalized such that $F \to 1$ when $\theta_0 \to 1$ but it can boost Ω_a by more that one order of magnitude for $\theta_o \sim \pi$.

In case 2, the value of θ_0 is randomly distributed in different causally connected parts of the universe at the time of the PQ phase transition. One then has to average the above result for $\theta_0 \in (-\pi, \pi)$ and obtain a robust estimate of the DM contribution due to vacuum-realignment:

$$\frac{\Omega_{a,\rm VR}}{\Omega_{\rm DM,obs}} \sim \left(\frac{40\,\mu\rm eV}{m_a}\right)^{1.184} . \tag{7}$$

However, in this case the contribution of axion strings and domain-wall decays to axion DM must be taken into account, but its computation is rather uncertain and a matter of a longstanding debate. Some authors argue that the contribution is of the same order than $\Omega_{a,\rm VR}$ [41], while others [37, 42] find it considerably larger:

$$\frac{\Omega_{a,\rm string+wall}}{\Omega_{\rm DM,obs}} \sim \left(\frac{400\,\mu\rm eV}{m_a}\right)^{1.184} \tag{8}$$

In any case, axions could easily account for the totality of cold DM needed by current cosmological models. The above uncertainties prevent us from defining specific preferred axion parameters, but it is clear that this can happen for a wide range of feasible axion models well beyond current limits. The “classic axion window” [37], $m_a \sim 10^{-5} - 10^{-3}$ eV, is often quoted as the preferred m_a range for axion cold DM, although much lower masses are still possible in fine-tuned models, the so-called “anthropic axion window” [43, 44]. QCD axions with masses above the classic window can still solve the DM problem if non-standard cosmological scenarios are invoked [45], or they can be a subdominant DM component. Mixed axion-WIMP DM is a possibility that may even be theoretically appealing [30, 31]. Moreover, axions are not the only WISPs allowing for a solution to the dark matter question. The nonthermal production mechanisms attributed to axions are indeed generic to bosonic WISPs such as axion-like particles or hidden photons (see next section). As recently shown [46], a wide range of $g_{a\gamma} - m_a$ space can generically contain models with adequate DM density.

To summarize, axions are as attractive a solution to the DM problem as WIMPs. In the current situation, with no hint from supersymmetry at the LHC and without a clear signature in WIMP direct-detection experiments, the hypothesis of axion DM stands out as increasingly interesting and deserves serious attention. The cosmological implications of the axion are well founded and represent a powerful motivation to push experimental searches well beyond current limits.

2.3 Other axion-like particles (ALPs)

Although the axion is the best motivated and most studied prototype, a whole category of particles called axion-like particles (ALPs) or, more generically, weakly interacting slim particles, WISPs, are often invoked in several scenarios, both theoretically and observationally motivated, at the low energy frontier of particle physics [47]. Although not necessarily related to the axion, ALPs share part of its phenomenology, and therefore they would be searchable by similar experiments. ALPs are light (pseudo)scalar particles that weakly couple to two photons, but not to two gluons like the axion [48, 49]. As such, the ALPs parameters $g_{a\gamma}$ and m_a are now to be viewed as completely independent, and the full parameter space of Fig. 1 is potentially populated by ALPs (not constrained to the yellow band as the axion models are).

ALPs can appear in extensions of the SM as pseudo Nambu-Goldstone bosons of new symmetries broken at high energy. Moreover, it is now known that string theory also predicts a rich spectrum of ALPs (including the axion itself) [50, 51, 52]. Remarkably, the region of the ALP parameter space at reach for future experiments is theoretically favored as they correspond to string scales contributing to the natural explanation of several hierarchy problems in the SM. It is intriguing that the possible detection of ALPs could become key to the much sought experimental test of string theory.

Beyond ALPs, other important examples of WISPs are hidden photons and minicharged particles [53, 54, 55]. They appear in extensions of the SM including hidden sectors, i.e., sectors that interact with SM particles through interchange of very heavy particles (e.g., a hidden sector is commonly employed for supersymmetry breaking). Hidden photons have kinetic mixing with normal photons, and therefore show a phenomenology similar to axion-photon oscillations (but this time without the external magnetic field), leading to the dissapearance and regeneration of photons as they propagate in vacuum [54]. Minicharged particles are particles with fractional electric charge, arising naturally in theories with hidden sectors.

As previously mentioned, under some circumstances, WISPs can also provide the right DM density. The nonthermal production mechanisms described in the previous sections are indeed generic to other bosonic WISPs such as ALPs or hidden photons. This WISPy DM has recently been studied [46], and in both cases a wide range of parameter space (in the case of ALPs $g_{a\gamma}$–m_a space) can generically contain models with adequate DM density, part of it at reach of current or future experiments.

It is remarkable that light scalars are also invoked in attempts to find a particle physics interpretation of Dark Energy, the so-called “quintessence” fields. This possibility is very much constrained from the non observation of new long-range forces, unless more sophisticated mechanisms are implemented, mechanisms that lead sometimes to ALP phenomenology [56]. More recently, fields with an environment-dependent mass or couplings, chameleons [57] or galileons, are being studied in this same context. Although these concepts are still in a very early stage of development, the possibility that detection techniques originally conceived to search for axions or ALPs could evolve into the first particle physics experiments directly testing Dark Energy is truly exciting.

All these families of models compose together a growing field of theoretical research. It is now acknowledged that, complementary to the conventional research performed at colliders of increasing energy (the high energy frontier), new physics can be hidden at very low energies too (the intensity frontier) for which different experimental tools, based rather on high precision and high source intensity, are required.

2.4 Astrophysical hints for axions and ALPs

The existence of axions or ALPs may have important consequences for some astrophysical phenomena. Since the early days of axions, well understood stellar physics has been used to constrain axion couplings [17] and derive limits, the most relevant of which have been presented previously. More intriguing are the cases where unexplained astrophysical observations may indicate the effects of an ALP. These situations must be treated with caution because usually an alternative explanation using standard physics or an uncontrolled systematic effect cannot be ruled out. At the same time, such models can further strengthen the physics case for exploring favored regions of parameter space, when other motivations already exist. We want to mention briefly two such cases that we consider specially relevant: the excessive transparency of the intergalactic medium to very high energy (VHE) photons, and the anomalous cooling rate of white dwarfs.

VHE photons (i.e., with energies $\gtrsim$ 100 GeV) have a non-negligible probability to interact via e^+e^- pair production with the background photons permeating the Universe – the extragalactic background light (EBL) – when long intergalactic distances are involved. That is, the Universe should be opaque to distant VHE emitters like active galactic nuclei (AGN). EBL density is measured by its imprint in blazar spectra by both HESS[68] and Fermi [69], and found in agreement with models. However, several independent observations seem to indicate that the degree of transparency of the Universe at VHE is too high, even for the lowest density EBL models developed [70, 71]. Current imaging atmospheric Cherenkov telescopes (both HESS [72] and MAGIC [73, 74]) have reported the observation of VHE photons with arrival directions clearly correlated with AGNs, some of them as distant as a $\sim$Gpc, with spectra that require either a too low density EBL, or anomalously hard spectra at origin. Alternatively, these photons could be secondaries produced in electromagnetic cascades [75], but this is in conflict with the sometimes fast time-variability of these sources [66]. Independent additional evidence might come from the observation of ultra high energy cosmic rays (UHECR) of energies $E > 10^{18}$ GeV correlated with very distant blazars [76, 77].

These observations could be easily explained by scenarios invoking photon-ALP oscillations triggered by intervening cosmic magnetic fields. These fields can be the intergalactic magnetic field, or the local magnetic fields at origin (at the AGN itself, or in the case of objects belonging to galactic clusters, the cluster magnetic field) and in the Milky Way. Thus, the ALP component can travel unimpeded through the intergalactic medium, and as a result the effective mean free path of the photon increases. Several authors have invoked one of these scenarios [78, 79, 80, 81, 82, 83, 71, 66] to account for the unexplained observations. For some of these cases, approximate required ALP parameters $g_{a\gamma}$ and m_a are drawn. Interestingly, most of them coincide roughly in requiring very small ALP mass $m_a \lesssim 10^{-(10-7)}$ eV (to maintain coherence over sufficiently large magnetic lengths) and a $g_{a\gamma}$ coupling in the ballpark of $g_{a\gamma} \sim 10^{-12}$–$10^{-10}$ GeV^{-1}. A more definite region -shown in Fig. 1- is extracted in [66] from a large sample of VHE gamma-ray spectra. Note that it extends to lower m_a values than the ones shown on the plot. Although these parameters are far from the standard QCD axions, as more generic ALP models they lie just beyond the best current experimental limits on $g_{a\gamma}$ from CAST (see next section). The most fiducial region related to this hint could be explored with IAXO, as commented later and shown in Fig. 25: only if the relevant astrophysical magnetic fields are much larger than expected, IAXO would not cover the entire relevant parameter space.

The random character of astrophysical magnetic fields produces a particular scattering of the photon

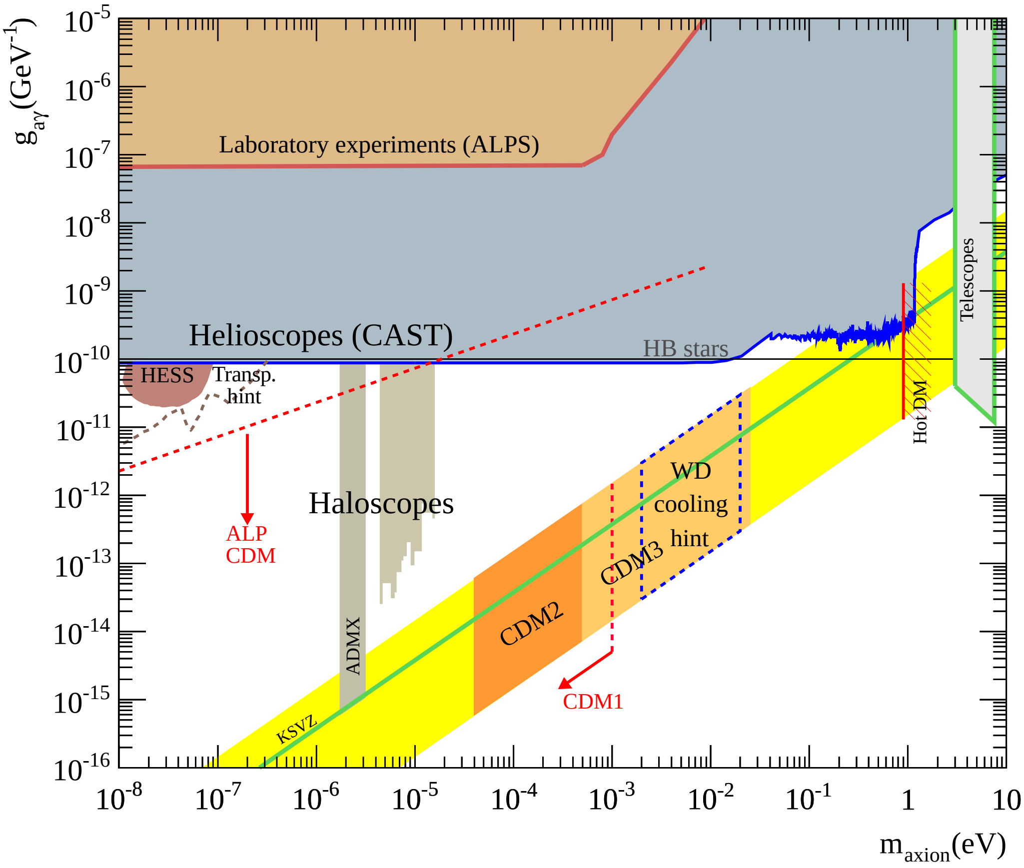

Figure 1: Comprehensive axion/ALP parameter space, highlighting the three main front lines of direct detection experiments: LSW experiments (ALPS [58]), helioscopes and haloscopes. The blue line corresponds to the current helioscope limits, dominated by CAST [59, 60, 61, 62] for practically all axion masses. Also shown are the constraints from horizontal branch (HB) stars, and hot dark matter (HDM) and the ones from searches of decay lines in telescopes [63, 64, 65]. The yellow "axion band" is defined roughly by $m_a f_a \sim m_\pi f_\pi$ with a somewhat arbitrary width representing the range of realistic axion models. The green line refers to the KSVZ model. The orange parts of the band correspond to cosmologically interesting axion models: models in the "classical axion window" possibly composing the totality of DM (labelled "CDM2") or a fraction of it ("CDM3"). The anthropic window ("CDM1") corresponds to a range unbound on the left and up to $\sim$1 meV. For more generic ALPs, practically all the allowed space up to the red dash line may contain valid ALP CDM models [46]. The region of axion masses invoked in the WD cooling anomaly is shown by the blue dash line. The region at low m_a above the dashed grey line is the one invoked in the context of the transparency of the universe [66] (note that is extends to masses lower than the ones in the plot), while the solid brown region is excluded by HESS data [67].

arrival probability that complicates the test of the ALP hypothesis [84]. In turn, this randomness can be used to constraints ALP parameters, as it should imprint irregularities in high-energy source spectra [85]. This effect is used by the HESS collaboration with blazar observations to exclude couplings of the order of a few 10^{-11} GeV^{-1} for masses of $10^{-8} - 10^{-7}$ eV (1), as shown in Fig. 1. The same method is used with X-ray data from the Hydra galaxy cluster [86] constraining $g_{a\gamma} < 8 \times 10^{-12}$ GeV^{-1} for ALP masses $< 10^{-11}$ eV. Still in the X-ray band, some luminosity relations of active galactic nuclei were recently shown to have precisely this particular scatter [87] although this claim is still controversial [88]. Finally, photon-ALP mixing is polarization dependent, a fact that could explain long-distant correlations of quasar polarization [89] and offers further testing opportunities [90]. This possibility is however challenged by the absence of significant circular polarisation [91].

The second astrophysical scenario we want to convey in this section regards the interior of white dwarf (WD) stars. The evolution of these objects follows just a gravothermal process of cooling, therefore their luminosity function (number of stars per luminosity interval) is predicted with accuracy by stellar models. The presence of extra cooling via axion emission speeds up the cooling thus suppressing the luminosity function at certain values of the WD luminosity. This is most relevant for non-hadronic axions with coupling to electrons g_{ae}, because axio-bremstrahlung would be very efficient in WDs.

These arguments were used long ago to constrain g_{ae} [22] and they have been cross-checked and improved over the years [23, 24, 25]. Nowadays, there is common agreement on an upper limit $g_{ae} < 3 \times 10^{-13}$. However, recent works are based on such a well populated luminosity function and well-studied WD cooling models that are able to claim that a small amount of axion energy loss is actually favored by data [23, 24]. This claim corresponds to $g_{ae} \sim 1 - 2 \times 10^{-13}$. The effect of axions decreases the number of bright WDs and increases the low bright end of the luminosity function. The need for this effect is apparent from the comparison of observations and theoretical cooling models (see for example Fig. 5 of [24]) but it is very small. A recent critic suggests that the existence of anomalous cooling cannot be concluded at any significant CL with the present measurements [25]. However further evidence for extra cooling in WDs comes from independent observations. The period decrease of certain pulsating WDs provides a direct measurement of their cooling and thus can be used to asses the necessity of non-standard cooling mechanisms. Two pulsating WDs have recently shown a preference for axion cooling: the ZZ Ceti star G117-B15A [92] and R548 [93]. Both fit better the expectations for $g_{ae} \simeq 5^{+1.2}_{-1.6} \times 10^{-13}$ and $g_{ae} \simeq 5^{+1.7}_{-4.9} \times 10^{-13}$, respectively ($2\sigma$ intervals quoted). The level of the improvement over the standard case is at $\sim 3\sigma$ and 2σ, respectively. The upper parts of these ranges are firmly excluded by the luminosity function argument and by the tip of the Red-Giant branch in M5. Given the scatter of the preferred values of g_{ae}, the tension with other limits and the possibility of unaccounted systematics or forgotten standard effects it is certainly premature to conclude the existence of axion energy loss in WDs. However, it is intriguing that none of the observables reported here fits better by reducing the standard stellar cooling. They all seem to improve with some extra cooling, which could be attributed to axions (or any pseudoscalar with coupling to electrons) with $g_{ae} \sim 1 - 5 \times 10^{-13}$. Even the agreement of the tip of the RGB of M5 with observations improves if we allow for couplings in this range, although at the $1 - \sigma$ level and thus again not significantly.

These g_{ae} values imply axion decay constants in the range $f_a = C_{ae} m_e / g_{ae} \in (2\text{–}5) \times C_{ae} 10^9$ GeV, corresponding to an axion mass $m_a \in (1\text{–}4)$ meV$/C_{ae}$. For DSFZ axions $C_{ae} < 1/3$ and this value corresponds to axion masses $m_a > 3$ meV (see "WD cooling hint" in Fig. 1). As shown later, IAXO may reach sensitivity to these models (sections 5.1 and 5.2).

Generic ALPs appearing in field and string theory extensions of the SM can just, as DFSZ axions, feature a coupling of electrons and photons. The typical sizes are similar to those of axions $g_{a\gamma}^{\mathrm{ALP}} =$

$\alpha \times C_\gamma^{\rm ALP}/2\pi f$ and $g_{ae} = C_e^{\rm ALP} m_e/f$ where f is a high energy scale (analogous to f_a) and $C^{\rm ALP}$'s are $\mathcal{O}(1)$ coefficients. Due to their inverse dependence with f, both are interrelated and ALPs with a coupling to electrons $g_{ae}^{\rm ALP} \sim 10^{-13}$ typically would have $g_{a\gamma}^{\rm ALP} \sim (C_\gamma^{\rm ALP}/C_e^{\rm ALP}) 2 \times 10^{-13}$ GeV^{-1}. Due to this reasoning, the WD favored region is sometimes expressed as a $g_{a\gamma}$ range [94]. Unfortunately the model dependence $C_\gamma^{\rm ALP}/C_e^{\rm ALP}$ can be significant.

Once more, although alternative explanations for these observations cannot be ruled out, it is intriguing that they together point to relatively well defined axion parameters, that are compatible with feasible QCD axion parameters, and that are not excluded by previous bounds. Moreover, axions at the meV scale are very close to the DM favored window (see previous section), have interesting phenomenological implications [95] and constitute a region especially difficult to explore experimentally. As shown later, IAXO constitutes probably the only realistic experimental technique able to explore (part of) these models.

3 The search for axions

3.1 Experimental strategies for direct axion detection

In spite of their weak interactions, axions could be directly detected in a number of realistic experimental scenarios. Three main categories of experimental approaches can be distinguished depending on the source of axions employed: *haloscopes* look for the relic axions potentially composing our dark matter galactic halo, *helioscopes* look for axions potentially emitted at the core of the sun, and *light-shining-through-wall* (LSW) experiments look for axion-related phenomena generated entirely in the laboratory. All three strategies invoke the generic axion-photon interaction, and thus rely on the use of powerful magnetic fields to trigger the conversion of the axions into photons that can be subsequently detected.

Haloscopes [14] use high-Q microwave cavities inside a magnetic field to detect photons from the conversion of relic axions. Being non relativistic, these axions convert into monochromatic photons of energy equal to m_a. For a cavity resonant frequency matching m_a, the conversion is substantially enhanced. The cavity must therefore be tunable and the data taking is performed by scanning very thin m_a-slices of parameter space. As shown in Fig. 1, past haloscope searches, and in particular ADMX [96, 97], have proven that sensitivities in $g_{a\gamma}$ enough to probe QCD axion models are possible for m_a in the few μeV range, under the assumption that axions are the main cold DM component. R&D is ongoing [98, 99], and new ideas being proposed [100, 101, 102], to extend the sensitivity of haloscopes to higher m_a values.

Helioscopes [14] look for axions emitted by the Sun, and therefore do not rely on the assumption of axions being the DM. Axion emission by the solar core is a robust prediction involving well known solar physics and the Primakoff conversion of plasma photons into axions. Solar axions have $\sim$keV energies and in strong laboratory magnetic fields can convert back into detectable x-ray photons. Contrary to haloscopes, the signal in helioscopes is independent on the axion mass up to relatively large values (e.g. 0.02 eV for CAST). Using the technique of the buffer gas [103] the sensitivity can be further extended to masses up to $\sim$eV [60, 61, 62]. The latest and most powerful axion helioscope is the CERN Axion Solar Telescope CAST briefly described in the next section. Its latest results, shown in Fig. 1, have surpassed the astrophysical limit $g_{a\gamma} \sim 10^{-10}$ GeV^{-1} in a wide m_a range. This means that for the highest mass values, close to the $\sim$1 eV, the sensitivity allows tests of some QCD axion models. Together with haloscopes, helioscopes are the only experimental technique with sensitivity to explore realistic QCD axion models. These two techniques are complementary, exploring the lower- (with haloscopes) and the higher-mass (with helioscopes) regions of the axion phase space not yet searched nor excluded. An advantage of helioscopes is that there is a clear scaling strategy to substantially push the present sensitivity frontline to lower values of $g_{a\gamma}$ and m_a, a strategy that is implemented in this proposal, and detailed in the following sections.

It is worth mentioning that a similar helioscope-like scheme can be invoked in solid crystalline detectors, and used to detect solar axions. In this case, the local conversion into photons is triggered by the periodic electromagnetic field of the crystal [104, 105, 106], giving rise to very characteristic Bragg patterns that have been searched for as by-products of a number of underground WIMP experiments [107, 108, 109, 110, 111]. However, the prospects of this technique have proven limited [112, 113] and do not compete with dedicated helioscope experiments.

LSW [114] experiments use high intensity light sources (e.g., lasers) and strong magnetic fields to produce ALPs in the laboratory. These ALPs can reconvert back into detectable photons after an opaque wall. This technique therefore does not rely on any astrophysical or cosmological assumption for the ALPs. A number of experiments have already used this technique to search for ALPs, with a sensitivity, however, still a few orders of magnitude behind helioscopes (see the ALPS limit in Fig. 1 from [58]). The prospects for future scaled-up setups [115], in particular ALPS-II [116], could surpass current helioscope limits for low m_a values and reach some unexplored ALP parameter space, although in any case, still without enough sensitivity to reach the QCD axion band.

All the searches mentioned up to now rely solely on the axion-photon phenomenology and therefore can be represented in the ALP parameter space of Fig. 1. Other small scale searches have been performed with a less generic scope, sometimes as by-products of other experiments. They are relevant for specific subsets of axion or WISP models. For example, axions have been searched for via more specific phenomenology (e.g. through the axioelectric effect [117, 118, 119, 120], or axion-emitting nuclear transitions [121, 122, 123, 124, 125, 126], among others). Specific non-axion WISPs have been (or are being) searched for in dedicated setups (e.g. hidden photons [127, 128]) or as by-products of axion and ALPs searches (e.g. chameleons [129]) or WIMP searches (e.g. [130]). For an updated review of all initiatives going on, we refer to the community documents prepared in recent roadmapping events, both in US [94, 131] and Europe [132, 1].

Below we will focus on the helioscope frontier. We will argue that the decade-long operation of CAST has not only led to one of the most competitive set of bounds on the axion and ALPs, but also to the establishment of a relevant community and the specific operational experience required to design a scaled-up version (forth generation) of the axion helioscope concept. IAXO is based on these ideas and aims to substantially push the helioscope envelope well into unexplored regions of the axion and ALP parameter space motivated by the arguments detailed in the previous section.

3.2 Solar axions and the axion helioscope frontier

Axions can be produced in the solar interior by a number of reactions. The most relevant channel is the Primakoff conversion of plasma photons into axions in the Coulomb field of charged particles via the generic $a\gamma\gamma$ vertex. The Primakoff solar axion flux, shown on the left of Fig. 2 peaks at 4.2 keV and exponentially decreases for higher energies. This spectral shape is a robust prediction depending only on well known solar physics, while the only unknown axion parameter is $g_{a\gamma}$ and enters the flux as an overall multiplicative factor $\propto g_{a\gamma}^2$. For the particular case of non-hadronic axions having tree-level interactions with electrons, other productions channels (e.g., brehmstrahlung, compton or axion recombination) should be taken into account, as their contribution can be greater than that of the Primakoff mechanism (see plot on the right of Fig. 2). However, the usual procedure in helioscopes considers only the Primakoff component because: 1) it maintains the broadest generality and covers a larger fraction of ALPs and 2) astrophysical limits on g_{ae} are quite restrictive and largely disfavor the values that could be reached by helioscopes looking at the non-hadronic solar axion flux. With IAXO, it will be possible for the first time to supersede even astrophysical limits on g_{ae}, opening the possibility to probe an interesting set of models. Therefore we will study with some detail the specific case of non-hadronic axions later on.

By means again of the $a\gamma\gamma$ vertex, solar axions can be efficiently converted back into photons in the presence of an electromagnetic field. The energy of the reconverted photon is equal to the incoming axion, so a flux of detectable x-rays of few keV energies is expected. The probability that an axion going through the transverse magnetic field B over a length L will convert to a photon is given by [14, 135, 59]:

$$P_{a\gamma} = 2.6 \times 10^{-17} \left(\frac{B}{10\ \mathrm{T}}\right)^2 \left(\frac{L}{10\ \mathrm{m}}\right)^2 \left(g_{a\gamma} \times 10^{10}\ \mathrm{GeV}\right)^2 \mathcal{F}$$

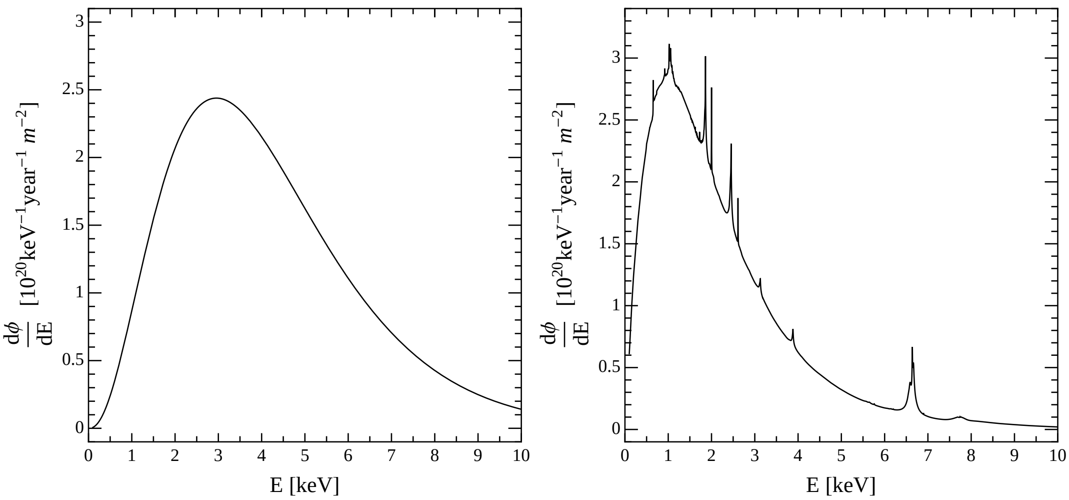

Figure 2: Solar axion flux spectra at Earth by different production mechanisms. On the left, the most generic situation in which only the Primakoff conversion of plasma photons into axions is assumed. On the right the spectrum originating from processes involving electrons, bremsstrahlung, Compton and axio-recombination [133, 134]. The illustrative values of the coupling constants chosen are $g_{a\gamma} = 10^{-12}$ GeV^{-1} and $g_{ae} = 10^{-13}$.

where the form factor $\mathcal{F}$ accounts for the coherence of the process:

$$\mathcal{F} = \frac{2(1 - \cos qL)}{(qL)^2} \tag{9}$$

and q is the momentum transfer. The fact that the axion is not massless, puts the axion and photon waves out of phase after a certain length. The coherence is preserved ($\mathcal{F} \simeq 1$) as long as $qL \ll 1$, which for solar axion energies and a magnet length of ∼10 m happens at axion masses up to $\sim 10^{-2}$ eV, while for higher masses $\mathcal{F}$ begins to decrease, and so does the sensitivity of the experiment. To mitigate the loss of coherence, a buffer gas can be introduced into the magnet beam pipes [103, 60] to impart an effective mass to the photons $m_\gamma = \omega_\mathrm{p}$ (where ω_p is the plasma frequency of the gas, $\omega_\mathrm{p}^2 = 4\pi\alpha n_e/m_e$). For axion masses that match the photon mass, $q = 0$ and the coherence is restored. By changing the pressure of the gas inside the pipe in a controlled manner, the photon mass can be systematically increased and the sensitivity of the experiment can be extended to higher axion masses.

The basic layout of an axion helioscope thus requires a powerful magnet coupled to one or more x-ray detectors. When the magnet is aligned with the Sun, an excess of x-rays at the exit of the magnet is expected, over the background measured at non-alignment periods. This detection concept was first experimentally realized at Brookhaven National Laboratory (BNL) in 1992. A stationary dipole magnet with a field of $B = 2.2$ T and a length of $L = 1.8$ m was oriented towards the setting Sun [136]. The experiment derived an upper limit on $g_{a\gamma}$ $(99\%$ CL$) < 3.6 \times 10^{-9}$ GeV^{-1} for $m_a < 0.03$ eV. At the University of Tokyo, a second-generation experiment was built: the Tokyo axion heliscope (also nicknamed Sumico). Not only did this experiment implement a dynamic tracking of the Sun but it also used a more powerful magnet ($B = 4$ T, $L = 2.3$ m) than the BNL predecessor. The bore, located between the two coils of the magnet, was evacuated and higher-performance detectors were installed [137, 138, 139]. This new setup resulted in an improved upper limit in the mass range up to 0.03 eV of $g_{a\gamma}(95\%\ \mathrm{CL}) < 6.0 \times 10^{-10}$

GeV^{-1}. Later experimental improvements included the additional use of a buffer gas to enhance sensitivity to higher-mass axions.

A third-generation experiment, the CERN Axion Solar Telescope (CAST), began data collection in 2003. The experiment uses a Large Hadron Collider (LHC) dipole prototype magnet with a magnetic field of up to 9 T over a length of 9.3 m [140]. Like Sumico, CAST is able to follow the Sun for several hours per day using a sophisticated elevation and azimuth drive. This CERN experiment is the first helioscope to employ x-ray focusing optics for one of its four detector lines [141], as well as low background techniques from detectors in underground laboratories [142]. During its observational program from 2003 to 2011, CAST operated first with the magnet bores in vacuum (2003–2004) to probe masses $m_a < 0.02$ eV. No significant signal above background was observed. Thus, an upper limit on the axion-to-photon coupling of $g_{a\gamma}$ $(95\%\ \text{CL}) < 8.8 \times 10^{-11}$ GeV^{-1} was obtained [135, 59]. The experiment was then upgraded to be operated with ^{4}He (2005–2006) and ^{3}He gas (2008–2011) to obtain continuous, high sensitivity up to an axion mass of $m_a = 1.17$ eV. Data released up to now provide an average limit of $g_{a\gamma}$ $(95\%\ \text{CL}) \lesssim 2.3 \times 10^{-10}$ GeV^{-1}, for the higher mass range of 0.02 eV $< m_a <$ 0.64 eV [60, 61] and of about $g_{a\gamma}$ $(95\%\ \text{CL}) \lesssim 3.3 \times 10^{-10}$ GeV^{-1} for 0.64 eV $< m_a <$ 1.17 eV [62], with the exact value depending on the pressure setting.

So far each subsequent generation of axion helioscopes has resulted in an improvement in sensitivity to the axion-photon coupling constant of about a factor 6 over its predecessors. CAST has been the first axion helioscope to surpass the stringent limits from astrophysics $g_{a\gamma} \lesssim 10^{-10}$ GeV^{-1} over a large mass range and to probe previously unexplored ALP parameter space. As shown in Fig. 1, in the region of higher axion masses ($m_a \gtrsim 0.1$ eV), the experiment has entered the band of QCD axion models for the first time and excluded KSVZ axions of specific mass values. CAST is the largest collaboration in axion physics with ~ 70 physicists from about 16 different institutions in Europe and the USA, and one of the first astroparticle experiments at CERN. The collaboration members have gathered unique expertise in the technologies applied in axion helioscopes throughout the last decade and are ready to apply this knowledge for a next generation axion helioscope.

We have recently shown [143] that a further substantial step beyond the current state-of-the-art represented by CAST is possible with a new fourth-generation axion helioscope. Our concept relies on a purpose-built magnet capable of tracking the sun for $\sim$12 hours each day, focusing x-ray optics to minimize detector area, and low background x-ray detectors optimized for operation in the 0.5–10 keV energy band. Pushing the current helioscope boundaries to explore the range in $g_{a\gamma}$ from 10^{-10} to well below 10^{-11} GeV^{-1} is highly motivated, as evident from previous section. We propose here to carry out this task with IAXO, as described in the following sections, as one of the main experimental pathways in the next decade for the axion community. More generally, a detection with IAXO would have profound implications for particle physics, with clear evidence of physics beyond the SM.

3.3 A new generation axion helioscope: figures of merit

All axion helioscopes to date make use of "recycled" magnets that were originally built for other experimental purposes. In order to achieve at least an order of magnitude improvement in sensitivity to $g_{a\gamma}$, a new and purpose-built magnet must be constructed. As explained in detail in section 4.1, a toroidal ATLAS-like magnet geometry [144] was identified as optimal design for this purpose [143]. This design opens the way for improvement mainly through a larger cross-sectional area for the helioscope, however this effectively translates in an improvement in sensitivity only if x-ray focusing is available for all the magnet cross-section. CAST has successfully used "recycled" x-ray optics, but only for one magnet bore of area ~ 15 cm^2. IAXO relies on x-ray focusing from much larger bore areas of $\sim$m^2 down to spot

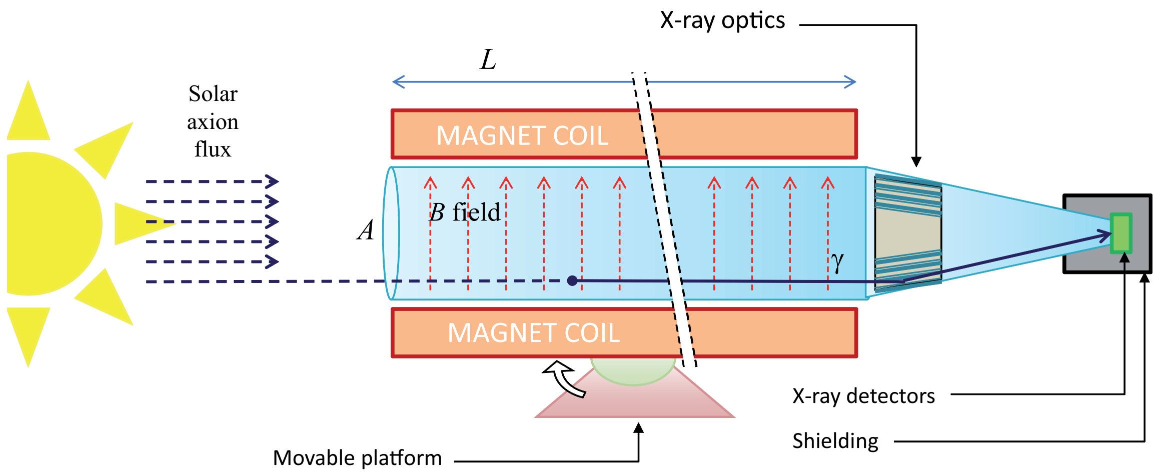

Figure 3: Conceptual arrangement of an enhanced axion helioscope with x-ray focalization. Solar axions are converted into photons by the transverse magnetic field inside the bore of a powerful magnet. The resulting quasi-parallel beam of photons of cross sectional area A is concentrated by an appropriate x-ray optics into a small spot area a in a low background detector. The envisaged design for IAXO, described in section 4, includes eight such magnet bores, with their respective optics and detectors.

sizes of few $\sim$mm^2 areas.

Indeed, in [143] we defined the basic layout of an *enhanced axion helioscope* as one in which the entire cross sectional area of the magnet is equipped with one or more x-ray focussing optics and low background x-ray detectors. This arrangement is schematically shown in Fig. 3. It is useful to define an approximate figure of merit (FOM) of an enhanced axion helioscope to understand the potential contribution of each component to the overall sensitivity. One such metric f was defined in [143] as inversely proportional to the minimal signal strength to which the experiment is sensitive to, i.e. $f \propto g_{a\gamma,\rm lim}^{-4}$, and thus:

$$f \equiv f_M \, f_{DO} \, f_T \tag{10}$$

where we have factored the FOM to explicitly show the contributions from various experimental parameters: magnet, detectors and optics, and tracking (effective exposure time of the experiment)

$$f_M = B^2 \, L^2 \, A \qquad f_{DO} = \frac{\epsilon_d \, \epsilon_o}{\sqrt{b \, a}} \qquad f_T = \sqrt{\epsilon_t \, t} \, . \tag{11}$$

where B, L and A are the magnet field, length and cross sectional area, respectively. The efficiency $\epsilon = \epsilon_d \, \epsilon_o \, \epsilon_t$, being ϵ_d the detectors' efficiency, ϵ_o the optics throughput or focusing efficiency (it is assumed that the optics covers the entire area A), and ϵ_t the data-taking efficiency, i. e. the fraction of time the magnet tracks the Sun (a parameter that depends on the extent of the platform movements). Finally, b is the normalized (in area and time) background of the detector, a the total focusing spot area and t the duration of the data taking campaign.

As will be shown below, these FOMs clearly demonstrate the importance of the magnet parameters when computing sensitivity of an axion helioscope. The CAST success has relied, to a large extent, on the availability of the first class LHC test magnet which was recycled to become part of the CAST helioscope. Going substantially beyond the CAST magnet's B or L is difficult, as 9 T is close to the maximum field one can realistically get in current large-size magnets, while 10 m is a considerable length for a structure that needs to be moved with precision. The improvement may come however in the cross section area, which in the case of the CAST magnet is only 3×10^{-3} m^2. Substantially larger cross sections can be achieved, although one needs a different magnet configuration. It is an essential part of our proposal that a new magnet must be designed and built specifically for this application, if one aims at a significant step forward in sensitivity. We discuss in detail this issue in section 4.1, where we show that cross section areas A of up to few m^2 are feasible, while keeping the product of BL close to levels achieved for CAST.

Another area for improvement will be the x-ray optics. Although CAST has proven the concept, only one of the four CAST magnet bores is equipped with optics. The use of focusing power in the entire magnet cross section A is implicit in the FOM of equation 11, and therefore the improvement obtained by enlarging A comes in part because a correspondingly large optic is coupled to the magnet. Here the challenge is not so much achieving exquisite focusing or near-unity reflectivity (of course, the larger the throughput ϵ_o and the smaller the spot area a, the better), but the availability of cost-effective x-ray optics of the required size. This issue is discussed in detail in section 4.2.

Finally, we need to discuss the x-ray detectors. CAST has enjoyed the sustained development of its detectors towards lower backgrounds during its lifetime. The latest generation of Micromegas detectors in CAST are achieving backgrounds of $\sim 10^{-6}$ counts keV^{-1} cm^{-2} s^{-1} . This value is already a factor of more than 100 better than the background levels obtained during the first data-taking periods of CAST. Prospects for reducing this level to 10^{-7} counts keV^{-1} cm^{-2} s^{-1} or even lower appear feasible and are discussed in section 4.3.

Although it has less impact on the sensitivity than the other factors, it is also desirable to improve the tracking efficiency ϵ_t. The goal is to improve performance from the current value of 0.12 obtained with CAST to $\epsilon_t = 0.3$–0.5. This gain would help in gathering exposure more quickly and shorten the time required for the experiment to move into the non-zero background regime, where the above FOMs are applicable. Higher efficiency is possible, provided that the design of the platform and magnet occurs in a coordinated fashion.

4 IAXO experimental setup

IAXO will follow the basic conceptual layout of an enhanced axion helioscope seen in Fig. 3, implemented into a large superconducting 8-coil toroidal magnet, together with x-ray optics and detectors attached to each of the 8 magnet bores, as shown in Fig. 4. The anticipated values for each of the experimental parameters of the helioscope were approximately quantified in [143], preliminarily organized within ranges from most conservative to most optimistic values. These values were justified by generic technological considerations on the magnet, x-ray optics and detectors. Since then the collaboration has further refined the experimental parameters into a first conceptual design of the experiment. In the following sections, a description is done of the three main elements of the experiment: the superconducting magnet (4.1), the x-ray optics (4.2) and the low background detectors (4.3). The tracking platform that points the magnet to the sun is briefly described in section 4.4 and possible additional equipment associated with extensions of the experiment's physics case is briefly commented in section 4.5.

4.1 The IAXO magnet

The outcome of the figure of merit analysis clearly indicates the importance and need for a new magnet to achieve a significant step forward in the sensitivity to the axion-photon coupling. The design of the new magnet is performed with the magnet's FOM (MFOM) in mind already from the initial design stages. Since practically and cost-wise the currently available detector (i.e. large scale) magnet technology is limited to using NbTi superconductor technology which allows peak magnetic field of up to 5-6 T, the magnet's aperture is the only MFOM parameter that can be considerably enlarged. Consequently, the design of the magnet has started with the focus on this parameter. The conclusion of the preliminary optimization study, conducted at CERN, has shown that the toroidal geometry is preferred for an axion helioscope [143]. Inspired by the design of the ATLAS barrel and end-cap toroids, a large superconducting toroidal magnet is being designed at CERN to fulfill the requirements of IAXO. The new toroid will be built up from eight, one meter wide and 21 m long, racetrack coils. The innovative magnet system is sized 5.2 m in diameter and 25 m in length. It is designed to realize a peak magnetic field of 5.4 T with a stored energy of 500 MJ at the operational current of 12.3 kA.

4.1.1 Figure of merit and lay-out optimization

The general guideline to define the lay-out of the new toroidal magnet has been to optimize the MFOM $f_M = L^2B^2A$, as defined in section 3.3, where L is the magnet length, B the effective magnetic field and A the aperture covered by the x-ray optics. Currently, the MFOM of the CAST magnet is 21 T^{2}m^4. As discussed in [143], an MFOM of 300 relative to CAST is necessary for IAXO to aim at sensitivities to $g_{a\gamma}$ of at least one order of magnitude beyond the current CAST bounds. Accordingly, we have adopted the latter value as the primary design criterion for the definition of the toroidal magnet system, together with other practical constraints such as the maximum realistic size and number of the x-ray optics (section 4.2) and the fact that the design should rely on known and well proven engineering solutions and manufacturing techniques.

To determine the MFOM, the magnet straight section length L is set to 20 m and the integration $\int B^2(x,y)dxdy$ is performed over the *open* area covered by the x-ray optics. Hence, to perform the integration, the telescopes' positioning must be determined. Upon placing the telescopes as close as possible to the inner radius of the toroid R_{in}, the optimized angular alignment of the telescopes is determined by the result of the integration. Two principal options for the angular alignment are considered: one is to

Property		*Value*	*Unit*
Cryostat dimensions:	Overall length	25	m
	Outer diameter	5.2	m
	Cryostat volume	~ 530	m^3
Toroid size:	Inner radius, R_{in}	1.05	m
	Outer radius, R_{out}	2.05	m
	Inner axial length	21.0	m
	Outer axial length	21.8	m
Mass:	Conductor	65	tons
	Cold Mass	130	tons
	Cryostat	35	tons
	Total assembly	~ 250	tons
Coils:	Number of racetrack coils	8	-
	Inner radius of bare coil, relative to racetrack center	500	mm
	Outer radius of bare coil, relative to racetrack center	884	mm
	Inner winding radius in corner	500	mm
Winding dimensions:	Winding pack width	384	mm
	Winding pack height	144	mm
	Length of inner turn	43.1	m
	Length of outer turn	45.5	m
	Turns/coil	180	-
Nominal Values:	Nominal current, I_{op}	12.3	kA
	Stored energy, E	500	MJ
	Inductance	6.9	H
	Peak magnetic field, B_p	5.4	T
	Average field in the bores	2.5	T
Conductor:	Conductor unit length per double-pancake	4.0	km
	Conductor length per coil	8.0	km
	Total conductor length (including reserve)	68	km
	Cross-sectional area	35×8	mm^2
	Number of strands	40	-
	Strand diameter	1.3	mm
	Critical current @ 5 T, I_c	58	kA
	Operating temperature, T_{op}	4.5	K
	Operational margin	40%	-
	Temperature margin @ 5.4 T	1.9	K
Heat Load:	at 4.5 K	$\sim$150	W
	at 60-80 K	$\sim$1.6	kW

Table 1: Main design parameters of the IAXO toroidal magnet.

align each of the telescopes between each pair of racetrack coils, whereas the other is to place the telescopes behind the racetrack coils. Fig. 5 provides a general illustration of the two alignment options for an eight coils toroid. In practice, the two options represent two different approaches: the first, referred to as the "area dominated" option, takes advantage of the entire large aperture of each of the telescopes and the second "field dominated" option assumes that placing the coils behind the optics, and by that including areas with higher magnetic field in the integration, will increase f_M.

Once the position of the telescopes is fixed, the integration over a disc with radius R_{det} centered at (R_{cen}, θ_{cen}) can be performed. Then, the magnetic field is determined by the geometrical and electromagnetic parameters of the magnet. For each lay-out, the magnetic field is calculated using a 3D FEA model and the integration is performed on the mid-plane. The model features an arc at the bent sections of each racetrack with a radius $R_{arc} = (R_{out} - R_{in})/2$, where R_{out} and R_{in} are the outer and inner radii of the racetrack coil windings, respectively. The model also assumes the use of an Al stabilized Rutherford NbTi cable in the coil windings. The winding dimensions are determined from the conductor dimensions assuming a few winding configurations.

The optimization study shows that IAXO's MFOM is affected considerably by the fraction of the aperture of the telescopes exposed to x-rays, thus favoring the area dominated alignment. Even when considering the field dominated alignment, it is preferable to use thinner coils, thus increasing the open

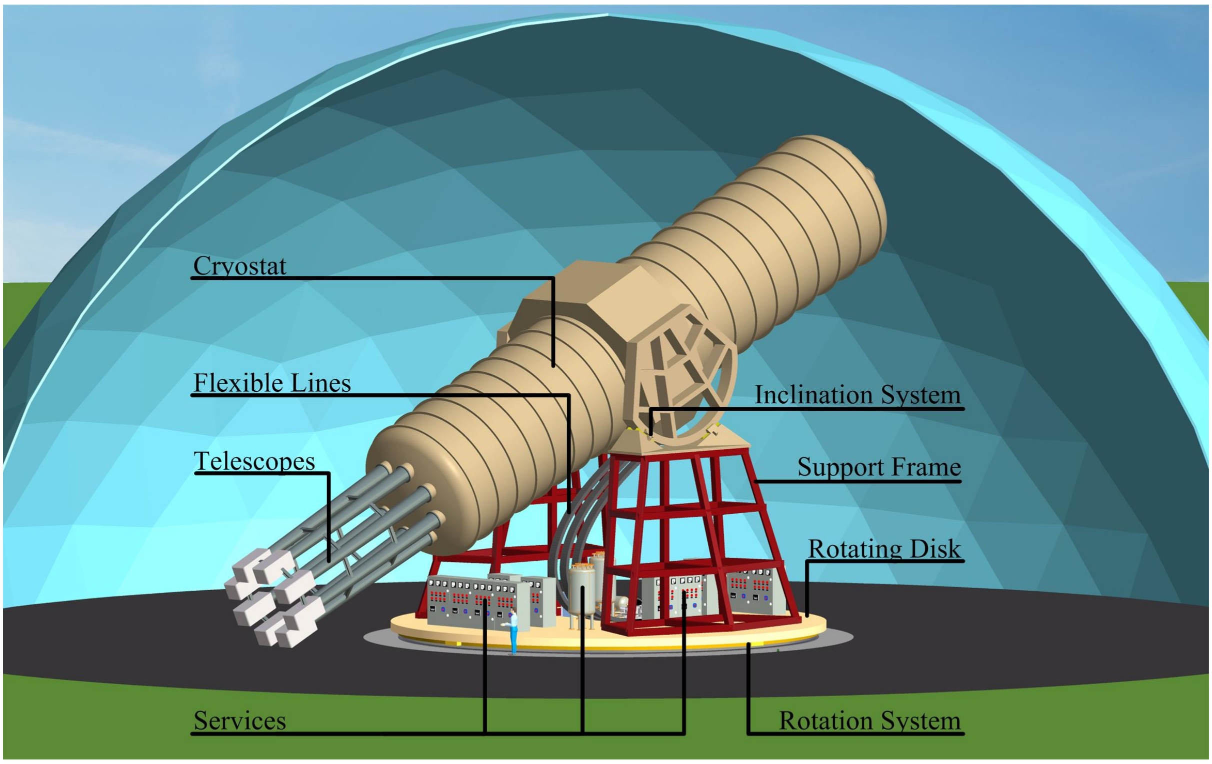

Figure 4: Schematic view of IAXO. Shown are the cryostat, eight telescopes, the flexible lines guiding services into the magnet, cryogenics and powering services units, inclination system and the rotating disk for horizontal movement. The dimensions of the system can be appreciated by a comparison to the human figure positioned by the rotating table.

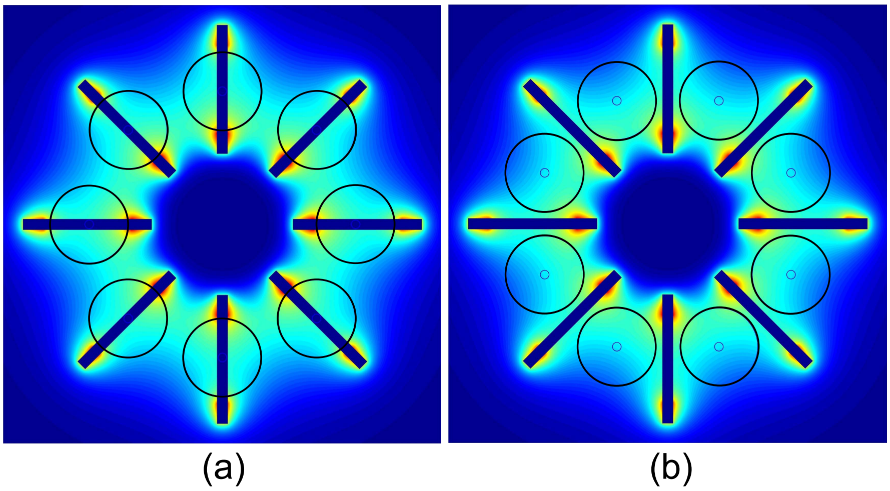

Figure 5: Illustration of the two principle angular alignment options considered for the telescopes with respect to the coils. The rectangles represent the toroid's coil and the circles represent the telescopes' bores. (a) "Field dominated" alignment: telescopes behind the coils. (b) "Area dominated" alignment: telescopes in between the coils.

aperture in front of the telescopes. Moreover, the area dominated option yields a 15% larger MFOM, compared to the field dominated option.

The magnet system design, presented in Fig. 4, follows the result of the geometrical optimization study. The design meets all the experimental requirements of the magnet. It is relying on known and mostly well-proven engineering solutions, many of which were used in and developed for the ATLAS toroids engineered by CERN, INFN Milano and CEA Saclay. This ensures that the magnet is technically feasible to manufacture. The main properties of the toroid are listed in Table 1. The design essentially features a separation of the magnet system from the optical detection systems, which considerably simplifies the overall system integration. This also allows for eight open bores, which are centered and aligned in between the racetrack coils, in accordance with the geometrical study. The inclusion of the eight open bores will simplify the fluent use of experimental instrumentation[†].

The toroidal magnet comprises eight coils and their casing, an inner cylindrical support for the magnetic forces, keystone elements to support gravitational and magnetic loads, a thermal shield, a vacuum vessel and a movement system (see Figs. 4 to 8 and Table 1). Its mass is $\sim$250 tons. At the operational current of 12.3 kA the stored energy is $\sim$500 MJ. The design criteria for the structural design study are defined as: a maximum deflection of 5 mm, a general stress limit of 50 MPa and a buckling factor of 5. The magnetic and structural designs are done using the ANSYS® 14.5 Workbench environment. The Maxwell 16.0 code is used to calculate 3D magnetic fields and Lorentz forces. The magnetic force load is linked to the static-structural branch to calculate stress and deformation. The eight bores are facing eight X-ray telescopes with a diameter of 600 mm and a focal length of $\sim$6 m. The diameter of the bores matches the diameter of the telescopes. The choice for an eight coils toroid with the given dimensions and eight 600 mm diameter telescopes and bores is also determined by a cost optimization within the anticipated budget for construction of the magnet of about 35 MCHF.

[†]An exception to this may be the use of microwave cavities (see section 4.5.4), which could profit from a cryogenic environment to achieve low levels of noise.

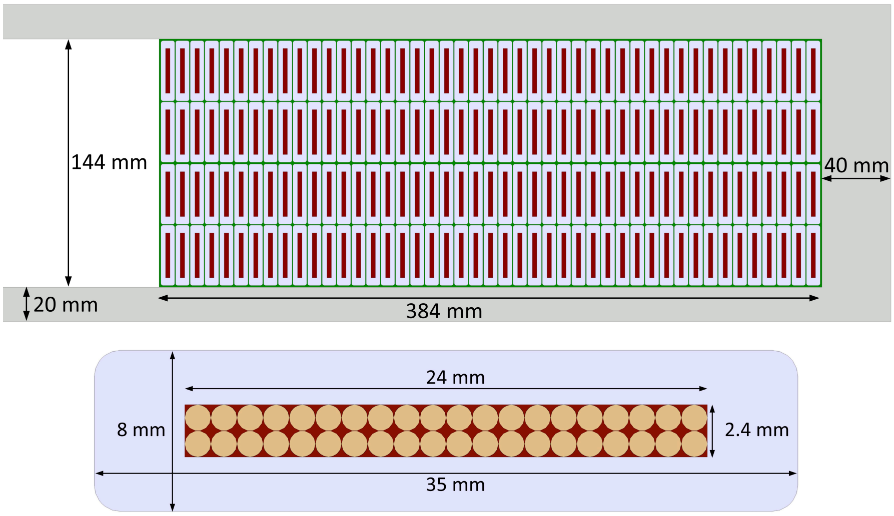

Figure 6: Cross section of the two double pancake winding packs, the coil casing (top) and the conductor with a 40 strands NbTi/Cu Rutherford cable embedded in a dilute Al-0.1wt%Ni doped stabilizer (bottom).

It is worth mentioning that numerous other magnet designs (e.g. accelerator magnets, solenoids and dipole structures) were considered during the optimization study as well [143]. Also, less conventional toroidal designs were examined. For example, ideas for racetrack windings with bent ends were suggested to reduce the area loss when implementing the field dominated alignment. For the same reason toroids with slightly tilted coils were discussed. In general, these designs posses significant technical complications while offering a low potential to significantly enlarge the MFOM and hence deviate from the philosophy behind the magnet concept. In addition, toroidal geometries with more coils and bores were studied essentially to enhance the detection area. The MFOM scales linearly with the number of coils (when keeping the telescopes' cross-section constant), which points out that, as mentioned, the choice for an eight toroid is cost driven in essence.

4.1.2 Conductor

The conductor is shown in Fig. 6. The Rutherford type NbTi/Cu cable, composed of 40 strands of 1.3 mm diameter and a Cu/NbTi ratio of 1.1, is co-extruded with a Al-0.1wt%Ni stabilizer with high RRR, following the techniques used in the ATLAS and CMS detector magnets at CERN [145, 146, 147]. The use of a Rutherford cable as the superconducting element provides a high current density while maintaining high performance redundancy in the large number of strands. The Al stabilizer serves both quench protection and stability for the superconductor. The conductor has a critical current of $I_c(5\ \mathrm{T},\ 4.5\ \mathrm{K}) = 58$ kA.

Peak magnetic field and forces The peak magnetic field in the windings, which determines the operation point of the conductor and the temperature margin, is calculated at 5.4 T for a current of 12.3 kA per turn. In order to minimize the forces acting on the bent sections, the racetrack coils are bent to a symmetric arc shape, with $R_{arc} = 0.5$ m. The net force acting on each racetrack coil is 19 MN, directed radially inwards.

Stability analysis The IAXO magnet requires maintaining the highest possible magnetic field in order to maximize the MFOM. However, suitable operational current and temperature margins are mandatory to ensure its proper and safe operation. For a two double pancake configuration with 180 turns and engineering current density $J_{eng} = 40$ A/mm^2, the peak magnetic field is $B_p = 5.4$ T. Following this, the critical magnetic field corresponding to the magnet load line is 8.8 T at 65 A/mm^2. Hence, IAXO's magnet is working at about 60% on the load line, setting the operational current margin to 40%.

The temperature margin calculation is based on an operational temperature of $T_{op} = 4.5$ K and a peak magnetic field of $B_p = 5.4$ T. A coil with two double pancakes and 45 turns per pancake satisfies this requirement with a temperature margin of 1.9 K, while yielding an MFOM of 300, relative to CAST, thus satisfying the principal design criterion.

4.1.3 Electrical circuit and quench protection

The adiabatic temperature rise in the case of a uniformly distributed quench is ~ 100 K. The toroid's quench protection is based on an active system and an internal dump of the stored energy. The principle of the quench protection system is to rely on a simple, robust and straight forward detection circuits, usage of simple electronics and have sufficient redundancy in order to reduce failure probability.

The electrical circuit of the IAXO toroid is shown in Fig. 7. The magnet power convertor of 12.5 kA is connected at its DC outputs to two breakers, which open both electrical lines to the magnet. The high-T_c current leads are installed within their own cryostat, that is integrated on the rotating gantry of the magnet. The current leads feed the eight coils, which are connected in series, by means of flexible superconducting cables. The flexibility is required to compensate for the changing inclination of the racetrack coils. Each coil is equipped with multiple quench heaters, connected in parallel. Across the warm terminals of the current leads, a slow-dump-resistor with low resistance is connected in series to a diode. The quench detection circuit relies on the detection of normal voltage growth across the toroid following a quench. The voltage sensitivity level of the detectors is 0.3 V, which implies a typical detection delay time of ~ 1 s. The protection circuit is equipped with a timer delay so that false signals do not activate the protection system and lead to a bogus fast discharge.

When a quench is detected and verified, the two breakers open to quickly separate the magnet from the power convertor and a quench is initiated in all coils simultaneously by activating all the quench heaters. This ensures a fast and uniform quench propagation and thus a homogenous cold mass temperature after a quench. Simultaneously, the current is discharged through the dump-resistor. This discharge mode, the so-called fast dump mode, is characterized by an internal dump of the magnet's stored energy, because the magnetic energy is dissipating into heat in the magnet windings. Upon grounding the magnet, the fast discharge scheme ensures that the discharge voltage excitation is kept low enough and that the stored energy is uniformly dissipated in the windings. The internal energy dump depends on the absolute reliability of the quench heaters system. To reduce failure probability to an acceptable level, the quench protection system features a six-fold redundant quench detection circuit with bridges and a two-fold redundant quench heater system with multiple heaters along each of the eight racetracks.

The DC power convertor will operate in voltage control mode when ramping up the toroid and in current control mode during steady operation. The field stability requirement for an axion helioscope is of minor importance. A time stability as large as 0.1% will not affect for the axion-photon conversion probability, and hence in the experiment's sensitivity.

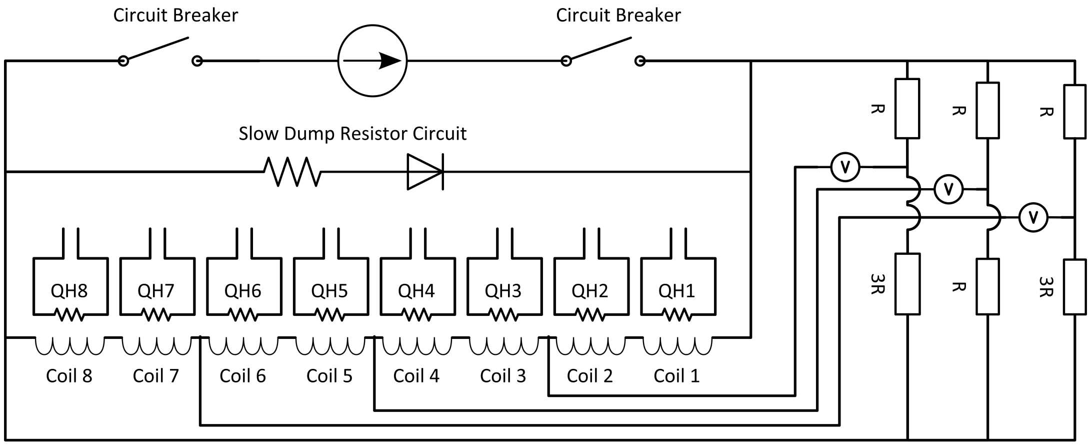

Figure 7: Schematic diagram of the electrical circuit and quench protection scheme. Shown are the power convertor, the eight coils, quench heaters (QH 1-8), the slow dump circuit and the quench detection circuit.

Under normal operation, the toroid will be discharged through the diode-resistor circuit in a passive run down mode (slow discharge mode). Slow discharge is also the safety dump mode activated in the case of a minor fault.

Each of the dump-resistors is connected in series to a diode unit to avoid current driven through the dump resistor circuit during normal operation of the magnet. The dump resistors circuit is air cooled by convection and have the capacity of absorbing the total stored magnetic energy of the toroid.

The longitudinal normal zone propagation velocity is $\sim$6.5 m/s. The velocity was calculated by using COMSOL 4.3b coupled multiphysics modules in a 2D adiabatic model. Hence, the normal zone will propagate around an entire coil (43 m) in 3.3 s.

4.1.4 Cold-mass

The cold mass operating temperature is 4.5 K and its mass is approximately 130 tons. The cold mass consist of eight coils, with two double pancakes per coil, which form the toroid geometry, and a central cylinder designed to support the magnetic force load. The coils are embedded in Al5083 alloy casings, which are attached to the support cylinder at their inner edge. The casings are designed to minimize coil deflection due to the magnetic forces.

To increase the stiffness of the cold mass structure and maintain the toroidal shape under gravitational and magnetic loads, and to support the warm bores, eight Al5083 keystone boxes and 16 keystone plates are connected in between each pair of coils, as shown in Fig. 8. The keystone boxes are attached to the support cylinder at the center of mass of the *whole* system (i.e. including the telescopes and detectors) and the keystone plates are attached at half-length between the keystone boxes and the coils ends.

A coil, shown in Fig. 6, comprises two double pancake windings separated by a 1 mm layer of insulation. The coils are impregnated for proper bonding and pre-stressed within their individual casing to minimize shear stress and prevent cracks and gaps appearing due to thermal shrinkage on cool-down and magnetic forces.

4.1.5 Cryostat and its movement system

The design of the cryostat is based on a rigid central part, placed at the center of mass of the whole system and serves as a fixed support point of the cold mass, with two large cylinders and two end plates enclosing it to seal the vacuum vessel. In addition, eight cylindrical open bores are placed in between the end plates. The vessel is optimized to sustain the atmospheric pressure difference and the gravitational load, while being as light and thin as possible. The Al5083 rigid central piece is 70 mm thick with a thicker 150 mm bottom plate to support the mass of the cold mass. Using two end flanges at the vessel's rims, as well as periodic reinforcement ribs at 1.35 m intervals along both cylinders, the structural requirements are met for a 20 mm thick Al5083 vessel with two 30 mm thick torispherical Klöpper shaped end plates. The 10 mm wall thickness of the eight cylindrical bores is minimized in order for the bores to be placed as close as possible to the racetracks coils inner radius, thereby maximizing the MFOM.

The cold mass is fixed to the central post of the cryostat. The cold mass supports are made of four G10 feet, connecting the reinforced bottom keystone box (referred to as KSB8) to the central part of the cryostat and transfer the weight load of the cold mass to the cryostat. KSB8 also provides a thermal property: the cold mass supports are not directly attached to the coils casings, thereby reducing the heat load on the windings and affecting less the stability of the magnet. The support feet are thermally connected to the thermal shield with copper braids, further reducing the heat load on KSB8. Moreover, KSB8 can be directly cooled to ensure that the magnet stability margins remain at the desired level.

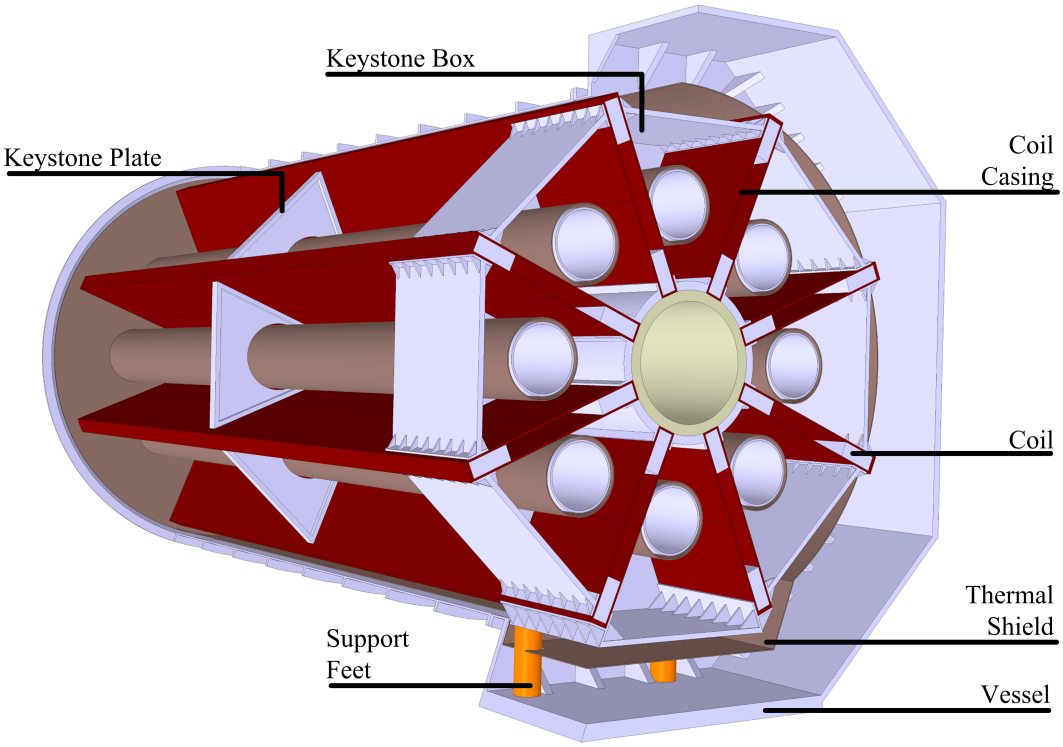

Figure 8: Mid-plane cut of the cryostat with an exposed cold mass, showing the cold mass and its supports, surrounded by a thermal shield, and the vacuum vessel. The open bores will simplify the use of experimental instrumentation.

Mechanical stops, which counteract forces along a specific axis, will be introduced at both ends of the cold mass to reduce the stress on the fixed support feet when the magnet is positioned at different inclination angles.

Searching for solar axions, the IAXO detectors need to track the sun for the longest possible period in order to increase the data-taking efficiency. Thus, the magnet needs to be rotated both horizontally and vertically by the largest possible angles. For vertical inclination a $\pm$ 25° movement is required, while the horizontal rotation should be stretched to a full 360° rotation before the magnet revolves back at a faster speed to its starting position.

The 250 tons magnet system will be supported at the center of mass of the whole system through the cryostat central post (see Fig. 4), thus minimizing the torques acting on the support structure and allowing for simple rotation and inclination mechanisms. Accordingly, an altitude-over-azimuth mount configuration was chosen to support and rotate the magnet system, as described in section 4.4. This mechanically simple mount, commonly used for very large telescopes, allows to separate vertical and horizontal rotations. The vertical movement is performed by two semi-circular structures (C-rings) with extension sections which are attached to the central part of the vacuum vessel. The C-rings distribute support forces from the rigid central part of the vessel to the C-rings pedestals, equipped with elevation hydrostatic pads and drives. The pedestals are mounted on top of a 6.5 m high structural steel support frame which is situated on a wide rotating structural steel disk. The rotation of the disk is generated by a set of roller drives on a circular rail system.

The required magnet services, providing vacuum, helium supply, current and controls, are placed on top of the disk to couple their position to the horizontal rotation of the magnet. The magnet services are connected via a turret aligned with the rotation axis, thus simplifying the flexible cables and transfer lines arrangement. A set of flexible chains are guiding the services lines and cables from the different services boxes to the stationary connection point.

4.1.6 Cryogenics

The coil windings are cooled by conduction at a temperature of 4.5 K. The conceptual design of the cryogenic system is based on cooling with a forced flow of sub-cooled liquid helium at supercritical pressure. This avoids two-phase flow within the magnet cryostat and hence the complexity of controlling such a flow within a system whose inclination angle is continuously changing. The coolant flows in a piping system attached to the coil casings, allowing for conduction cooling in a manner similar to the ATLAS toroids [145, 146]. The decision for using this design is following the same philosophy of our concept: a known technology with a low-cost proven solution and most reliable.

The heat load on the magnet by radiation and conduction is $\sim$150 W at 4.5 K. In addition comes the thermal shield heat load of $\sim$1.6 kW. An acceptable thermal design goal is to limit the temperature rise in the coils to 0.1 K above the coolant temperature under the given heat loads.

Fig. 9 shows a schematic flow diagram of the cryogenic system concept. It features the helium compression and gas management that is ground stationary. The refrigerator cold box, current leads cryostat and a 4.5 K helium bath are integrated on the rotating disk that carries the structure of the helioscope. A helium bath operating at 4.2 K is connected to the magnet cryostat to follow its movement.

The magnet coils are cooled by a helium flow of 23 g/s, supplied at about 300 kPa and 4.6 K and sub-cooled in the 4.5 K bath. Before entering the cooling circuit of the first coil, the flow is cooled to 4.3 K in the 4.2 K bath. After passing through the cooling channels of each coil, the helium, then at below 4.5 K, is re-cooled in the sub-cooler of the magnet cryostat. As the flow returns from the last magnet coil channels, part of the helium is used to supply the 4.2 K sub-cooler and the remaining gas supplies the 4.5 K bath on the rotating disk. The latter flow is also used as a drive flow for a cold injector pump that pumps the 4.2 K sub-cooler at ambient pressure.

The thermal shield is cooled by a flow of 16 g/s gas at 16 bar between 40 K and 80 K. The cooling of the current leads is supplied at 20 K and 1.2 bar, which corresponds to the cooling used for the HTS current leads of the LHC machine [148]. The path of the superconducting cables to the magnets is not shown in Fig. 9 but they could for example be integrated in the helium supply line.

The total equivalent capacity of the refrigerator results in a 360 W isothermal load at 4.5 K. Thus, the refrigerator cold box will be compact enough to be integrated together with the cryostat of the current leads on the gantry that is rotating with the helioscope. All cryogenic lines between the refrigerator and the magnet cryostat will therefore only need to compensate for the $\pm$ 25° inclination, and not for the 360° rotation that will be followed only by ambient temperature lines.

4.1.7 Magnet system reliability and fault scenarios

The IAXO magnet system is a complex combination of subsystems which work in harmony. Therefore, the anticipation of fault scenarios and the basic operational strategy in case of such failures should be dealt with already at the design stage. Here, we identify and describe the major fault cases which could interrupt the normal operation of the system:

- *Cryogen leak:* Minor leaks in the cryogenics pipes will result in exceeding the vacuum system trip limits. In this case the safety system will initiate a slow magnet discharge. In the case of a rupture in the cryogen lines a rapid pressure rise in the vessel will occur. The vessel will remain protected by a set of relief valves, while a fast shut down of the system will be initiated.

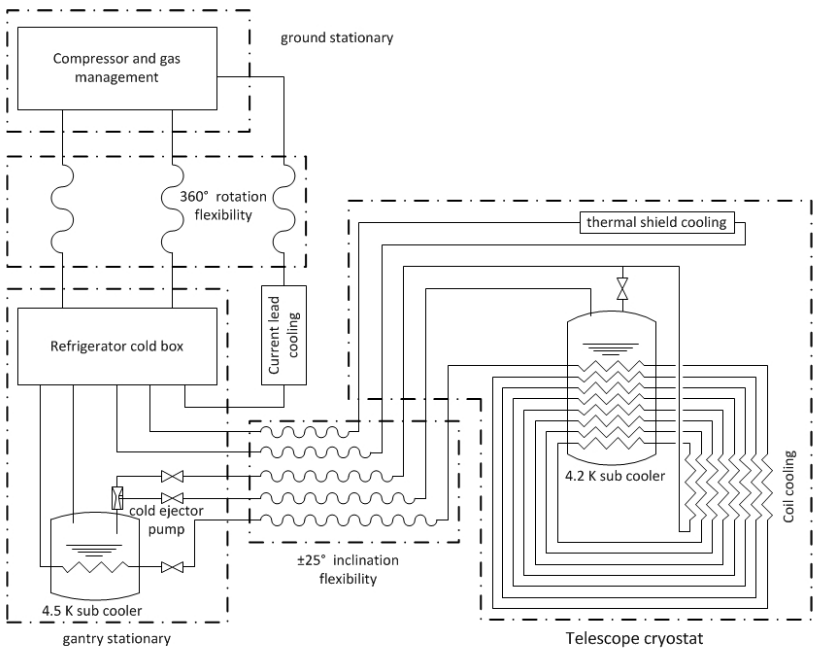

Figure 9: Flow diagram of the cryogenic system of the IAXO magnet.

- *Vacuum failure:* The vacuum system is supported by safety valves, thus decreasing the probability for a catastrophic vacuum failure considerably. Normal vacuum system faults will be dealt with by hard wired interlocks.
- *Quench protection system failure:* Total failure of the quench detection system or the heaters system will be avoided by using multiple detectors and heaters to give redundancy to the system. Nonetheless, the coils and conductors are designed to sustain even such fault conditions so that a complete quench system failure will not lead to coil nor conductor damage.
- *Power failure:* If the mains power will fail to supply power to the magnet control systems, the power supply will be maintained by a UPS. Nonetheless, such a fault scenario will initiate a slow discharge of the magnet.
- *Refrigeration supply failure:* A failure to supply cooling power from the refrigerator cold box to the current leads and bus-bars, thermal shield or the 4.2 K sub-cooler will initiate a slow discharge process.
- *Water supply failure:* Water supply failure to the power converter, vacuum pumps, etc. will result in a slow discharge.
- *Air supply failure:* Air supply is required for the ongoing operation of the vacuum system and the cryogenic system. A deficient air supply to these systems will lead to a slow discharge of the magnet.
- *Seismic disturbances:* The structure and movement system must sustain an additional sidewards load of at least 1.2g, which may be caused by a moderate seismic activity.

System reliability is an important issue when designing a complex assembly of subsystems such as the IAXO magnet system, let alone when the system is required to operate for long periods of time without exterior interference. Some key factors are to be noted when defining the magnet system's reliability: A fast discharge of the magnet should be initiated only when the magnet, experiment as a whole or personal safety is in danger. In all other cases a slow energy dump should take place. A UPS unit will maintain key services in order to enable a safe and controlled slow discharge in extreme cases. Lastly, routine maintenance is essential to avoid false magnet discharges.

4.1.8 Cryostat assembly procedure and integration

The IAXO detector will be placed in a light and confined structure, such as a dome or a framed tent, which will serve as the main site for the experiment. For this reason the assembly requires a hall with enough space to allow for the large tooling and infrastructure needed for the final cold mass and cryostat integration.

The assembly of the cold mass and the cryostat will be performed in five main steps: First, each of the eight warm bores, surrounded by 30 layers of super-insulation and a thermal shield, will be connected to one keystone box and two keystone plates to form eight sub-units. These sub-units will be attached, together with the coils casings, to the cold mass central support cylinder in order to assemble the complete cold mass. Cooling circuits will be installed and bonded to the surface of the coils casings already during fabrication. Additional cooling pipes will be attached to the cold mass when the latter is assembled. Next, the complete cold mass will be connected to the central part of the cryostat, where the cylindrical

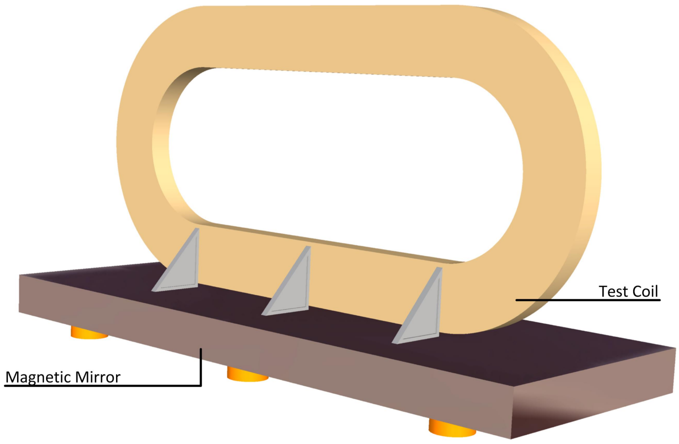

Figure 10: Possible arrangement of the two-meter long prototype coil T0 in combination with a cold iron yoke to generate the windings internal stress and force levels as in the full size detector toroid.

cold mass G10 based supports will be inserted into their their designated slots. The two cylindrical parts of the vessel will be connected to the central part, followed by the enclosure of the cryostat by the two Klöpper end plates which will be connected to the end flanges on both sides of the cryostat cylinders and to the bores. Lastly, the magnet vessel will be transferred to the main site where it will be attached to the movement system. The installation of services lines to the services turret, as well as the integration of the magnet system with the rest of the experiment's systems, will be performed at the last stage of system integration in the main site.

4.1.9 T0 prototype coil for design validation and risk mitigation

Though the design of the toroid is based on the experience gained on the ATLAS toroids, still the IAXO toroid features a peak magnetic field of 5.4 T which is not trivial in terms of superconductor development and training behavior of the coil. In order to validate the design and thereby gain essential manufacturing experience that will flow back in the final manufacturing design, it is highly recommended to construct and test a single short prototype coil, called T0. This coil features the same windings cross section and cold mass design as in the full toroid, see Table 4.1, but its length is limited to two meters for reducing cost and enabling easy performance testing in an existing test facility. A demonstration program for the T0 coil comprises:

- development and procurement of a 200 meter test length of Al stabilized NbTi/Cu conductor, extensive conductor qualification tests, followed by production of the 2x600 meter long units required for the T0 coil;
- coil winding; coil casing production and cold mass integration;
- and finally the performance test of the coil.

Ideally, during the test of the single shorter T0 coil the actual stress and Lorentz forces per meter as present in the full size toroid coil windings should be approximated in order to qualify the mechanical soundness of the coil windings and check its vulnerability for training. This can be achieved by testing the prototype coil at an excess operating current, eventually in combination with a cold-iron mirror temporarily attached to the test coil for this purpose. A test set-up of the T0 coil to be adapted to the constraints of the test facility is shown in Fig. 10. With iron present this arrangement can produce the 50 MPa coil windings stress as in the full toroid at a test current of 14.9 kA (excess of 2.6 kA) and a peak magnetic field of 5.5 T. The pulling force on the straight section of the coil is then some 0.45 MN/m. Without iron a test current of 16.2 kA (excess of 3.9 kA) is needed for generating 50 MPa with 5.6 T peak magnetic field. However, in this case there is no pulling force on the coil inner beam.

It is highly recommended preceding the IAXO magnet construction with the prototype coil as proposed here to finalize the manufacturing design and minimize construction time, thereby mitigating the risk.

4.2 X-ray optics for IAXO

4.2.1 Basic considerations

The purpose of the x-ray optics is to focus the putative x-ray signal to as small as spot as possible, and in doing so, reduce the size of the detector required and, ultimately, the detector background. The performance of an x-ray optic is generally characterized by three basic properties: the point spread function (PSF), the shape of the resultant spot; the throughput, ϵ_o the amount of incident photons properly focused by the optic; and the field-of-view (FOV), the extent to which the optic can focus off-axis photons.

Although x-ray optics can rely on refraction, diffraction or reflection, the large entrance pupil and energy band required for IAXO lead us to only consider grazing-incidence reflective optics. To achieve the smallest spot a, the optics should have as short a focal length, f, as possible since the spot area grows quadratically with focal length, $a \propto f^2$. At the same time, the individual mirrors that comprise the optic should have the highest x-ray reflectivity. Reflectivity increases with decreasing graze angle, α, and since $f \propto \frac{1}{\alpha}$, to achieve the highest throughput the optics should have as long a focal length as possible.

Further complicating the optical design is that the ϵ_o, FOV and PSF of an optic have a complex dependence on the the incident photon energy E and α.

- **Throughput:** there are many choices for the coatings of an x-ray mirror. These coatings can have abrupt changes in reflectivity as a function of energy when the pass-band includes the characteristic absorption edges of the constituent materials. And as already discussed, the reflectivity will be higher with decreasing graze angle.

- **Field-of-view:** The FOV is impacted by a phenomenon referred to a "vignetting," the loss of photons that pass through the entrance aperture of the optic but are not properly focused on the focal plane. Vignetting is more severe at lower graze angles and increases with the off-axis position. Vignetting is a geometric effect and would occur even if the coatings have 100% reflectivity. When realistic coatings, with their own dependence on E, are accounted for, the FOV becomes dependent on the photon energy and decreases at higher energies.

- **Point Spread Function:** The PSF of an x-ray telescope depends on several factors including the basic design, the long spatial frequency errors (usually refereed to as figure errors) and short spatial frequency errors (usually refereed to as finish errors). These first two factors can be accounted for using geometric optics treatments and do not have a formal energy dependence. But like the FOV, once realistic coatings are considered, the PSF can take on a mild energy dependence. Finish errors can be accounted for using wave optics treatments (e.g., scattering theory) that depend on both E

and α. Several authors have shown that the transition between the valid use of geometric and wave optics itself has a dependence on E and α, so the final energy dependence of the PSF is not easily described by a simple relationship.

There are two basic families of reflective x-ray optics: those that employ two reflections to (nearly) satisfy the Abbe sine rule and have excellent imaging properties across its FOV; those that employ a single reflection and have poor imaging properties. The former include a family of designs originally proposed by Wolter and include telescopes and point-to-point imagers; the later include concentrators and collimators.

Since the x-rays produced via the conversion of axions to photons in the IAXO magnet have the same directionality of the axions, the optic need only have a FOV slightly larger than the inner 3 arcminute ($\sim$0.9 mrad) Solar disk, the region of axion production. Moreover, the fact the emission is from a uniformly filled extended region means to first order, a telescope or concentrator with the same focal length, f will result in the same focused spot of $\sim 1.0 \times f_{\rm m}$ mm, where $f_{\rm m}$ is the focal length in meters. The focal length of the optic, be it a collimator or a telescope, depends on the radius of the largest shell and maximum graze angle that can still result in a high reflectivity from the mirror shell. For a telescope, the relationship is $f \propto \frac{\rho_{\rm max}}{4\alpha}$, while for a collimator it is $f \propto \frac{\rho_{\rm max}}{2\alpha}$.

To zeroth order, the x-ray reflectivity at a single energy of a single metal film is near-unity up to a certain angle, called the critical angle, and then zero above that angle. If this were strictly true, a telescope would be the clear winning design for IAXO, since it would have half the focal length, and hence half the spot diameter and one-fourth the area of a collimator.

However, we know that the reflectivity in the $1-10$ keV has a more complex relationship as a function of energy and α. The throughput of the optics will depend on the reflectivity, which in turn depends on the coating material and graze angle, and the optical design, which determines the number of reflections a photon will experience as it passes through the optic: for a collimator, $n = 1$ while for a telescope, $n = 2$.

4.2.2 Fabrication techniques for reflective optics

The x-ray astronomy community has designed, built and flown x-ray telescopes on more than ten satellite missions, and they have developed a number of techniques for fabricating the telescopes. For each technology, we give a brief description and cite examples of telescopes that rely on it. Broadly speaking, telescopes can be classed into two groups that depend on how they are assembled. Segmented optics rely on several individual pieces of substrates to complete a single layer. (The appropriate analogy is the way a barrel is assembled from many individual staves.) Integral-shell optics are just that: the hyperbolic or parabolic shell is a single monolithic piece.

Segmented optics: rolled aluminum substrates Telescopes formed from segmented aluminum substrates were first utilized for the broad band x-ray telescope (BBXRT) that flew on the Space Shuttle in 1990 [149]. Later missions that used the same approach included: *ASCA* [150], launched in 1993; SODART [151], completed in 1995 but never launched; InFocμs [152], a hard x-ray balloon-borne instrument flown in 2004; and *Suzaku* [153], launched in 2005. Aluminum substrates will also be used for the soft and hard X-ray telescopes on the upcoming JAXA Astro-H (also called NeXT) mission, scheduled for launch in 2014 [154].

Segmented optics: glass substrates Although using glass substrates for an x-ray telescope was explored as far as back as the 1980s [155], it was not fully realized until 2005 with the launch of HEFT [156]. HEFT had three, hard x-ray telescopes, each consisting of as many as 72 layers. HEFT was the pathfinder for NASA's *NuSTAR* [157], launched in 2012 and the first satellite mission to use focusing x-ray optics to image in the hard x-ray band up to 80 keV. Each of *NuSTAR's* two telescope consists of 130 layers, comprised of more than 2300 multilayer-coated pieces of glass. Finally, slumped glass is a candidate technology being developed by several groups for future NASA and ESA missions, like ATHENA (see, e.g., [158] and [159]).

Segmented optics: silicon substrates Another technology being pursued for ATHENA are silicon pore optics [160], which consists of silicon wafers that have a reflective coating on one side and etched support structures on the other. Individual segments are stacked on top of each other to build nested layers. Prototype optics have been built and tested, but there are no operational x-ray telescope yet to use this method.

Integral shell optics: replication Replicated optics are created by growing the mirror, usually a nickel-based alloy, on top of a precisely figured and polished mandrel or master. The completely-formed shell is separated from the mandrel, and a two unique mandrels are required for each individual layer (one for the parabolic-shaped primary, another for the hyperbolic-shaped secondary). Missions that have utilized replicated x-ray telescopes include: *XMM* [161], launched in 1999; *Beppo-SAX* [162], launched in 1996; *ABRIXAS* [163], launched in 1999; the balloon-borne HERO mission [164], first flown in 2002; and the sounding rocket mission FOXSI [], currently under development.

It is important to mention that CAST currently employs a flight-spare telescope from *ABRIXAS*.

Integral shell optics: monolithic glass For completeness, we mention telescopes formed from monolithic pieces of glass. Although these telescopes have excellent focusing quality and have produced some of the best images of the x-ray sky, because of the cost and weight, no future mission is expected to use this approach. Missions that have utilized monolithic optics include: *Einstein* [165], launched in (1978); *RoSAT*, [166] launched in 1980; and the *Chandra X-ray Observatory* [167], launched in 1998.

4.2.3 The baseline technology for IAXO

For IAXO, we have adopted segmented, slumped glass optics as the baseline fabrication approach for several reasons. First, the technology is mature and has been developed by members of the IAXO collaboration, most recently for the NuSTAR satellite mission. Second, this approach easily facilitates the deposition of single-layer or multi-layer reflective coatings. Third, it is the least expensive of the fabrication techniques. Fourth, the imaging requirement for solar observations for IAXO is very modest– focusing the central 3 arcminute core of the Sun. Although other optics technologies may have better resolution than slumped glass, they would not produce a significantly smaller focused spot of the solar core.

4.2.4 The IAXO x-ray telescopes

Design and optimization of the IAXO x-ray telescopes

The optical prescription and reflective coatings were identified by a systematic search of a multi-dimensional parameter space that accounted for the detector efficiency, axion spectrum, optics properties and recipe

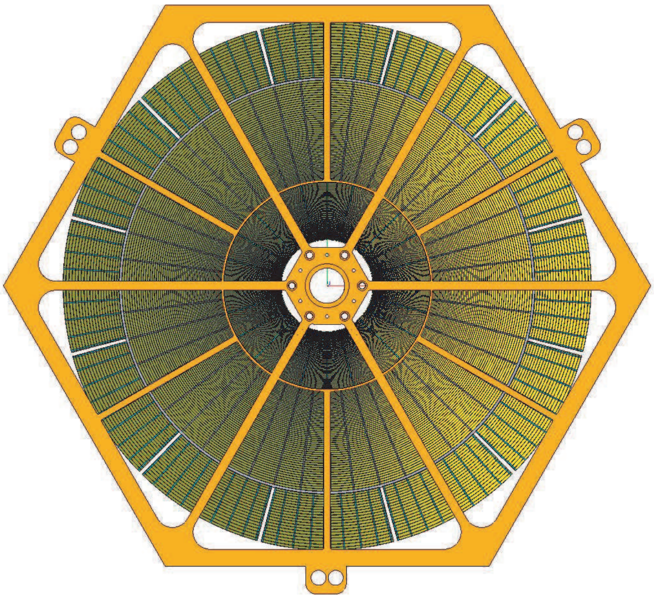

Figure 11: Above: An edge-on view of one IAXO optic, including the hexagonal “spider” structure that will be used to mount the optic into the magnet bores. The thousands of individual mirror segments are visible.

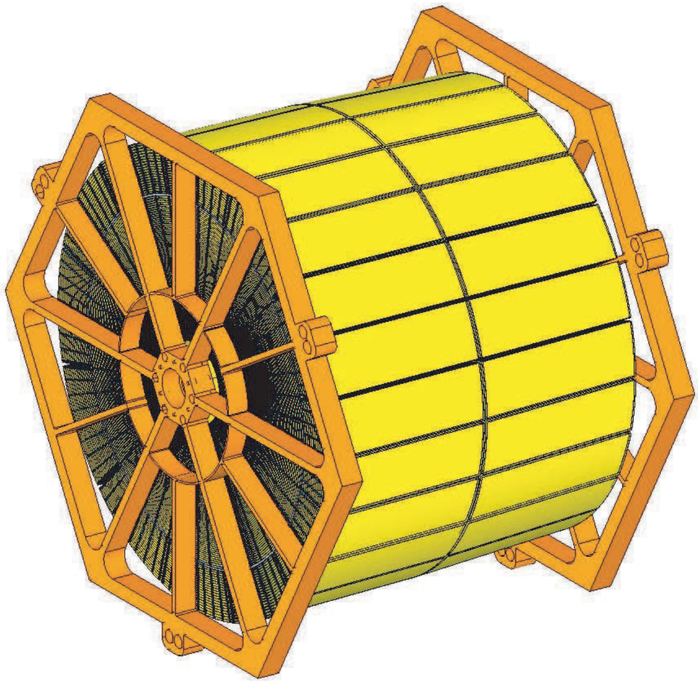

Figure 12: An isomorphic side-view of the telescopes and the spider mounting structures.

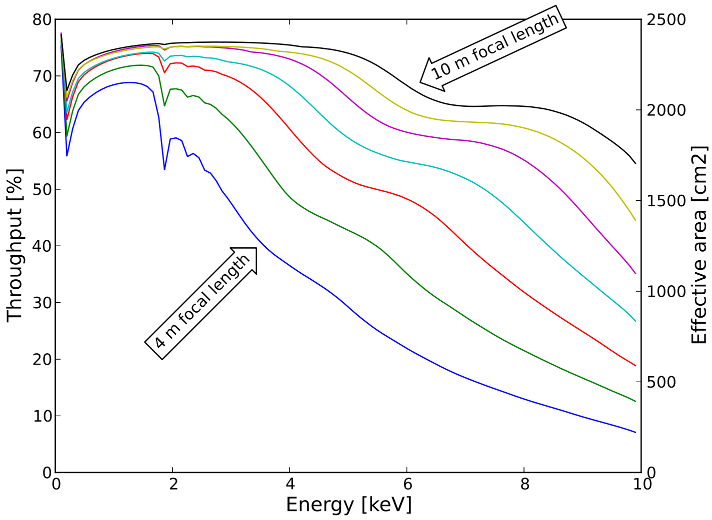

Figure 13: Effective area (right axis) and throughput/efficiency (left axis) versus photon energy for a single telescope for different focal lengths considered, from $f = 4$ m (lowest curve) up to $f = 10$ m (highest curve). Effective area grows as the focal length is increased.

of the reflective coatings. The total optics and detector figure of merit, f_{DO} was then computed. The optical prescription and multilayer recipes presented below produced the highest f_{DO}. It is incredibly important to note that the telescope optimization **must** account for the axion spectrum and detector efficiency and cannot be performed independently. If this process does not include these energy dependent terms, f_{DO} will not achieve the highest possible value.

Telescope prescriptions were generated for designs that had a fixed maximum radius of 300 mm and a minimum radius of 50 mm, with the focal length varied between 4 and 10 m, in increments of 1 m. As the focal length is increased and the graze angle, α decreases and the number of nested layers increases. For example, the $f = 4$ m design has 110 nested layers, while the $f = 10$ m design has more than 230 layers.

Traditionally, x-ray telescopes have relied on single layer coatings of metals like Au or Ir to achieve high throughput in the $1-10$ keV band. More recently, missions designed for hard x-ray observations, like NuSTAR and ASTRO-H, have employed multilayer coatings to achieve high reflectivity up to $\sim$80 keV. We explored using combinations of both for IAXO. Although it is theoretically possible to optimize the coating for each layer of the telescope, this would impose a high penalty in resources when depositing multilayers on the substrates. Instead, we divided the layers into ten sub-groups, with each sub-group of layers receiving the same multilayer coating. A similar strategy was successfully implemented for NuSTAR [168], and this approach allowed the multilayer deposition tools to be used efficiently.

Material types investigated were single layers of W and W/B_4C multilayers. Other types/combinations to consider are W/Si, Pt/B_4C, Ir/B_4C and Ni/B_4C. W/B_4C and W/Si are well understood coatings for x-ray reflectivity and considerably less expensive to use W than Pt or Ir. Using B_4C instead of Si as the light material will give increase reflectivity at $1-4$ keV, but also gives slightly higher stress in the coating. Ni/B_4C coatings are not well understood and can give a high interfacial roughness between light and heavy material, but performs similar to W/B_4C and Ir/B_4C at $1-10$ keV.

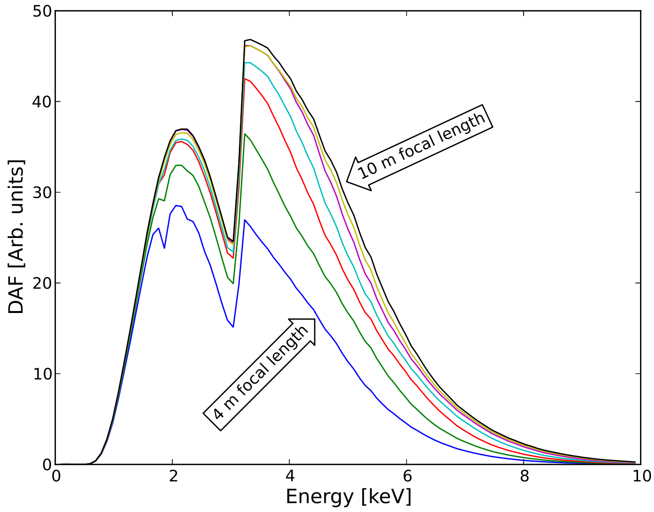

Figure 14: DAF versus photon energy E for a single telescope, and for the different focal lengths considered, from $f = 4$ m (lowest curve) up to $f = 10$ m (highest curve). The significant structure now present is due to absorption edges in detector and coating materials and the shape of the solar axion spectrum.

At a given substrate incident angle, α, the coating geometry was optimized by trying every combination in a parameter space of n (number of bilayers), $d_{\min}$ (minimum bilayer thickness), $d_{\max}$ (maximum bilayer thickness) and Γ , the ratio between the thickness of the heavy material with respect to the total thickness of the bilayer. For every combination, the x-ray reflectivity was calculated using IMD [169]. One of the basic properties of any x-ray telescope is the effective area, EA, the energy-dependent effective aperture of the telescope that accounts for finite reflectivity of individual mirror elements and physical obscuration present in the telescope (e.g., from the support structures used to fabricate the optics and the finite thickness of the substrate which absorb incoming photons). The effective area of an individual layer i is given by:

$$\mathrm{EA}(E)_i = \mathrm{GA}_i \times R_i(E,\alpha)^2 \times 0.8, \tag{12}$$

where GA_i is the projected geometric area of the individual layer i, $R_i(E,\alpha)$ is the reflectivity of the coatings on layer i and the constant factor of 0.8 accounts for obscuration. The total area is given by:

$$\mathrm{EA}(E) = \sum_{i=1}^{N} \mathrm{EA}_i(E), \tag{13}$$

where N is the total number of layers. Figure 13 shows the expected behavior of the effective area increasing as the focal length grows. Again, this behavior arises from the fact that longer focal lengths results in shallower incident angles, and reflectivity increases with decreasing graze angles.

The energy-dependent optics throughput or efficiency, $\epsilon_o(E)$, is simply the $\mathrm{EA}(E)$ divided by the geometric area of the entrance pupil:

$$\epsilon_o(E) = \frac{\mathrm{EA}(E)[\mathrm{m}^2]}{\pi(0.3^2 - 0.05^2)[\mathrm{m}^2]} \tag{14}$$

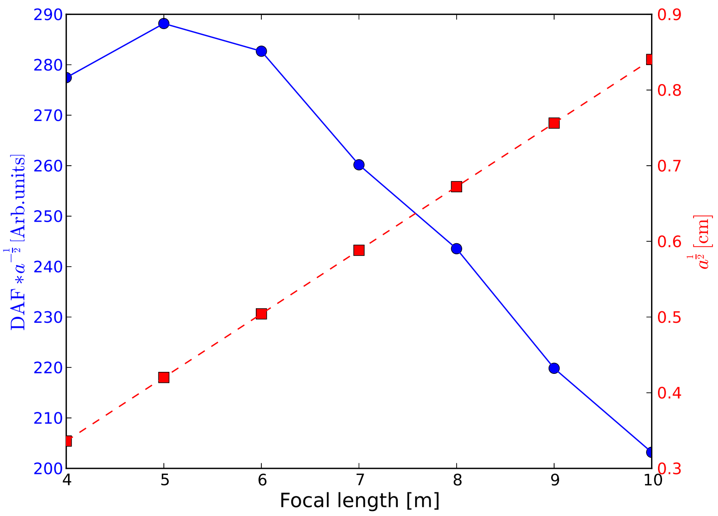

Figure 15: Value of the focal spot size $\sqrt{a}$ (red squares and dashed line, right axis) and the figure of merit DAF$/\sqrt{a}$ (blue circles and solid line, left axis) versus focal length f. The optimal figure of merit is found for $f = 5$ m.

The plot of Fig. 13 displays this quantity for different focal lengths.

In order to build a meaningful figure or merit we multiply the optics throughput by the energy-dependent axion flux $\frac{d\phi}{dE}$(E) and detector efficiency $\epsilon_d(E)$. The resulting quantity, that we call "detected axion flux" (DAF(E)),

$$\mathrm{DAF}(E) = \sum_{i=1}^{N} \mathrm{EA}_i(E) \times \epsilon_d(E) \times \frac{d\phi}{dE}(E) \tag{15}$$

is actually proportional to a hypothetical axion signal in IAXO, and is plotted in Fig. 14.

To find the optimal focal length, we need to maximize the sum of the DAF from $1-10$ keV divided by the square root of the spot size, a quantity proportional to f_{DO}:

$$f_{DO} \equiv \frac{\epsilon_d \epsilon_o}{\sqrt{ba}} \propto \sum_{E=1\ keV}^{10\ keV} \left(\frac{\mathrm{DAF}(E)}{\sqrt{a}} \right). \tag{16}$$

The only quantity left to compute is the spot-size, a. The point-spread-function (PSF) of any x-ray telescope has a complex shape, and the spot-size is computed by first taking the integral of the PSF to compute the encircled energy function (EEF), a measure of how much focused x-ray light is contained within the diameter of a particular size. For example, a common measure of the focusing quality of an x-ray telescope is to determine the 50% value of the EEF, that is determine the smallest diameter extraction region that contains 50% of the power. This is often referred to as the half-power diameter or HPD.

The spot-size will depend on both the physical size of the object imaged, in this case the 3 arcminute (0.87 mrad) central core of the Sun, and the intrinsic imaging capability of the x-ray optic, i.e. the size of the resultant spot when the telescope images a point-like source. To first order, then, the overall spot size s_{total}, measured in angular extent, will be the root mean square of the object size s_{obj} and the optic

Telescopes	8
N, Layers (or shells) per telescope	123
Segments per telescope	2172
Geometric area of glass per telescope	0.38 m^2
Focal length	5.0 m
Inner radius	50 mm
Outer Radius	300 mm
Minimum graze angle	2.63 mrad
Maximum graze angle	15.0 mrad
Coatings	W/B$_4$C multilayers
Pass band	$1-10$ keV
IAXO Nominal, 50% EEF (HPD)	0.29 mrad
IAXO Enhanced, 50% EEF (HPD)	0.23 mrad
IAXO Nominal, 80% EEF	0.58 mrad
IAXO Enhanced, 90% EEF	0.58 mrad
FOV	2.9 mrad

Table 2: Main design parameters of the IAXO x-ray telescopes.

quality s_{opt}:

$$s_{total} = \sqrt{s_{obj}^2 + s_{opt}^2} \tag{17}$$

Based on the performance of the NuSTAR x-ray telescopes [157], we assume for the nominal design of the telescopes a HPD of 1 arcmin (0.29 mrad) and an 80% EEF of 2 arcmin (0.58 mrad). The angular spot size then becomes:

$$s_{total} = \sqrt{s_{obj}^2 + s_{opt}^2} = \sqrt{0.87^2 + 0.58^2} = 1.0 \text{ mrad} \tag{18}$$

As discussed above, the spatial diameter of the spot is simply $f \times s_{total}$ and the spot area becomes:

$$a = \frac{\pi}{4} \left(s_{total} \times f\right)^2 \tag{19}$$

Properties of the IAXO x-ray telescopes

Fig. 15 shows $\sqrt{a}$ as well as f_{DO}, as calculated in Eq. 16, as function of the focal length. The optimal focal length is found to be $f = 5$ m. This parameter and the considerations exposed in previous sections fix the design proposed of the IAXO optics. Different engineering draawings of the optics are shown in Fig. 11 and 12, where the 123 nested layers can be seen. Finally, its main design parameters are listed in Table 2.

4.2.5 Final considerations

Our preliminary scoping study has made simplifying assumptions that will be revisited for the final design study.

- We have assumed the axion spectrum and intensity is uniformly emitted from a region 3 arcmin in extent. We must include the actual distributions in a full Monte Carlo model of the system performance.
- We have computed effective area for an on-axis point source. When the solar extent is included in ray-tracing, the area will decrease by a small amount.
- We have not accounted for non-specular scattering.
- We have assumed the encircled energy function (EEF) evaluated at 50% (i.e., the half-power-diameter) is 1 arcminute and the EEF evaluated at 80% is 2 arcminute.
- We have only coarsely studied how the focal length f influences the FOM in increments of 1 m.

4.3 Ultra-low background x-ray detectors

The baseline technology for the low background x-ray detectors for IAXO are small gaseous detectors (Time Projection Chambers), with a thin window for the entrance of x-rays and a pixelated Micromegas readout, manufactured with the microbulk technique. This kind of detector has already been used in CAST, and has been the object of intense development in recent years, mainly within the T-REX R&D project [170, 171, 172], funded by the European Research Council (ERC). The CAST microbulk detectors have achieved record levels of background and, as described below, they offer the best prospects to meet the requirements for IAXO.

4.3.1 State of the art

The detection concept is sketched on the left of figure 16. The x-rays coming from the magnet enter the detector via an thin window (e.g. aluminized mylar), which is also the cathode of the TPC. This

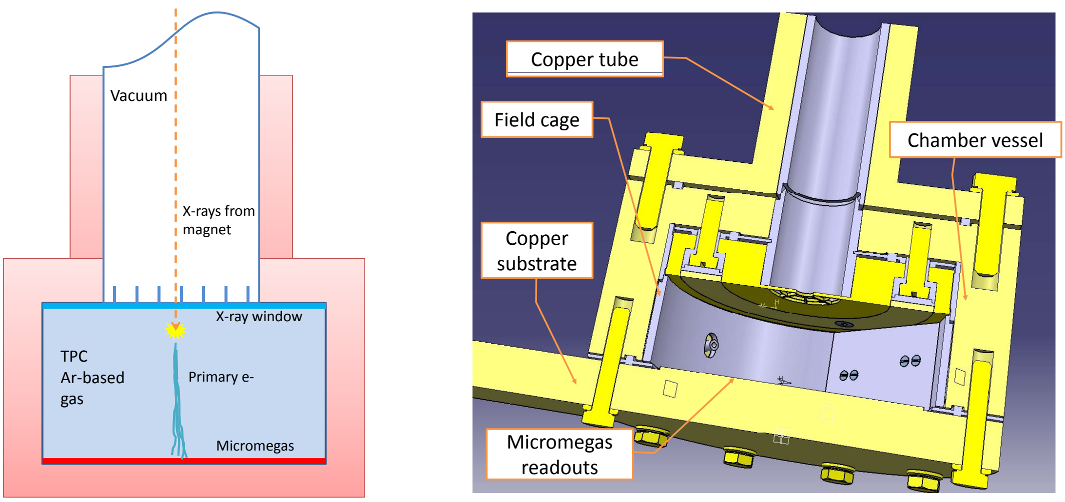

Figure 16: Left: Scheme of the detection principle of Micromegas detectors in IAXO. Right: Design of the IAXO detector prototype

window holds the detector gas, so it must be sufficiently gas-tight and withstand the pressure difference, while being sufficiently transparent to the x-rays so not to affect the efficiency of the detector. The drift distance z of the TPC is adjusted so that the conversion volume contains enough gas to efficiently stop x-rays of the required energies. The design choice in CAST detectors has been $z = 3$ cm at 1.5 bar of an argon gas mixture (usually Ar$-$2.3% isobutane). The primary charge created by the interaction of x-rays drifts towards the anode of the TPC, where it is amplified by a Micromegas structure.

Micromegas readouts [173, 174] make use of a metallic micromesh suspended over a (usually pixellised) anode plane by means of insulator pillars, defining an amplification gap of the order of 50 to 150 μm. Primary electrons go through the micromesh holes and trigger an avalanche inside the gap, inducing detectable signals both in the anode pixels and in the mesh. It is known [175] that the way the amplification develops in a Micromegas gap is such that its gain G is less dependent on geometrical factors (the gap size) or environmental ones (like the temperature or pressure of the gas) than conventional multiwire planes or other types of micropattern detectors based on charge amplification. This fact allows in general for higher time stability and spatial homogeneity in the response of Micromegas, in addition to better energy resolution.

These advantages together with the possibility of easily building large areas, its robustness, the relative cost-effectiveness and the high flexibility in patterning the anode plane, has spread the use of Micromegas in many areas of high energy physics. There are several fabrication techniques of Micromegas, but we focus on a recent one, *microbulk* Micromegas [176], originally developed at CERN and CEA. In these readouts the Micromegas amplification structures are obtained out of a double-clad kapton sheet, by

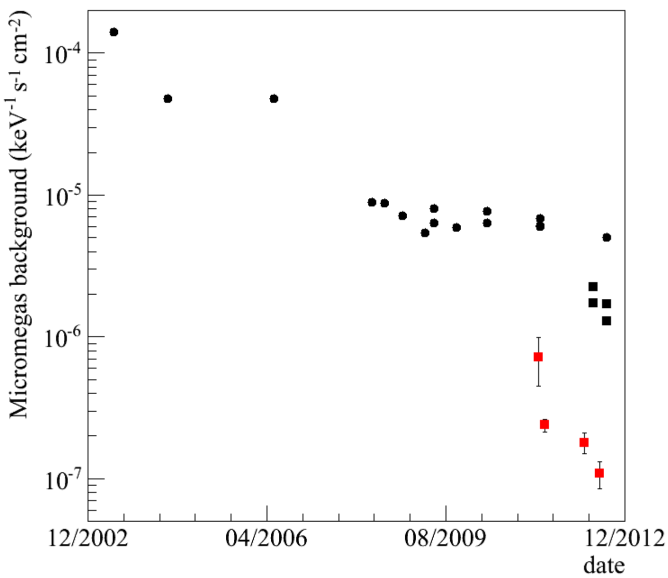

Figure 17: Micromegas background history since the first detector installation in 2002. The black points correspond to the values obtained with the different detectors in the CAST hall. Red points correspond to the values obtained with different shielding configuration in the Canfranc Underground Laboratory.

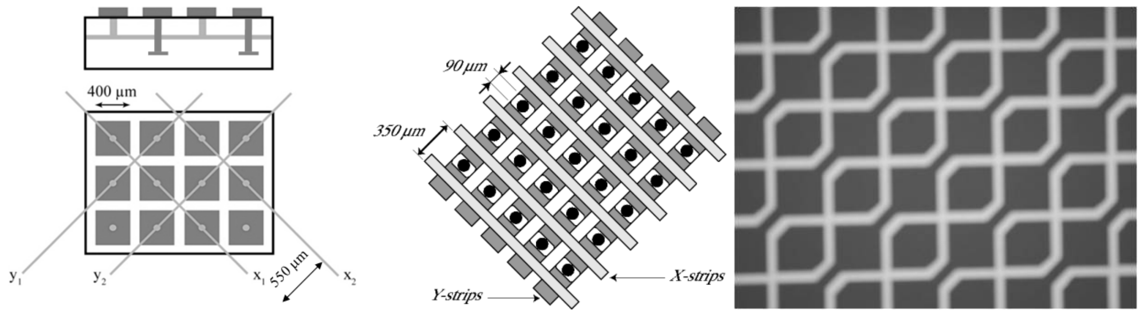

(a) (b) (c)

Figure 18: (a) Sketch of the 2-D readout strategy used in CAST; (b) shows the first pattern of strips and pads used in the first detectors and (c) the most recent pattern based on interconnected pads.

chemically removing part of the kapton. This technique is known to yield the highest precision in the gap homogeneity and, because of that, the best energy resolutions among Micropattern detectors. Moreover, because of the raw materials, microbulk Micromegas are very radiopure objects [177], a desirable property in low background applications. Since the development of this type of Micromegas, these detectors have been studied, proposed or applied in an increasing number of low background applications [170]. Indeed, the first microbulk detectors have been used for the first time in a real data taking in CAST. In its turn, CAST has been a test bench for this technology, that has evolved throughout the lifetime of the experiment.

The plot of figure 17 shows the Micromegas background history in CAST. The black points correspond to nominal background of data taking campaigns in the experiment, while red points correspond to the background level obtained in special runs in a test set-up located underground, at the Laboratorio Subterráneo de Canfranc (LSC). They always represent the average background in the energy region of interest $2-7$ keV. The improvements obtained over time are due to continuous development of the detector setups. These improvements regard the following aspects:

- **Anode patterning:** The use of a gaseous medium for the conversion volume allows to use information of the ionization topology of the events as a handle to identify signals and reject background. To effectively use it the readout needs to be patterned with rather high granularity. Microbulk planes naturally allow for highly granular patterning and indeed, CAST detectors were the first 2D Micromegas readouts. Fig. 18 shows different pattern concepts used in the CAST detectors, always with a pitch below 500 μm.

- **Fabrication technology:** As mentioned before, microbulk Micromegas enjoy several improvements over more conventional techniques. Since their first application in CAST, the manufacturing process has been refined and consolidated.

- **Radiopurity:** The raw material of microbulk readouts (i.e., double-clad kapton foils) as well as fully built readouts have been measured in underground Ge detectors [178] and proven to be very radiopure materials. Moreover, a continuous effort have been made to study the radioactivity of other components of the detector body (chamber, x-ray window, screws, gas gaskets, connectors, etc.) and replace them with radiopure versions.

- **Shielding:** Increasingly powerful passive and active shielding setups have been designed to reduce the contribution of external gammas to the detector background. Although shielding concepts from underground experimentation can be borrowed, care must be paid to the specificities of our case, e.g., the space and weight constraints of the moving platform, the operation at surface (presence of cosmic rays), the geometry imposed by the magnet (the shielding will always have an opening from which the signal x-rays reach the detector) and the intrinsic sensitivity and rejection capability of the Micromegas detectors. The most recent version of the CAST Micromegas shielding, based on a 10 cm thick pure lead shielding around a core of electroformed copper, is shown (partially built) in figure 19.

- **Offline rejection algorithms:** The detailed information obtained by the patterned anode, complemented with the digitized temporal wave-form of the mesh, is the basis to develop complex algorithms to discriminate signal x-ray events from other type of events. The power of this discrimination is highly coupled to the quality of the readout so that improvements in readout design or manufacturing yield improvements in discrimination power. The raw background in the energy region of interest (1 to 10 keV) is normally reduced by a factor of about 10^2 – 10^3 only by offline discrimination.

As indicated in Fig. 20, the lowest background achieved by Micromegas detectors in CAST is of 2×10^{-6} counts keV^{-1} cm^{-2} s^{-1} (sunset Micromegas detectors, 2012 data taking Run). In special setups underground, levels of $\sim 10^{-7}$ counts keV^{-1} cm^{-2} s^{-1} have been achieved. For IAXO we aim at background levels of at least $\sim 10^{-7}$ counts keV^{-1} cm^{-2} s^{-1} and if possible down to $\sim 10^{-8}$ counts keV^{-1} cm^{-2} s^{-1} (lower levels do not translate into better sensitivity as we reach the zero background situation for the exposure considered for IAXO). Below we describe the status of our knowledge of the background limiting factors, and the prospect to further improvement to reach levels required by IAXO.

4.3.2 Main sources of background: current understanding

The improvements obtained are result of the progressive understanding of background sources and their eventual rejection. This understanding has been achieved by a vigorous program of experimental tests and detailed simulations. Given that the final background level in a Micromegas detector is dependent

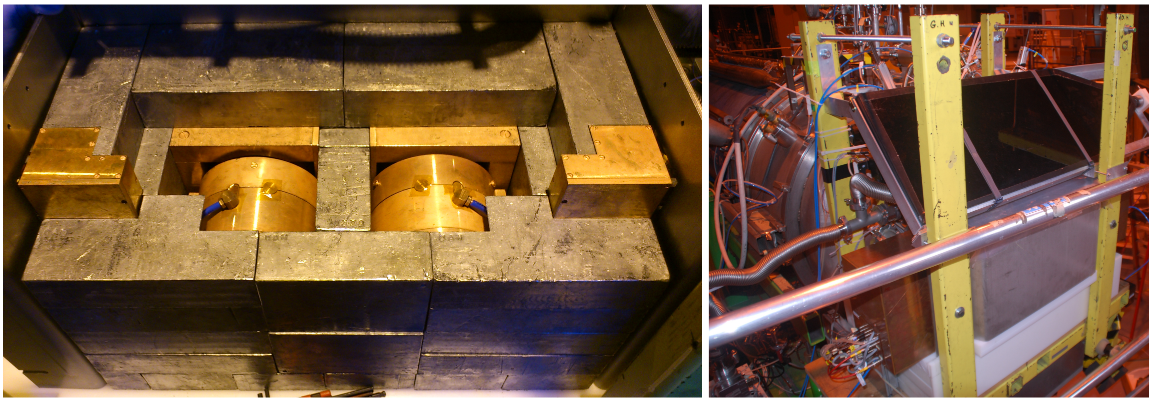

Figure 19: Left: picture of the CAST sunset side setup (incomplete), showing the inner copper shielding surrounded by pure lead pieces. Right: picture of the complete setup with the cosmic muon veto.

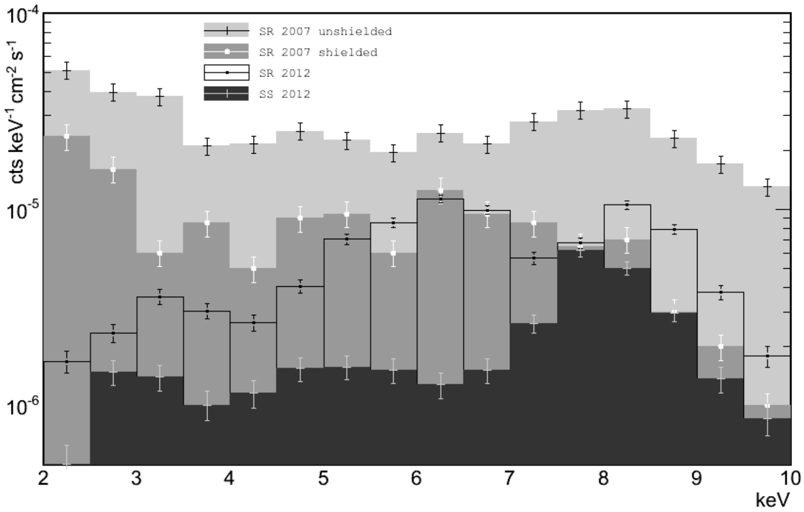

Figure 20: Evolution of the CAST micromegas background spectra since 2007. The lowest spectrum corresponds to the 2012 sunset data after the last improvement in shielding and the implementation of the cosmic muon veto.

on the application of the offline cuts on a number of event features, one needs complex simulations to reproduce the final background level from a given external radiation source. These simulations include not only Geant4-like simulations of particle transport and interaction through the detector setup, but also the full response of the detector, from the generation of the primary ionization in the conversion volume, to the drifting and diffusion of the electrons, amplification and induction of electronic signals in the electrodes. The level of reproduction of the full detector response is currently very remarkable, and has been validated by means of calibrations and specific tests with gamma sources. Simulated data are generated with the very same format as real data from the DAQ, and they undergo the same analysis chain as the latter.

The background of the first generations of CAST Micromegas detectors was dominated by the external gamma radiation, and therefore most early efforts were directed towards quantifying and reducing it. Fig.20 shows several experimental spectra obtained in different CAST setups from 2007 until 2012. In the next-to-last detector setup (labelled SR2012 in Fig.20), and using the simulation tooling developed, the external gamma radiation was quantified to contribute to about $\sim 1.5 \times 10^{-6}$ counts keV^{-1} cm^{-2} s^{-1} in the 2-7 keV range, the actual simulated spectrum being shown on the left of Fig. 21. Although many different uncertainties affect these type of simulations (e.g., the precise spectrum and distribution of the simulated external gamma radiation) we consider this estimate accurate within a factor of 2-3. The shape of the spectrum also gives useful information, as it is populated by fluorescence peaks, produced by the remaining gammas reaching the innermost copper parts of the detector, or by gammas interacting in the stainless steel pipe that connects the detector to the magnet. This estimation is corroborated by experimental tests performed in CAST, as well as in test benches reproducing the same setups, both at surface and underground. This insight was used to design the last version of the shielding (labelled SS2012 in Fig. 20), that should have reduced this contribution by, at least, one order of magnitude. The actual improvement, as shown in Fig. 20, was more modest, due to the fact that cosmics have become the dominant source of background.

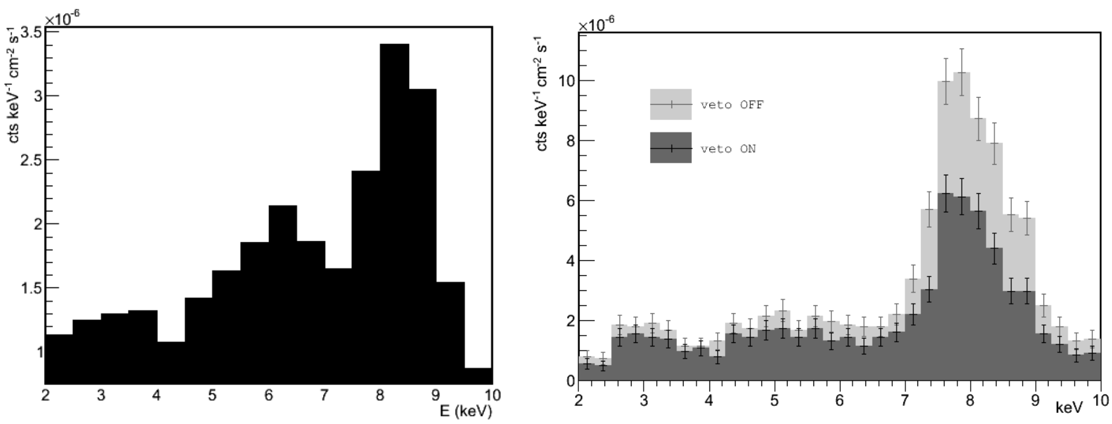

Figure 21: Left: simulated background spectrum induced by external γ flux. Right: background spectra in the CAST sunset Micromegas detectors in the 2012 Run, with and without the anticoincidence with the muon veto. About 25% of the background in the 2-7 keV window are tagged as comic-induced. Given the modest coverage of this veto, the result is compatible with the conclusion that most of the current background is dominated by cosmics.

As mentioned before, the current experimental background level is of 2×10^{-6} counts keV^{-1} cm^{-2} s^{-1} . According to our current best knowledge, this level is dominated by cosmics (muons) that cross the shielding and produce secondaries (mostly fluorescences) in the innermost parts of the setup, populating the low energy part of the spectrum. This assumption is sustained by tests done with partial-coverage muon veto working in anticoincidence (see Fig. 21). A well-designed high-coverage active veto should be able to reduce this component of the background by one or two orders of magnitude. Efforts in this direction are planned for the near future as explained below in 4.3.3.

Finally, another component of the background is the one induced by radioactivity from the detector components themselves. The current detector setup has undergone several redesigns and replacements of components regarding radiopurity (window strongback of copper instead of aluminium, gas inlets of copper instead of brass, etc.), and we estimate that the remaining internal radioactivity contributes to the detector background to, at the maximum, $\sim 2\times10^{-7}$ counts keV^{-1} cm^{-2} s^{-1} . This level has been experimentally obtained in special shielding setups at LSC, in which both gamma (by full 4π shielding) and cosmics (by operation underground) are reduced to negligible levels.

In summary, while current background levels at CAST are at the $\sim 10^{-6}$ counts keV^{-1} cm^{-2} s^{-1} level, reduction to close to $\sim 10^{-7}$ counts keV^{-1} cm^{-2} s^{-1} level seems at hand by an adequate design of an active veto. Further reduction below that level seems also realistic in the mid-term as a result of the ongoing campaign to identify and replace radioactive components of the detector. At lower levels of background we cannot exclude unidentified contributions from gammas entering through the remaining openings of the shielding facing the magnet, but they could be rejected by subsequent improvements in the shielding design.

4.3.3 A demonstrating prototype of ultra-low background Micromegas detector for IAXO

As part of a coordinated effort to test both the optics and detector technologies proposed for IAXO, we are currently building a new version of Micromegas detector aiming at a further improvement in background level. This detector will be designed to operate at the focal point of the prototype x-ray optics described in 4.2. The combined set will be installed at the CAST sunrise side and will take physics data during 2014, giving precious operational experience on this combination of technologies for IAXO.

The new detector will be based on the current design, but will incorporate improvements from the results and considerations exposed before. The detector aims at reducing the background level down to, possibly, $\sim 10^{-7}$ counts keV^{-1} cm^{-2} s^{-1} . As argued previously, this level is feasible by improving the active and passive shielding. The main features of the new design are the following:

- **Shielding:** The new shielding will extend the concepts successfully tested in the 2012 CAST sunset setup. It will enclose better the detector geometry further reducing the opening solid angle in the direction of the magnet (taking advantage of the focusing of the optics). Active shielding with muon veto will also be also used, and a teflon coating will block fluorescence from the vacuum pipe.
- **Detector chamber:** Shown on the right of Fig. 16, the new chamber is mostly made out of electroformed copper, improving the radiopurity and acting as the innermost part of the shielding. The Micromegas readout have been redesigned with improved solder-less connection of all the drift and field cage electrodes. All front-end electronics components, potentially radioactive, are outside the shielding. All gaskets are out of radiopure teflon.
- **Electronics:** The new detector will enjoy an electronics based on the AFTER chip [179] developed at CEA/Saclay to be used in the DAQ of the Micxromegas TPC of the T2K experiment. This electronics provides independent temporal information for every channel, adding extra topological information with respect to the previous (2D-proyected) Gassiplex-based DAQ, and potentially adding discrimination capabilities to the offline analysis. The form factor of the electronics allows for future upgrade to the AGET chip [180] currently under development. This chip offers autotrigger capabilities which translate to potentially lower threshold for this detector.

The construction of this prototype, and its operation in 2014 in CAST in conjunction with the new x-ray optics will be an important milestone for IAXO. The detector is supposed to achieve a background level that will be very close to the requirement for IAXO. Its operation will give important information to define an additional decrease of the background well below 10^{-7} counts keV^{-1} cm^{-2} s^{-1} . It is important to stress that the strategies for background reduction are not exhausted with the design here presented, and prospects for additional improvement are based on one or more of the following lines of work that will be studied in parallel:

- Improvements in gamma shielding, especially towards further reduction of the unavoidable open solid angle in the connection of the detector to the magnet.
- Improvements in active muon shielding, increasing the veto efficiency.
- Improvements in radiopurity of components of the detector chamber itself.
- Improvements of the offline discrimination algorithm, possibly using the new topological information provided by the new AFTER electronics, and the lower threshold expected from the better signal-to-noise ratio offered by the new electronics. In addition, further study of the discrimination algorithms will be possible with the dedicated multi–energy calibrations soon to be available in the x-ray tube installation of the CAST detector lab at CERN. Finally the use of different gases may bring improvement also in this direction.

4.4 General assembly, rotating platform and gas system

The proper rotation and inclination of the IAXO magnet and detectors, which have to follow the sun's trajectory, is performed by an altitude-over-azimuth mount situated on a concrete foundation. This assembly is generating the system's motion via two semi-circular objects, responsible for the systems inclination by means of hydrostatic pads and rollers, and a structural steel disk, mounted on circular rails and generating the system's rotation by means of roller drives. The primary magnet system service units, including the interfacing proximity cryogenics enforcing supercritical helium flow in the cold mass cooling pipes, the cryostat isolation vacuum system, the power convertor and auxiliary switches, current leads and the diodes-dump-resistors unit, as well as the controls and safety systems are mounted on top of the rotating table to couple their position to the rotation of the magnet cryostat, thereby simplifying the transfer lines and flexible cables arrangement. As presented in section 4.1 and shown in Fig. 4, all service lines connected to the magnet cryostat are provided through flexible transfer lines and flexible superconducting cables that are connected to a stationary services turret on the magnet cryostat. The flexibility of the transfer lines and cables is required to compensate for the changing inclination angle of the magnet. The ground stationary service units, like the cryogenics plant providing liquid helium to the system and mains switchboards, will be housed in the side building.

The movement of the Sun in the azimuth-altitude plot along the year is shown on the left of Fig. 22 for CERN geographical coordinates. Assuming all the azimuthal angles are reachable, the maximum elevation of the structure will determine the total fraction of time that the sun is reachable by IAXO. On the right of Fig. 22 the relation between maximum magnet tilting and the fraction of time of sun tracking is shown, computed for the CERN geographical coordinates. If we aim at an effective exposure of about half of the time ($\epsilon_t = 0.5$), the needed maximum elevation for IAXO's structure is $\pm 25°$. In Fig. 23 we

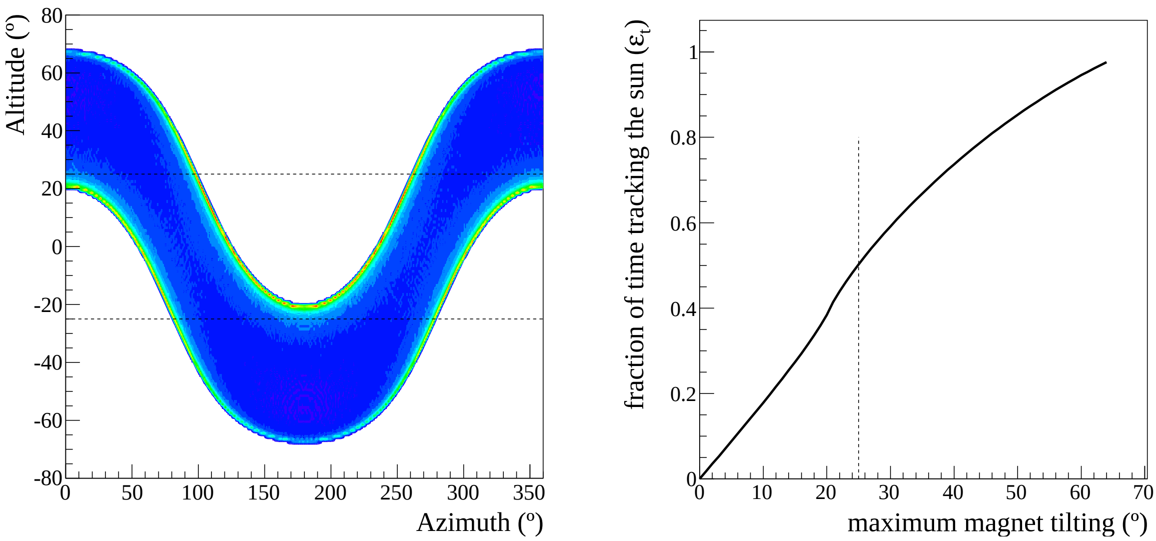

Figure 22: On the left the region of azimuth-altitude coordinates of the Sun position along one year for CERN geographical coordinates. The horizonal lines show the range of elevation for IAXO. On the right the fraction of time the Sun is reachable versus the maximum elevation. The horizontal line indicates the value of elevation that we aim for IAXO, $\pm 25°$, which corresponds to $\epsilon_t = 0.5$.

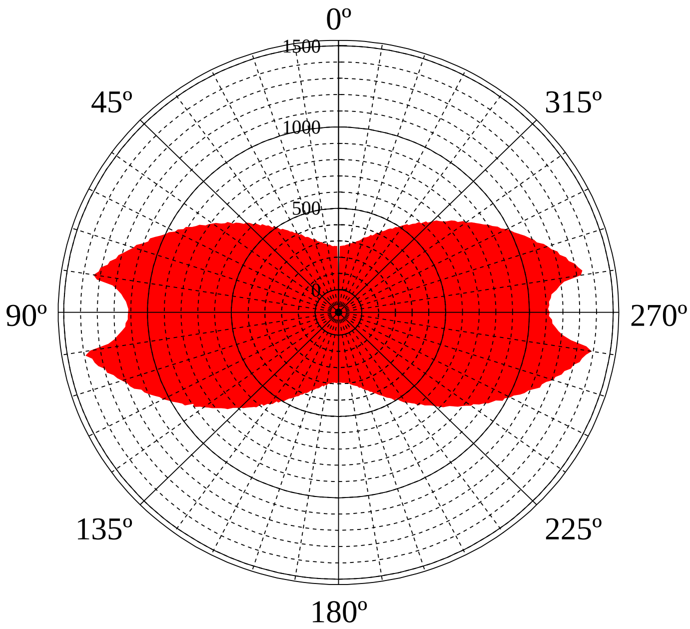

Figure 23: The distribution of exposure time in azimuthal coordinates. North direction corresponds to 0°

show, in polar coordinates, the distribution of exposure time to the Sun in azimuthal coordinates.

In addition, for Run II (see section 5) the magnet bores must be filled with gas at precise and well-controlled pressures, for which an appropriate gas system will be needed. The system will have several stages including storage, circulation, pumping, metering system and a set of monitoring probes for the gas. The experience with the gas system developed for CAST will be very valuable as conceptually the system will be similar, however, the system needed for IAXO will be substantially simpler in several aspects. For CAST the operating gas was ^{4}He and at a later stage ^{3}He (a considerably expensive gas that required very stringent safety requirements to the system). ^{3}He was needed to reach the high densities associated to the values of m_a aimed for, given that the gas was at cryogenic temperatures when inside the bore. The fact that IAXO bores are at room temperature and that the maximum axion mass aimed for is of $m_a \sim 0.25$ eV (see figure 25), makes that the IAXO gas system will use only ^{4}He, the gas will be always at room temperature and the working pressures will range from 0 to 1 bar (no need for high pressure specifications). In CAST conditions, the need to study and control the potential excursions and inhomogeneities of the gas density along the magnet bore supposed a large challenge for the monitoring, simulation and data treatment of the experiment. Although detailed studies of, e.g., the expected density gradient along the IAXO bores will be done for the Technical Design Report, the maximum densities of the gas in IAXO will always be well below the densities where we expect any substantial effect in density gradient according to the experience in CAST.

4.5 Additional equipment

The equipment described in previous sections completes the baseline of IAXO. Magnet, optics and x-ray detectors have been described to some extent and rely on solid technological ground. They are sufficient to accomplish the primary physics goal of the experiment. The additional equipment described below rely on less developed considerations but offer potential improvements beyond the baseline of the experiment. They include GridPix detectors, Transition Edge Sensors (TES), low noise Charge Coupled Devices (CCD) and microwave cavities and antennas. None of the quantified physics potential explained in section 5 relies on any of these devices. The motivations to consider an complementary or alternative use of this equipment are several:

- They offer potential to span the detection energy window of solar ALPs to lower energy ranges (GridPix, TES, CCD) which could be interesting for additional searches of more specific ALPs or WISP models (e.g., hidden photons, chamaleons or other ALPs)
- They offer potential for new physics cases, like the detection of dark matter axions and ALPs (microwave cavities or antennas).
- Even if at the moment the Micromegas detectors are the ones with best prospects to achieve the needed FOM for low background x-ray detection in IAXO, other technologies, e.g., low noise CCD, could eventually prove competitive too as R&D is ongoing in this direction. Provided similar FOMs were achieved by a second technology, the preferred configuration for IAXO would be a combination of the two (e.g. half the magnet bores equipped with one kind of detector and half with another), as this configuration is more immune to systematics effects in case of a positive detection.
- Finally, the consideration of more technologies is helpful to attract and built community around the project.

4.5.1 GridPix

The GridPix development aims at the combination of a Micromegas with a highly pixelized readout [182]. To cope with the large number of electronics channels needed to cover significant areas with very fine granularity, the readout ASICs of pixel detectors are used. The bump bond pads, which are usually used

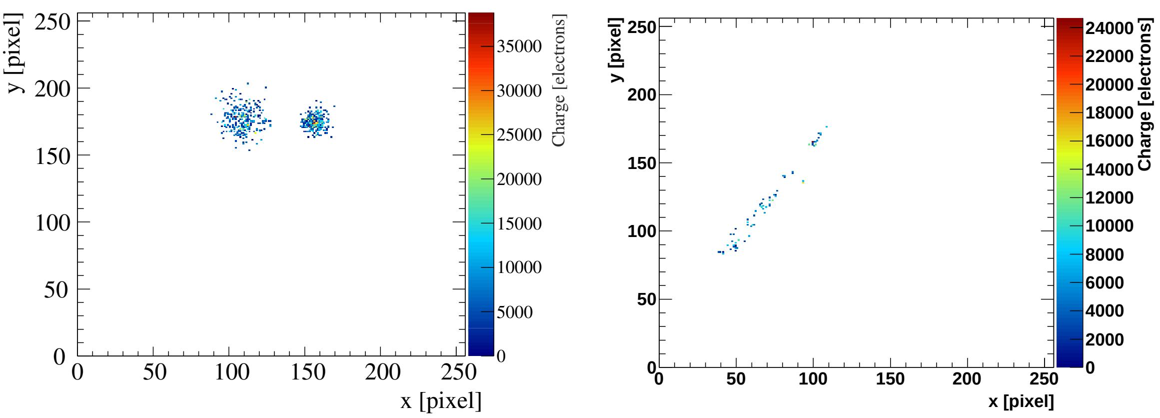

Figure 24: Left: Conversion of two X-ray photons at different drift distances, right: track of cosmic ray [181].

to connect the ASIC to the silicon sensor, are placed below the Micromegas and serve as charge collection pads. Currently the Timepix ASIC [183] is used as a readout chip, but the successor, Timepix3, is under development and will feature many improvements of the Timepix's limitations. The Micromegas gas amplification structure can be built directly on top of the ASIC. Industrial post-processing techniques ensure an optimal alignment of grid holes with the pixels, a very thin grid of less than 1 μm thickness and a very homogenous gap and hole size. The low noise level and uniform gas amplification properties of the setup result in a single electron efficiency of 100 % for moderate gas amplifications of a few thousand (the event picture with 2 photon conversions of an ^{55}Fe-source are shown on the left of Fig. 24). If sufficient diffusion is provided, the primary electrons of each photon conversion can be determined by counting the pixels hit.

This results in three features potentially very interesting for IAXO. Firstly, it should lead to improved energy resolution (see for example Ref. [184]). Secondly, when a photon is absorbed in the gas, on average one electron is created per 20-30 eV photon energy. Only a few primary electrons are sufficient to identify a photon, thus lowering, in principle, the threshold for photon detection. Currently, first measurements are under way to study the lower energy part of the detectable spectrum. Finally, the precise topological reconstruction of events helps to distinguish the photon conversions from background events such as cosmic ray tracks (the event picture with of a background track can be seen on the right of Fig. 24). With a first detector a background suppression by a factor of about 120 was reached [184]. With more sophisticated algorithms such as neural nets, and new electronic components, in particular the above-mentioned Timepix3, will lead to further improvements in all three key parameters. First tests of such a system are planned for the fall of 2013 in the CAST experiment. The development of critical detector components, such as photon windows with low material budget, will continue independently.

4.5.2 Transition edge sensors (TES) for IAXO

Transition Edge Sensors (TES) [185] offer the possibility of extending the detection energy window of IAXO to much lower energies while potentially keeping single-photon counting capability and very low background rates. TES-based photon sensors have an extremely low intrinsic dark count rate since they operate at sub-K temperatures, where the available thermal energy is not sufficient to excite a transition. The response time of TES-based sensors is in the range of the tens of microseconds, not sufficient for fast counting applications, but more than adequate in WISP searches, where expected counting rates are well below 1 Hz. Within these limitations TES-based sensors are capable of counting single photons down to the sub-eV energy range [186, 187, 188]. The energy range of maximum sensitivity for TES-based sensors depends on the thickness and type of material used for the layer which must absorb the incoming photons. It is possible to manufacture sensors with overlapping energy sensitivities from $\sim$1 eV up to several keV and cover all the energy ranges of interest of solar WISP detection: visible (hidden photons), below 1 keV (chameleons), keV range (QCD axions and other ALPs).

Challenges for TES operation at helioscopes TES-based sensors operate in a sub-K environment (typically 100 mK) which must be reached and maintained for the entire duration of the measurements. The standard way to operate a TES is to insert it into a refrigeration unit which uses cryogenic fluids or a pulse tube to bring the temperature in the K range, and then either ^{4}He-^{3}He dilution or Adiabatic Demagnetization Refrigeration(ADR) to move down to the mK regime. All these cooling solutions are commercially available. In a magnetic helioscope, such as IAXO, the first-stage cooling needs (from room down to K temperatures) could be covered by using the liquid He supply necessary for magnet operation, while the second-stage cooling technique must be chosen between dilution and ADR. The former (dilution) has the advantage of working in continuous mode once the final temperature is reached, and of being largely insensitive to stray magnetic fields, while disadvantages include the necessity of precisely manipulating expensive gases such as ^{3}He. The latter (ADR) has the advantage of ease of operation and the disadvantage of working in hour-long cycles: the cold chamber slowly heats up and the demagnetization procedure must be repeated. In addition, since the SQUID circuits necessary for TES readout are sensitive to the stray magnetic fields generated by the ADR, shielding and compensation coils must be accurately designed.

The main drawback for the use of TES-based sensors in a helioscope is the small sensitive area: typical sensors have sensitive areas of (100 μm)$\times$(100 μm) up to (1 mm)$\times$(1mm). This limitation can be partially overcome by combining single sensors into an array connected in parallel [189, 190]. Such arrays could reach sensitive areas of about 1 cm^2. An additional possibility is to position the TES-based sensor in the focal point of an x-ray optics. The focal point area considered for IAXO optics are $\sim$0.2 cm^2. The reflectivity of the optics to the appropriate photon wavelengths should be taken into account. A further challenge is coupling the TES-based sensor to the helioscope beam. In the case of $\sim$1eV photons this can accomplished by means of an optical fiber conveying photons from the helioscope to the sensor itself which can, in principle, be positioned far away from the magnet and within its own refrigeration unit. With photons of energies above $\sim$10 eV, the TES-based sensor must be placed directly in the beam.

Proposed detector The basic characteristics of TES-based sensors are ideally suited for WISP searches, while the small sensitive area presents a challenge when proposing the application of these sensors to helioscopes such as IAXO. One option to turn this weakness into a strength is to combine several TES sensors sensitive to different energy ranges into a single chip to be positioned in the focal point of an x-ray optics. Such a Multy-Energy TES Array (META) could be for example one of the basic detectors to be used in IAXO runs. Possible construction steps for META:

- Design and manufacture a single chip with TES sensors having different absorber thicknesses/materials in order to cover photon energies from 1 eV up to several keV. Each sensor must have its own current readout channel, keeping however the option of connecting them all in parallel. Target size for individual sensor sensitive area should be (1 mm)$\times$(1 mm).
- Test multi-energy TES arrays in a stand-alone refrigerator (requires finding appropriate photon sources)
- Design and manufacture cold finger assembly to hold the META sensor in the beamline after choosing a final-cooling stage method (either dilution or ADR)

Sensor pads differing only in thickness can be integrated on a single chip with readily available technology and equipment. For pads relying on different layer material acting as absorbers, some technical developments are necessary. Furthermore, TES pads having layers made of the same materials will work at the same transition temperature, while for pads made of different materials the question must be investigated through simulations and actual tests. There is also the possibility to individually tune the electro-thermal feedback biasing each pad to compensate for differences in transition temperature and response, this must however be thoroughly checked experimentally. Finally, the technology to achieve a sensitive area of 1 mm^2 area for each sensor pad is presently available, however this development will require a significant increase in financial and personnel resources with respect to the present situation.

In practice, the possible short term developments are to design and manufacture a prototype META chip and to conduct laboratory tests with visible and soft X-ray sources. With readily available equipment, a prototype META could be manufactured with 2 or more (20 μm)$\times$(20 μm) TES pads made of the same material, but having different thicknesses in order to cover photon energies up to 1 keV.

It should be noted that the ALPS-II experiment at DESY in Hamburg plans to use a TES for WISP searches and future space-born X-ray missions are developing TES arrays as detector options. The BaRBE collaboration in Italy (INFN Trieste, University of Camerino, INRiM Torino) is presently testing TES-based detectors sensitive in the visible range and is developing coupling methods with source photons using optical fibers. The intended application is WISP searches, including CAST and IAXO. Hence, some experience exists in the application of TES systems in the fields relevant for IAXO.

4.5.3 Low-noise Charge Coupled Devices (CCDs) for IAXO

Charge coupled devices (CCDs) are routinely used for detection of soft x-rays or photons with near-visible wavelengths, in applications like photography or astronomical imaging. These devices have been developed in part to make use of their small pixelated structures which allow for high resolution image reconstruction. In this standard application, noise is often not a problem as the integration time (exposure time) is relatively short and thus there is low noise even with fast readout. Image processing algorithms can be employed to clean up residual artifacts from noise. As a static detector integrating energy deposited by photons or other particles, CCDs have a noise component that arises from internal dark currents and the accumulation of charge deposited by the clocking signals used to move charge to readout amplifiers within the CCD. Such noise makes CCDs less than ideal in the search for signals from new particles as the differentiation between charge from noise and charge from possible new physics is difficult to distinguish.

R&D on techniques to minimize this noise have been carried out with CCDs used for the Dark Energy Survey (DES) astronomical survey. These CCDs, in order to be more sensitive to near infra-red photons, are hundreds of microns thick compared with more traditional astronomical CCDs. An interesting by-product application found for these more massive CCD sensors is to use them as the sensitive element in the search for low-mass WIMP Dark Matter recoils. The DArk Matter In CCDs (DAMIC) [191] experiment is using CCDs in the search for low-mass WIMPs where low noise is necessary in order to gain sensitivity for their interactions in the bulk of the silicon.

There are plans to study the possibility of using this type of low noise CCDs in IAXO. This could be either as alternative keV x-ray detector, provided the ongoing low noise R&D succeeds in getting a competitive figure of merit, or as a detector for softer x-rays, in order to expand the IAXO energy window to lower values, as needed for a number of additional potential physics goals of IAXO (see section 5.3). CCDs have been used as detectors for soft x-rays and thus there is nothing intrinsic in preventing the DES CCDs being used in a solar helioscope although the quantum efficiency versus x-ray wavelength would need to be quantified. Soft x-rays also do not penetrate much material and a suitable window or other system would be required to ensure that x-rays produced in the helioscope would impinge upon the sensor. As long as these technical difficulties are addressed, there could be a real advantage to using low noise CCDs in a helioscope to search for the new particles in a manner that would complement more conventional approaches to x-ray detection.

4.5.4 Microwave cavities and/or antennas

Still at an early stage of development, the possibility of using the large magnetic volume of IAXO to search for relic axions or ALPs is very appealing. The physics potential of this possibility is discussed briefly in section 5.5. These searches require microwave cavities or –as recently proposed– antennas, coupled with appropriate low noise sensors, all embedded in strong magnetic fields.The sizes, design and features of these elements will depend very much on how this concept is further developed. The fact that the IAXO magnet is built with very easy access to the magnet bores make the option to instrument one or more of these bores with cavities or antennas feasible. This could be conceived as an additional data taking phase or in parallel with the solar axion searches. Technically more difficult, but also conceivable, would be to instrument the unused empty magnetic space inside the magnet cryostat for this purpose.

5 IAXO physics potential

In this section we review the physics potential of IAXO. We evaluate with some detail the expected sensitivity to solar axions and ALPs emitted via generic Primakoff effect. This is the main physics outcome of the experiment. We also estimate the sensitivity of IAXO to non-hadronic solar axions emitted by BCA processes. Although secondary, this goal shows high potential, with sensitivity to meV-scale axion models. Finally, we briefly mention additional potential goals of IAXO, without showing quantitative results.

5.1 Expected sensitivity to solar axions and ALPs

The main experimental parameters entering the figure of merit defined in section 3.3 are listed in table 3. Two set of values are indicated, one conforming the "nominal scenario", and the other the "enhanced scenario". Both set of values approximately represent our current estimation of the range encompassing the final performance expected for the different subsystems of IAXO, as justified by the considerations exposed in section 4.

This breakdown of the figure of merit allows to approximately quantify the improvements expected from each of IAXO subsystems. Already this simple exercise points to sensitivities, in terms of detectable signal counts, up to $\sim 10^{4-5}$ better than the CAST vacuum result, which corresponds to more than one order of magnitude in $g_{a\gamma}$.

Parameter	Units	CAST-I	IAXO Nominal	IAXO Enhanced
B	T	9	2.5	2.5
L	m	9.26	20	20
A	m^2	2×0.0015	2.3	2.3
f^*_M		1	300	300
b	$\frac{10^{-5}\,\mathrm{c}}{\mathrm{keV\,cm^2\,s}}$	~ 4	5×10^{-3}	10^{-3}
ϵ_d		0.5 – 0.9	0.7	0.8
ϵ_o		0.3	0.5	0.7
a	cm^2	0.15	8×0.2	8×0.15
f^*_{DO}		1	17	60
ϵ_t		0.12	0.5	0.5
t	year	~ 1	3	3
f^*_T		1	3.5	3.5
f^*		1	2×10^4	6×10^4

Table 3: Values of the relevant experimental parameters representative of IAXO, both the *nominal* and *enhanced* ones, based on the considerations explained in section 4. They are compared to the ones representing the CAST vacuum phase result (CAST-I) [59]. Numbers shown for the figures of merit (equation 11) are relative to CAST-I, i. e. $f^* = f/f_{\mathrm{CAST}}$, and are approximate.

Run:	Run I	Run II
Total duration:	~ 4 years	~ 4 years
Effective data taking duration:	3 years	3 years
Effective exposure:	9540 h	9540 h
Gas density: (^{4}He at room temperature)	0 bar	variable from 0 to ~ 1 bar
(in terms of axion mass)	0 eV	0–0.25 eV

Table 4: Values of the exposure used to compute the sensitivity curves.

In order to add fidelity to our estimates, we have fully computed sensitivity values from both nominal and enhanced scenarios, by means of a Monte Carlo simulation of the expected background counts in the optics spot area, computation of the likelihood function and subsequent derivation of the 95% upper limit on the $g_{a\gamma}$ assuming no detected signal. The calculation is repeated for a range of m_a values in order to build full sensitivity lines in the $(g_{a\gamma}, m_a)-$plane.

Regarding exposure, we have assumed the two runs shown in table 4. IAXO Run-I will be performed with vacuum in the magnet bores and 3 years of effective data taking (four years total duration for a 75% assumed duty cycle), and will determine the sensitivity of IAXO for axion masses below $m_a \lesssim 0.01$ eV. IAXO Run-II will use a buffer gas inside the magnet bores in order to recover coherence above $m_a \gtrsim 0.01$ eV. The range of densities used (number of gas density steps) will determine how far in m_a to go. The current sensitivity curves are calculated assuming that the gas density in Run II is continuously changed from 0 to 1 bar of ^{4}He at room temperature, during a total effective data taking time of 3 additional years. This program would allow IAXO to reach an axion mass of 0.25 eV. The shape of the sensitivity region in the range m_a ~0.01−0.25 eV depends on the actual distribution of the exposure time in density, which is for now assumed flat, i.e. we spend equal time at each gas density. This distribution may be redefined in the future according to the evolution of bounds on the axion mass or other eventual results/interest favoring a particular m_a value or range.

In Fig. 25 the area to be explored by IAXO is shown. The obtained values for each of the scenarios are represented by the couple of lines bounding the dashed area. As seen, IAXO will be a factor of $\sim 15-20$ more sensitive than CAST in terms of the axion-photon coupling constant $g_{a\gamma}$, which translates in about **5 orders of magnitude more sensitive** in terms of signal intensity. That is, IAXO could be sensitive to $g_{a\gamma}$ values as low as, or even surpassing,

$$g_{a\gamma} \sim 5 \times 10^{-12}\ \mathrm{GeV}^{-1} \tag{20}$$

for a wide range of axion masses up to about 0.01 eV and around $g_{a\gamma}$ ~10^{-11} GeV^{-1} up to about 0.25 eV.

While CAST was the first experimental search reaching, and slightly surpassing, the limit $g_{a\gamma} \lesssim 10^{-10}$ GeV $^{-1}$ in this mass range, and therefore started probing ALP parameter space allowed by astrophysics, IAXO will deeply enter into completely unexplored ALP and axion parameter space, as indicated by Fig. 25. At a minimum, IAXO will exclude a large region of the QCD axion phase space that has yet to be explored. If IAXO does discover a new pseudoscalar fundamental, it would be a groundbreaking result for particle physics.

Fig. 26 focuses on the sensitivity for the high mass region $m_a > 1$ meV. At these masses this experiment would explore a broad range of realistic axion models that accompany the Peccei-Quinn solution of the strong CP problem. Its sensitivity would cover axion models with masses down to the few meV range, superseding the SN 1987A energy loss limits on the axion mass. Axion models in this region are

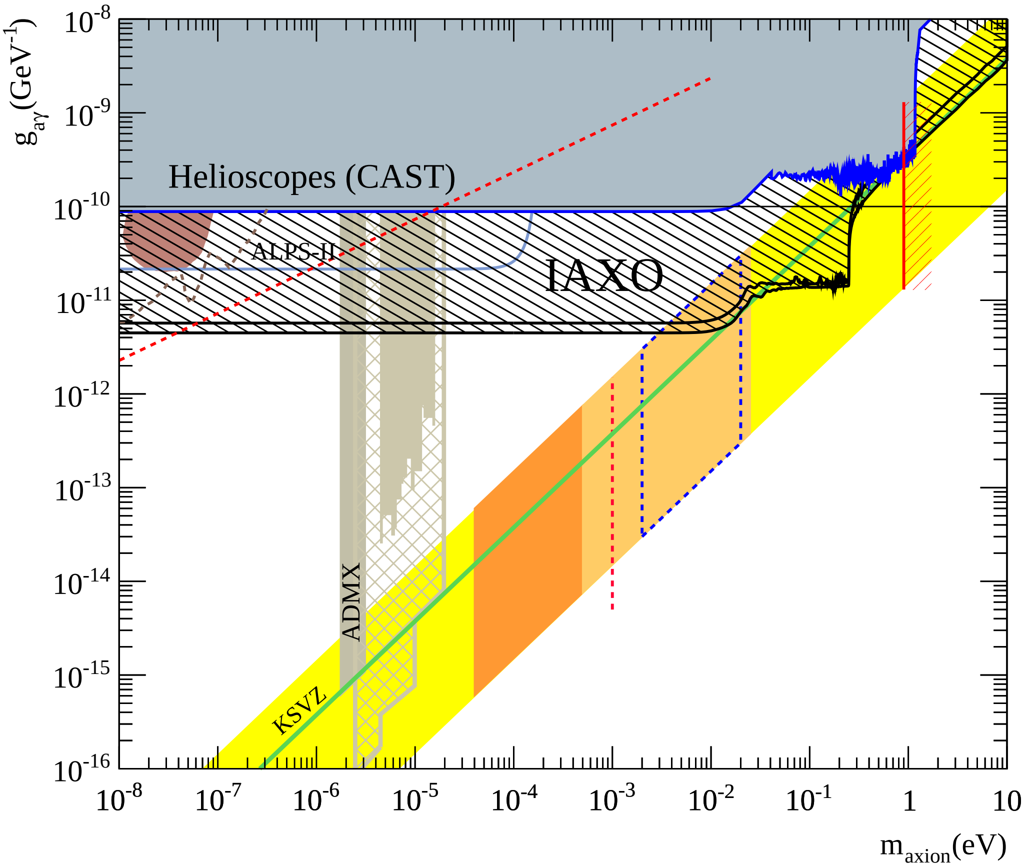

Figure 25: Expected sensitivity of IAXO as explained in the text, compared with current bounds from CAST and ADMX. Also future prospects of ADMX (dashed brown region) and ALPS-II [192] (light blue line) are shown. For the sake of clarity we have removed labels from other bounds or regions. We refer to figure 1 for those.

of high cosmological interest. As explained in previous sections, they are favored dark matter candidates and could compose all or part of the cold dark matter of the Universe. In non-standard cosmological scenarios, or in more generic ALP frameworks [46], the range of ALP parameters of interest as DM is enlarged and most of the region at reach by IAXO contains possible dark matter candidates. At the higher part of the range (0.1 - 1 eV) axions are good candidates to the hot DM or additional *dark radiation* that is recently invoked to solve tension in cosmological parameters. At much lower masses, below $\sim 10^{-7}$ eV, the region attainable by IAXO includes ALP parameters invoked repeatedly to explain anomalies in light propagation over astronomical distances. IAXO could provide a definitive test of this hypothesis.

5.2 Axion-electron coupling

Axions with an axion-electron coupling $g_{ae} \sim \mathcal{O}(10^{-13})$ have been invoked to solve the anomalous cooling observed in white dwarfs as was explained in section 2.4 and could affect the dynamics of further stars: neutron star cooling, SN explosions, etc. IAXO is sensitive to non-hadronic axions with a

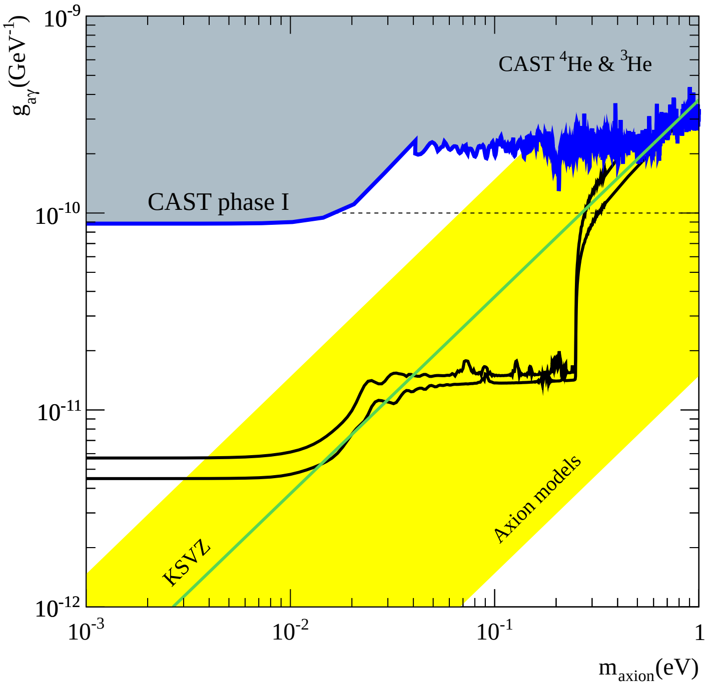

Figure 26: Close-up of the high mass part of parameter space of Fig. 25 (1 meV $< m_a <$ 1 eV).

sizeable coupling g_{ae} because it can detect the flux of solar axions originating from axion-Bremsstrahlung (electron-ion and electron-electron) Compton, and, to a lesser extent, axio-deexcitation of ions (together referred to BCA reactions).

As seen in figure 2, for this kind of models, the flux of solar axion produced via BCA processes may be up to 10^2 times larger than the standard Primakoff axions, providing a relevant opportunity to be searched for at helioscopes [134]. The energies of these axions are somehow lower than the Primakoff ones, falling in the range of about 0.5-2 keV. Provided the threshold of the IAXO optics and detectors is low enough, something that it is technically feasible if taking into account at design time, competitive sensitivity to these models can be reached.

In this case the expected signal depends on $g_{ae}g_{a\gamma}$, the product of the electron coupling (responsible for the production in the Sun) and the two-photon coupling (responsible for the detection in IAXO). The plot on the left of fig. 27 shows the computed sensitivity of IAXO to the product $g_{ae}g_{a\gamma}$ assuming that the Primakoff emission from the Sun is subdominant and therefore the solar flux is caused by the BCA reactions alone. The computation is performed in a similar way and with the same assumed parameters than in previous section. The additional input is that energy threshold for both detectors and optics is set at 0.5 keV, with background and efficiencies comparable to the ones in previous section down to this threshold. Under the assumption of no positive signal, IAXO could be able to constrain

$$g_{a\gamma}g_{ae} < 2.5 \times 10^{-25}\,\mathrm{GeV}^{-1} \quad (95\%\ \mathrm{CL}) \tag{21}$$

at low masses $m_a \lesssim 10$ meV — where the probability of axion-photon conversion in IAXO becomes independent of the mass — and worsens as $1/m_a^2$ for higher masses. In general, IAXO would be sensitive to the region above the black lines (nominal and enhanced IAXO scenarios) in plot on the left of Fig. 27.

The orange band in that plot represents axion models with g_{ae} values suggested by the anomalous WD cooling, and with $g_{a\gamma}$ given by the DSFZ model. The part of the band highlighted in yellow could satisfy also the model-dependent relation of g_{ae} and m_a. Values above that band are firmly excluded. As seen, IAXO could reach a sensitivity more than two orders of magnitude better than the recent similar analysis performed with CAST data [134] (shown in the same plot) and enough to reach the relevant models at the right mass values ($m_a \gtrsim 3$ meV).

If we also include the Primakoff flux (which is unavoidable because it is produced by the same coupling $g_{a\gamma}$ involved in the detection), the signal at IAXO depends on three parameters: g_{ae}, $g_{a\gamma}$ and m_a. However, for $m_a \lesssim 10$ meV the detection is independent of m_a and we can plot our results in the g_{ae}–$g_{a\gamma}$ parameter space. In this low-mass range, Run-I gives the highest sensitivity and thus we have focused only on this data set. The black lines in the plot on the right of Fig. 27 show the region that IAXO would be sensitive to, compared to that excluded by CAST. For very small values of $g_{ae} \lesssim 10^{-12}$, the BCA flux is negligible and the IAXO line smoothly becomes the standard one of previous section where only Primakoff emission was assumed. However, for larger values of g_{ae} the BCA flux becomes dominant and we recover the bound of Eq. 21.

We also show in the plot on the right of Fig. 27 an orange band representing parameters where axion

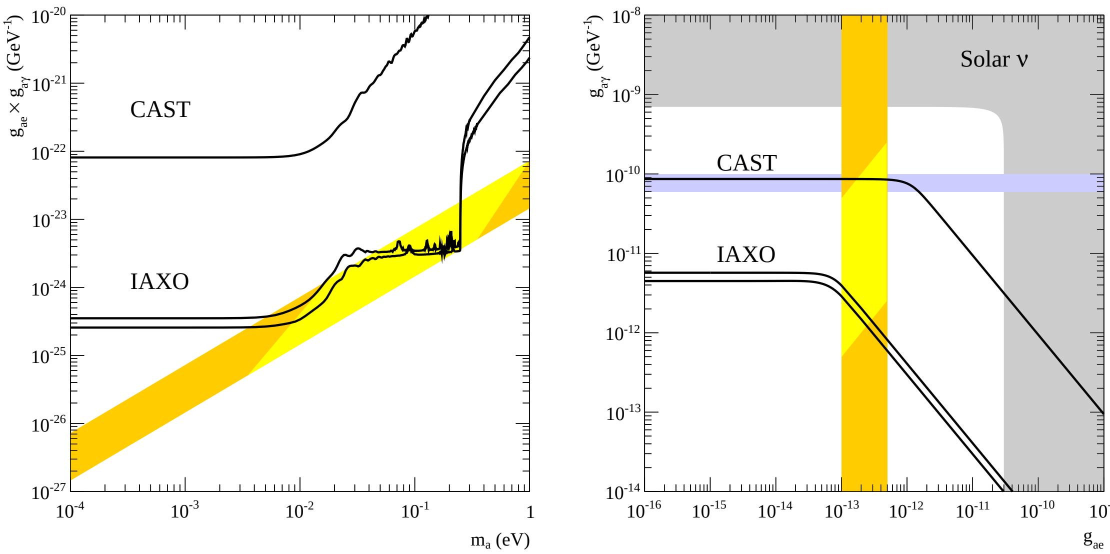

Figure 27: Left: IAXO sensitivity line for $g_{ae}g_{a\gamma}$ as a function of m_a, assuming the solar emission is dominated by the BCA reactions which involve only the electron coupling g_{ae}. The orange band corresponds to values of $g_{ae} \sim 1-5\times10^{-13}$ and $g_{a\gamma}$ related to m_a by the DSFZ model with $C_\gamma = 0.75$. The part of the band highlighted in yellow corresponds to those models for which the relation of g_{ae} with m_a is also considered (taking a reasonable range $\cos^2\beta$ =0.01−1). The recent limit of CAST on g_{ae} is also shown. Right: IAXO sensitivity on g_{ae} and $g_{a\gamma}$ for $m_a \lesssim 10$ meV. The gray region is excluded by solar neutrino measurements. The orange band corresponds to values of $g_{ae} \sim 1-5\times10^{-13}$. The part of the band highlighted in yellow corresponds to models that satisfy the model-dependent relation between $g_{a\gamma}$ and g_{ae} (taking again $C_\gamma = 0.75$ and $\cos^2\beta$ =0.01−1). The recent limit of CAST on g_{ae} is also shown. In the orange bands, axion emission affects white dwarf cooling and the evolution of low-mass red giants; couplings stronger than in these bands are firmly excluded. Likewise, helium-burning stars would be perceptibly affected in the blue band of the right plot and parameters above it are excluded.

emission would have a sizeable impact on stellar evolution. In the vertical orange band of g_{ae} values, axion emission would perceptibly affect WD cooling [193, 194, 92, 93, 23, 24, 195, 196] and delay helium ignition in low-mass red giants [197, 198]. Parameters to the right of this band are excluded and to the left are harmless. The part of the band highlighted in yellow includes the models for which $g_{a\gamma}$ and g_{ae} fulfill a model-dependent relation (see figure caption). Within the horizontal blue band, axion Primakoff emission would affect stars in the helium-burning phase. The upper edge of this band corresponds to the traditional horizontal-branch star limit and the remaining to the the suppression of the blue-loop of massive stars [21], see the summary of constraints in section 2.

In summary, IAXO could directly measure the solar flux of axions produced by the BCA processes, for the first time with sensitivity to values of g_{ae} not previously excluded and relevant to test the hypothesis that the cooling of WD is enhanced by axion emission (via BCA procesees, the same mechanisms that IAXO would be testing in the Sun), and for values of m_a for which QCD axion models can give the needed g_{ae} values.

5.3 Additional physics potential

IAXO can be sensitive to models of other proposed particles at the low energy frontier of particle physics. Some examples, briefly mentioned in section 2.3, are hidden photons or chameleons. They could also be produced in the Sun, and give specific signatures in axion helioscope data. Hidden photons emitted from the Sun have been studied in the context of specific searches [127] or as by-products of axion helioscopes like Sumico [128] or CAST [199]. Chameleons are scalars with an environment-dependent mass that are proposed in the context of dark energy models. Recent calculations [200, 192] show that resonant production in the magnetic regions of the solar atmosphere might allow for the propagation of these chameleons into a solar helioscope where they can be regenerated into soft x-rays through the inverse Primakoff-effect. For these searches, sensitivity to energies lower than the baseline Primakoff axion spectrum (sub-keV and lower) is needed, something that IAXO could obtain by one or more of the additional equipment described in section 4.5.

More intriguing would be the possibility to detect relativistic axions or ALPs from other sources in the sky, using IAXO as a true axion telescope. Although most potential astrophysical axion sources will probably be too faint to be detected by IAXO, some relic populations of ALPs could provide detectable signals. If the dark radiation that is recently invoked to relieve the tension in cosmological parameters [29] is composed by relativistic axions or ALPs (from, e.g., primordial decays of heavy fields [201]) they would still linger today as a Cosmic Axion Background with energies of $\sim \mathcal{O}(100)$ eV. With appropriate low energy detectors, the predicted fluxes could be within reach of IAXO for some ALP parameters. The relevance of such search is briefly discussed in the following section.

Finally, IAXO could also search for the non-relativistic axions potentially composing the galactic dark matter halo. This could be accomplished by using microwave cavities (and turning IAXO into a haloscope kind of detector), or dish antennas [102, 202] inside the large IAXO magnetic volume. The size and strength of the IAXO magnet make this possibility very appealing and deserves serious consideration. Still a possibility under study, it is discussed in some detail in section 5.5.

Another experimental configuration of IAXO could be to equip two of the bores with microwave cavities, one of them with a strong emitter, and the second one with a low-noise receiver. This would be an analogous LSW experiment with microwaves, conceptually similar to the one performed in [203]. Given the size of the IAXO magnet bores, the operating frequency of such a configuration would be around 200 Mhz. The potential of this configuration is currently under study.

5.4 Search for axionic dark radiation in IAXO

Axions and ALPs appear copiously in string theories, see e.g. [50]. String compactifications imply a plethora of new particles but very often most of them are very weakly interacting and very massive (e.g. moduli) and thus are very difficult to test experimentally. Axions are naturally very light and thus constitute prime tests of a number of these theories [51, 52]. Recently, it has been pointed out that the decay of moduli in the early universe can produce a sizable amount of dark radiation (i.e. a cosmological relic of relativistic particles, with very weak interactions with the standard model) in the form of axions or axion-like particles [204, 205, 201, 206]. These dark radiation axions/ALPs can feature a coupling to photons and can thus be observed by IAXO as a diffuse isotropic background. Other observational possibilities have been discussed in [207, 206]. The shape of the energy spectrum is given by the mass of the decaying modulus (m_Φ) and the normalization by the branching ratio of the moduli into axions (B_a). For obtaining the sensitivity of IAXO we parameterize the flux as

$$\frac{d\Phi}{dE} = 2\times 10^6 \times \Delta N_{\rm eff} \times \frac{E}{E_*^3} e^{-(E/E_*)^2} \left[\frac{1}{\mathrm{cm}^2\,\mathrm{s}\,\mathrm{keV}}\right], \tag{22}$$

where E_* is the average DR axion energy *in keV* and the energy density of dark radiation, $\rho_{\rm DR}$ is parameterized through $\Delta N_{\rm eff}$, defined as $\rho_{\rm DR} = \frac{7}{8}\left(\frac{4}{11}\right)^{4/3} \rho_{\rm CMB} \times \Delta N_{\rm eff}$ where $\rho_{\rm CMB}$ is the energy density of the Cosmic Microwave Background (CMB). Note that the spectral shape is not accurate but this is not very important for our purposes. In terms of the modulus properties $\Delta N_{\rm eff} = 14\frac{B_a}{1-B_a}/g_*^{1/3}$, with g_* the number of standard degrees of freedom reheated by the modulus decay (typically $g_* \sim \mathcal{O}(60)$), and $E_* \sim 0.7\,\mathrm{keV}\left(10^6\mathrm{GeV}/m_\Phi\right)^{1/2} g_*^{-1/12}(1-B_a)^{-1/4}$.

Under the assumption that negligible background is achievable down to a threshold of 0.2 keV the sensitivity of IAXO to DR axions/ALPS would be the one shown in Fig. 28 as a function of the average energy E_*. More realistic prospects depend on the experimental parameters (background and threshold) actually achieved with the technologies of choice to extend IAXO energy window to lower values, and will be studied in the near future.

5.5 Search for relic CDM axions in IAXO

Axions and axion-like particles are excellent candidates for the dark matter (DM) of the universe. QCD axions can account for the full amount of DM observed for different mass ranges $m_a \lesssim 1$ meV. This depends whether inflation happened after (CDM-2 and 3 in Fig. 1) or before (CDM-1) the PQ phase transition and in the last case also on the initial misalignment angle. For ALPs, the ranges are much wider, because their coupling strengths and masses are unrelated [46]. The motivation of axions and ALPs as CDM candidates was exposed in detail in section 2.2

Axion and ALP DM particles convert into photons of the same energy in homogeneous magnetic fields by the inverse-Primakoff process. The huge magnet required by IAXO offer excellent possibilities to host DM searches. These come in two flavors: haloscopes and dish antennas.

The haloscope technique consists in a tunable microwave-cavity (in a strong B-field) coupled to a ultra-low-noise microwave sensor. DM axions and ALPs convert into microwaves with a boosted probability if a resonant frequency of the cavity matches the axion energy ($E = m_a + K$ with $K \sim O(10^{-6} m_a)$). In case of a discovery the measured photon energy reveals the axion mass and velocity distribution of the DM flow. Since m_a is *not known a-priori*, the experiment has to smoothly *scan* axion masses by tuning the cavity resonances until a signal is found. The power output of the cavity due to

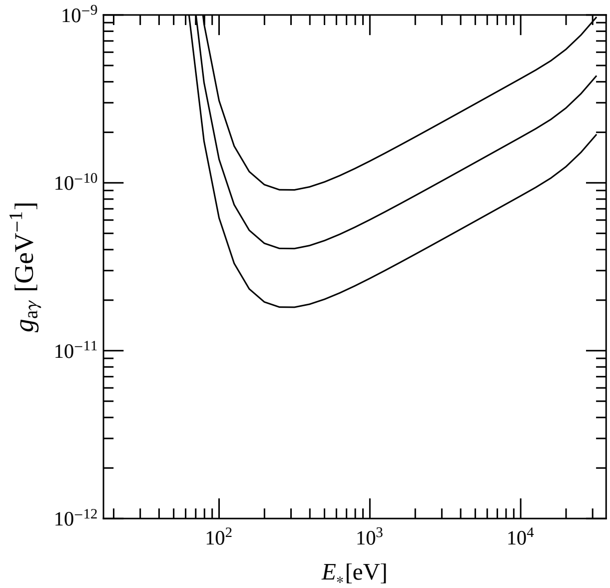

Figure 28: IAXO sensitivity to the axion/ALP two-photon coupling of cosmological dark radiation (DR). Lines correspond to 1 event/year for $\Delta N_{\rm eff} = 0.1, 0.5$ from top to bottom.

axion/ALP DM is

$$P_{out} \simeq \frac{g_{a\gamma}^2}{m_a} \times \rho_{\rm DM} \times VB^2 Q \mathcal{G}_c \kappa \tag{23}$$

where $\rho_{\rm DM}$ is the local energy density of DM, V is the cavity volume, B the magnetic field strength, Q the quality factor, $\mathcal{G}$ the overlap integral of the spatial DM and cavity modes and κ is the cavity coupling. For a cylindrical cavity with height/radius ratio $H/R = \beta > 1$, $Q = 10^6$, the fundamental mode tuned to the axion mass and $B = 5$ T,

$$P_{out} \sim 0.7 \times 10^{-22} \beta C_\gamma^2 \left(2\,\mu{\rm eV}/m_a\right)^2 {\rm W}. \tag{24}$$

The only active haloscope, ADMX, has already scanned the range $m_a \sim 2-3\,\mu$eV ($480-860$ MHz) excluding

$$C_\gamma \times \sqrt{\frac{\rho_{\rm DM}}{0.3\,{\rm GeV/cm^3}}} \gtrsim 2 \tag{25}$$

and plans to cover up to $10\,\mu$eV (2.4 GHz) with greater sensitivity, and possibly to $20\,\mu$eV (4.8 GHz) by exploiting new techniques (see Fig. 25). However, even the most ambitious ADMX plans leave a huge region of axion masses unexplored making axion and ALP DM search with IAXO very worthwhile. The ADMX cavity has $H = 1$ m, $R = 0.21$ m, which make the lowest usable resonant frequency $\omega_{\rm TEM_{010}} \sim 2\,\mu$eV.

The huge magnetic volume of IAXO would allow to host cavities much larger than ADMX, allowing to explore $m_a < 2\,\mu$eV. In this mass region, the signal to noise ratio is quite favorable. A shot noise limited detector has noise power

$$P_n \sim m_a^2/10^6 \sim 10^{-21}(m_a/2\mu{\rm eV})^2{\rm W}, \tag{26}$$

in a bandwidth $m_a/10^6$ around m_a so that each step in the mass scan would be limited by the time to tune the cavity, not by the measurement time required to observe a signal. In this *large cavity* option there are several possibilities for the geometry and the disposition inside the IAXO toroid being the most obvious a cylinder along the IAXO tubes and a toroid following the magnetic field lines. The first option requires using modes different to those of ADMX since the magnetic field lines have to be aligned with the electric field in the cavity to have $\mathcal{G}_c \sim 1$ cf., e.g. [100], also the first option does not exploit IAXO's full magnetic volume. The second option allows accessing the lowest m_a but presents more technical challenges to tune the frequencies. This is technically feasible and will be studied for the TDR. Work to estimate the reasonable mass ranges is in progress but it already appears that axions in the $0.5 - 2\mu$eV range could be either found or strongly excluded. These *large cavity* searches use a sizable part of the IAXO volume and if taken to the extreme might be incompatible with simultaneous solar axion runs, which also require IAXO to track the Sun (with possible complications for noise reduction). The possibility of performing them before or after the solar-axion runs has to taken into serious consideration.

When exploring masses similar or higher than ADMX the main problem is that the signal to noise decreases very steeply with m_a, therefore the detector's noise becomes extremely crucial and reaching the shot noise limit almost a necessity. Larger integration times are required in general and the total scanning time soon becomes dominated by measurement time. Several additional ideas exist to enhance the signal slightly. A partial boost can be also achieved by using long cavities with $\beta \gg 1$ and connecting identical cavities in parallel. We are also exploring the simultaneous detection of higher modes. These searches could be performed even during the operation of IAXO in solar-axion mode by hosting the cavities in the dead volume. All in all, it appears that IAXO can be competitive with ADMX and its upgrades and explore a complementary mass range.

A new concept for axion DM detection consists on a spherical reflecting dish (embedded in a magnetic field) that reacts to DM axion particles emitting radiation focused on its center (where the detector lies) [102]. This technique does not require tuning of the experiment to the unknown m_a. The accesible axion mass range is in practice determined by the detector sensitivity. The power received in the detector due to axion DM is

$$P_{out} \simeq \frac{g_{a\gamma}^2}{m_a^2} \times \rho_{\rm DM} \times AB^2 \mathcal{G}_d \sim 0.5 \times 10^{-27} C_\gamma^2 \, {\rm W} \tag{27}$$

where A is the area of the dish and $\mathcal{G}_d$ a geometrical factor ~ 1. For the last estimate we have taken $B = 5$ T, $A = 1$ m^2. The dish search does not rely on resonant enhancement available for a cavity search but this is compensated if a large area for the dish is available. This technique compares favorably to the resonant cavity for $m_a \gtrsim$ meV, but for these large values both techniques are not sensitive enough to reach the QCD axion. This technique is still very interesting for ALP scenarios or "axion clumps" expected in certain cosmological scenarios. Dark matter experiments in IAXO would benefit of ultra-low temperatures to reduced the backgrounds as much as possible. This suggests hosting the experiments in the cold part of the magnet. A possibility to consider is designing one of the IAXO bores to remain at liquid-He temperature to benefit directly from the cryogenics.

As laid out in [46], also hidden sector photons could constitute Dark Matter, such that a cavity hosted in IAXO could also perform particle searches when the magnet is switched off for some reason, but the cavities/ dish detectors can run. Overall, the axion DM search constitutes a very promising add-on to the helioscope physics and could contribute to solving a long-standing puzzle in (astro-)particle physics.

6 Timetable, cost estimation and collaboration

6.1 Timetable

An approximate six years time-table towards the construction and commissioning of IAXO is shown in Fig. 29. It consist of parallel timelines for the magnet, optics and detectors and include, during its first 18 months a preparatory phase with demonstrative activities in both magnet and detector plus optics, followed by the actual construction, integration, calibration and commissioning of IAXO.

Although the conceptual design of the toroidal magnet is relying on known engineering solutions and manufacturing techniques, a supplementary manufacturing design and preparation phase of about 18 months is needed to further optimize the magnet system and maximize its envisaged performance.

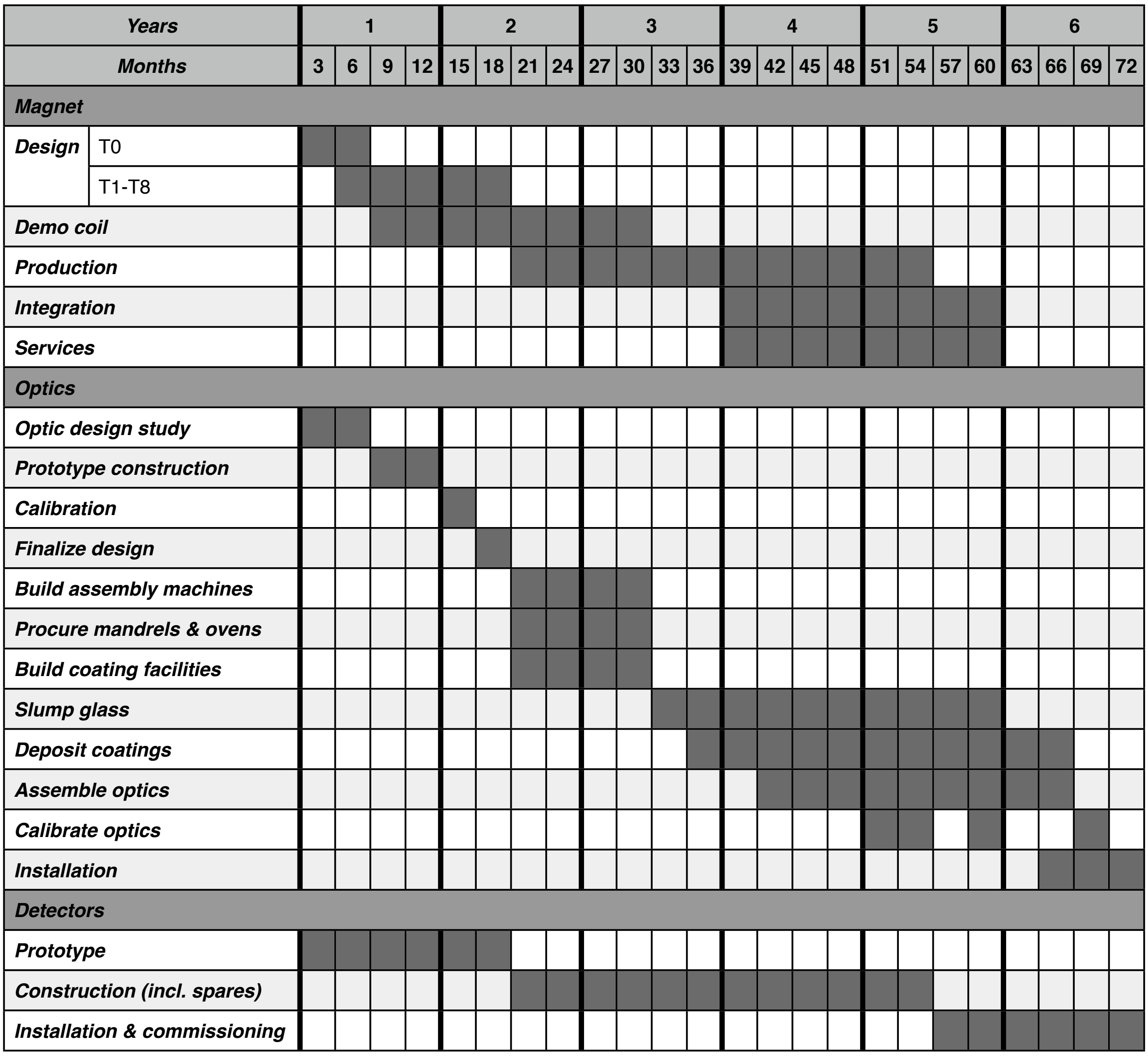

Figure 29: Timetable for the design, prototyping, construction, integration and commissioning of IAXO.

During this phase a demonstration coil (referred to as T0), 3 m long and 1 m wide, will be constructed as well. During the prototyping stage, the T0 demo coil will be used to test the magnetic behavior and quench performance of the coils. During approximately this time also prototyping activities are contemplated for the detector and the optics. A prototype optic with similar dimensions than the IAXO optics will be constructed to finetune the equipment and parameters needed to construct the final IAXO optics. This phase is understood as the last part of the design study phase of IAXO that also continues some activities that have already started, like the pathfinder system of detector and small-scale optics that is being constructed and that was described in section 4.3.3.

After about month $\sim$18 the actual production stage starts. The final eight toroidal coils (named T1 - T8) are then produced, as well as the structural parts of the magnet. The construction of the assembly machines and coating facilities for the optics takes place, followed by the actual constructions of nine (eigth plus one spare) IAXO optics. Finally, during the last 24 months of this schedule, and partially overlapping with the previous stage, the system integration takes place. The services installation for cryogenics, vacuum, power circuit and controls will take part in parallel to the system integration phase. Subsequently, the optics and detectors are installed in IAXO and the alignment and commissioning takes place.

Item	Cost (MCHF)	Subtotals (MCHF)
Magnet		31.3
Eight coils based assembled toroid	28	
Magnet services	3.3	
Optics		16.0
Prototype Optic: Design, Fabrication, Calibration, Analysis	1.0	
IAXO telescopes (8 + 1 spare)	8.0	
Calibration	2.0	
Integration and alignment	5.0	
Detectors		5.8
Shielding & mechanics	2.1	
Readouts, DAQ electronics & computing	0.8	
Calibration systems	1.5	
Gas & vacuum	1.4	
Dome, base, services building and integration		3.7
Sum		**56.8**

Table 5: Estimated costs of the IAXO setup: magnet, optics and detectors. It does not include laboratory engineering, as well as maintenance & operation and physics exploitation of the experiment.

6.2 Site and Costs

IAXO will be an international experiment designed, constructed and operated by a collaboration of institutes from many different countries. The realization of the magnet system will be conducted by a subgroup of laboratories with expertise in superconducting magnets like CERN. The construction of its main components will be performed in industry while considering its large dimensions system assembly is foreseen on site. For weather protection IAXO will be housed in a light and confined structure, such as a tent or a dome of about 45 meter diameter. In addition, a relatively small side building is needed for the services units and a control room.

Table 6.1 shows the main costs of constructing IAXO. The main cost driver is the magnet, estimated in about 31.3 MCHF. The overal estimation, adding up to 56.8 MCHF, does not include laboratory engineering costs, nor maintenance and exploitation of the experiment during the subsequent data taking phases.

6.3 Collaboration expertise and know-how

The IAXO proto-collaboration is being formed at the moment. The signatories of the present LoI include groups that are currently active in axion and ALP experiments (most CAST groups, but also from other experiments like ALPS); plus new groups with worldwide expertise in the key technologies for IAXO (e.g. CERN, CEA-IRFU-SACM, DTU Space, etc.); as well as a number of expert groups in axion and ALP theory, phenomenology and their connection with cosmology and astrophysics, which are actively building up physics motivation for IAXO. In overall, they constitute a large fraction of the community working in axion experimentation and phenomenology worldwide. In table 6 we list all institutions in the authorlist with indication of their respective expertise. As shown they encompass all the needed know-how to support IAXO: axion and ALP theory, axion detection phenomenology, axion cosmology and astrophysics, superconducting magnets, x-ray optics, x-ray detection and low background techniques. If this Letter of Intent is supported by CERN, it is clear that a solid enough collaboration will be formed to carry out the project.

Group	(*)	Axion theory and phenomenology	Axion cosmology and astrophysics	Axion detection phenomenology	X-ray detectors	Low background techniques	X-ray optics	SC magnets and technology
South Carolina (US)	2	x		x				
CERN (Switzerland)	3			x				x
IPHT CEA/Saclay (France)	4	x	x					
IRFU CEA/Saclay (France)	1		x	x	x			x
U. Trieste (Italy)	5			x	x			
U. Zaragoza (Spain)	6			x	x	x		
LLNL (US)	7			x			x	
LBNL (US)	8			x				x
Dogus U. (Turkey)	9			x				
U. Haifa (Israel)	10		x					
DTU-Space (Denmark)	11						x	
St. Petersburg NPI (Russia)	12	x		x				
U. Bonn (Germany)	13				x			
DESY Hamburg (Germany)	14	x		x		x	x	x
U. Thessaloniki (Greece)	15			x				
RCLTMS Kyoto U. (Japan)	30			x				
NCSR Demokritos (Greece)	16			x	x			
U. Valencia (Spain)	17							
INR Moscow (Russia)	18	x		x				
Ben Gurion U. (Israel)	19	x						
Columbia Astrophysics Lab (US)	20						x	
Kyoto U. (Japan)	21	x	x					
TU-Darmstadt (Germany)	22			x	x			
ICE Barcelona (Spain)	24		x					
JAEA (Japan)	25			x				
U. Hamburg (Germany)	23		x					
U. Heidelberg (Germany)	26	x						
RBI Zagreb (Croatia)	27	x		x				
U. Tokyo (Japan)	28		x	x				
U. Rijeka (Croatia)	29			x	x			
MPI Munich (Germany)	31	x	x					
Tokyo I.T. (Japan)	32		x	x				
BNL (US)	33			x				
U. Florida (US)	34	x	x					
Berkeley (US)	35			x				x
Cape Town U. (South Africa)	36	x						
FNAL (US)	37			x	x			x
U. Patras (Greece)	38	x		x				

Table 6: (*) Check this number in the authorlist in the first page to see the full institution name.

7 Proposal and requests to CERN

IAXO is currently at the level of the Conceptual Design. The work performed up to now has largely occurred as an ancillary activity, when possible, of other projects of the groups involved (e.g. CAST). In order to make progress at the pace proposed in the timetable and reach the next milestone, the Technical Design Report (TDR), the IAXO project has to receive formal recognition and the nascent IAXO collaboration has to formally organize roles and responsibilities. IAXO activities towards the TDR has to receive specific support and resources, and the project must be acknowledged by the institutions involved. Work to explore funding strategies from a broad range of agencies has to start in earnest to secure approval and begin the initial project phases. Formal endorsement of the project by CERN is considered an essential first step. With this Letter of Intent to CERN we request such formal endorsement, as well as support for the near term steps. More specifically, we request that CERN:

- Endorses the scientific motivation of the proposal and gives approval for IAXO to become an official project at CERN.
- Endorses that the collaboration embarks in the design study of the experiment, aiming to complete a Technical Design Report, and carrying out the prototyping activities indicated in the preparatory phase of section 6 and table 29.
- Supports the CERN magnet group, providing the necessary manpower and resources, to carry out the magnet prototyping activities foreseen in the preparatory phase, i.e. the design and construction of the demo coil T0 described in section 4.1.9, as well as support the collaboration with site study, local link, and technical coordination of the project.

8 Conclusions

As its primary physics goal, IAXO will look for axions or ALPs originating in the Sun via the Primakoff conversion of the solar plasma photons. IAXO will substantially surpass the previous best search, that of CAST. In terms of signal-to-background ratio, IAXO will be about **4−5 orders of magnitude more sensitive** than CAST, which translates into a factor of ~ 20 in terms of the axion-photon coupling constant $g_{a\gamma}$. That is, this instrument will reach the few $\times 10^{-12}$ GeV^{-1} regime for a wide range of axion masses up to about 0.25 eV. While CAST was the first experimental search reaching, and slightly surpassing, the limit $g_{a\gamma} \lesssim 10^{-10}$ GeV $^{-1}$ in this mass range, and therefore started probing ALP parameter space allowed by astrophysics, IAXO will deeply enter into completely unexplored ALP and axion parameter space, as indicated by Fig. 25. At a minimum, IAXO will exclude a large region of the QCD axion phase space that has yet to be explored. If IAXO does discover a new pseudoscalar fundamental, it would be a groundbreaking result for particle physics.

More specifically, at high masses this experiment would explore a broad range of realistic axion models that accompany the Peccei-Quinn solution of the strong CP problem. Its sensitivity would cover axion models with masses down to the few meV range, superseding the SN 1987A energy loss limits on the axion mass. Axion models in this region are of high cosmological interest. As explained in previous sections, they are favored dark matter candidates and could compose all or part of the cold dark matter of the Universe. In non-standard cosmological scenarios, or in more generic ALP frameworks [46], the range of ALP parameters of interest as DM is enlarged and most of the region at reach by IAXO contains possible dark matter candidates. At much lower masses, below $\sim 10^{-7}$ eV, the region attainable by IAXO includes ALP parameters invoked repeatedly to explain anomalies in light propagation over astronomical distances. IAXO would provide a definitive test of this hypothesis.

Additional physics cases for IAXO include the possibility of detecting more specific models of axions or ALPs from the Sun. Most remarkable is the possibility to detect the flux of solar axions produced by axion-electron coupling g_{ae} induced phenomena. Although the existence of these production channels for standard axions is model-dependent, axions with a g_{ae} of few $\sim 10^{-13}$ have been invoked to solve the anomalous cooling observed in white dwarfs. For the first time, IAXO could directly measure the solar flux of axions produced by the very same mechanism invoked for WDs, with sufficient sensitivity to g_{ae} to test the hypothesis that the cooling of WD is enhanced by axion emission. Similarly IAXO will be sensitive to models of other proposed particles at the low energy frontier of particle physics, like hidden photons, or chameleons, scalars with an environment-dependent mass proposed in the context of dark energy models. Although still at an early stage of theoretical development, the possibility of directly testing the particle physics nature of dark energy is an exciting possibility.

Additional potential experimental programs for IAXO may include: 1) the search for axionic dark radiation, 2) the realization of microwave LSW experiments among different bores of the IAXO magnet, and 3) the direct detection of relic CDM axions or ALPs using microwave cavities or antennas in different configurations within the IAXO magnet. The physics potential of all these options is under study, but they certainly offer possibility for IAXO to become a first-class multi-purpose generic facility for axion and WISP research.

In summary, IAXO will allow to probe unexplored axion and ALPs parameter space, where not only theory, but interpretations of astrophysics phenomena may hint at the existence of new fundamental scalar or pseudoscalar particles. Any such particle discovered by IAXO would be a very viable candidate for a dark matter constituent. Hence IAXO might provide fundamental new insights into particle physics, astrophysics as well as cosmology.

It is important to stress the complementarity of the IAXO physics potential with that of axion haloscopes and purely laboratory based experiments. The haloscope ADMX has proven sensitivity to realistic axion models around masses of a few μeV, assuming the axion is the main DM component. However, the resonance condition restricts that sensitivity to a very narrow mass windows determined by the cavity geometry, and competitive sensitivity in other mass ranges is difficult (although progress is done continuously). Helioscopes, on the other hand, have mass-independent sensitivities up to very large values ($\sim$0.01 eV or up to $\sim$ 1 eV if buffer gas is used). Due to the $g_{a\gamma} - m_a$ proportionality, helioscopes, very specifically IAXO, can probe a large fraction of axion space at the high mass (above $\sim$ meV) range, i.e. very complementary to the regions reached by haloscopes. Measurements at laboratory experiments could complement IAXO results allowing to disentangle uncertainties from solar flux calculations and coupling strength. The near- and midterm future purely laboratory based experiments like ALPS-II (presently under preparation at DESY) will not be able to probe the whole parameter space accessible by IAXO, but will provide a considerable overlap.

The realistic prospects of both haloscopes at low masses and helioscopes at high masses still leaves a window at the sub meV level which is extremely challenging to explore experimentally and is highly motivated theoretically. New ideas are being put forward that could combine elements from both haloscopes and helioscopes (and other) searches. With additional equipment (like microwave cavities or antennas) IAXO could be converted into an axion haloscope experiment, and look also directly for axions or ALPs composing the galactic DM halo. This possibility is at an early stage of development, but has enormous potential, given the size and geometry of the IAXO magnet. The collaboration aims at consolidating a DM program with IAXO that could complement and extend the helioscope baseline program, and eventually access the remaining axion parameter space.

The complementarity between helioscopes, haloscopes and laboratory-based experiments goes beyond their corresponding sensitivity regions in the ALP parameter space. The sensitivity of a haloscope in the ALP parameter space assumes that the whole DM density is in the forms of axions, a non-guaranteed assumption, as axions (or ALPs) can exist but still be only a subdominant fraction of DM. Given that the haloscope signal is proportional to $g_{a\gamma}^2 n_a$ (n_a being the local DM halo axion density), a positive signal in a haloscope will not determine the value of $g_{a\gamma}$ nor the local density of axion DM [‡] independently, but only the product $g_{a\gamma}^2 n_a$. Helioscopes have the advantage that the Primakoff emission of axions or ALPs by the Sun is guaranteed and well quantified up to a multiplicative factor of $g_{a\gamma}^2$. Although eventually purely laboratory-based experiments are required to determine the coupling in a model independent way, a positive signal in a helioscope will provide a good independent determination of $g_{a\gamma}$. For some range of values, determination of m_a is also possible (by means of out-of-coherence runs with buffer gas). Obviously no information about DM density is available from a helioscope, but the mere identification of an ALP is sufficient to deduct that it will be –at least a subdominant– part of DM. Therefore the information on the axion or ALP properties derived from a positive signal in a haloscope and in a helioscope are equally important, and complementary. Strictly speaking, the determination of the local DM density of axions or ALPs can *only* be obtained by combining both a positive signal in a helioscope or laboratory experiment plus another in a haloscope. A potential course of action could be the following: after a positive detection in a helioscope with $g_{a\gamma}$ and m_a determined, a haloscope specifically tuned to the previously determined m_a could determine the relative fraction of axion DM.

It is important also to stress that a positive signal in a helioscope (as in a haloscope or a laboratory-based experiment) would constitute, by itself, a robust indication of the existence of a new particle. These

[‡]WIMP direct detection experiments have a similar limitation. Their WIMP signal is proportional to σn, where σ is the WIMP-nucleus crosssection and n is the WIMP local DM density.

experiments provide several means to cross-check the nature of a putative positive signal. In the case of IAXO, the correlation with the Sun, the variation of the magnetic field, or the alteration of the length of the magnet, among others, are factors that can be used to alter the signal detected in very specific ways, and provide tests that should unambiguously distinguish a real signal from other possible systematic effects.

In summary, axions are as well motivated candidates to constitute DM as WIMPs, although up to now they have received much less attention than the latter. However, for the time being there is no hint of supersymmetry at the LHC and also no clear signature for WIMPs in direct-detection experiments in spite of tremendous technical progress in both kinds of experiments. These facts together with advances in theory and phenomenology makes the search for axions (and by extension for ALPs) increasingly motivated. Axion searches and related R&D are currently being performed by a small but growing and active community. The diverse experimental approaches have a large degree of complementarity, and new developments and ideas are constantly proposed and studied. Among these approaches the axion helioscope stands out as the most mature, technologically feasible and capable of being scaled in size. IAXO is one instantiation of a fourth-generation axion helioscope concept, one that envisions the construction of a dedicated magnet and x-ray optics to dramatically increase its sensitivity compared to CAST, currently the most powerful axion helioscope. IAXO also has the potential to serve as multi-purpose facility for generic axion and ALP research in the next decade.

References

[1] K. Baker, G. Cantatore, S. A. Cetin, M. Davenport, K. Desch, B. Döbrich, H. Gies, I. G. Irastorza, J. Jaeckel, A. Lindner, T. Papaevangelou, M. Pivovaroff, G. Raffelt, J. Redondo, A. Ringwald, Y. Semertzidis, A. Siemko, M. Sulc, A. Upadhye, and K. Zioutas, *The quest for axions and other new light particles*, *Annalen der Physik* **525** (2013), no. 6 A93–A99.

[2] H.-Y. Cheng, *The Strong CP Problem Revisited*, *Phys.Rept.* **158** (1988) 1.

[3] C. A. Baker, D. D. Doyle, P. Geltenbort, K. Green, M. G. D. van der Grinten, P. G. Harris, P. Iaydjiev, S. N. Ivanov, D. J. R. May, J. M. Pendlebury, J. D. Richardson, D. Shiers, and K. F. Smith, *Improved experimental limit on the electric dipole moment of the neutron*, *Phys. Rev. Lett.* **97** (Sep, 2006) 131801.

[4] R. D. Peccei and H. R. Quinn, *CP conservation in the Presence of Instantons*, *Phys. Rev. Lett.* **38** (1977) 1440–1443.

[5] R. D. Peccei and H. R. Quinn, *Constraints imposed by CP conservation in the presence of instantons*, *Phys. Rev.* **D16** (1977) 1791–1797.

[6] S. Weinberg, *A New Light Boson?*, *Phys. Rev. Lett.* **40** (1978) 223–226.

[7] F. Wilczek, *Problem of Strong P and T Invariance in the Presence of Instantons*, *Phys. Rev. Lett.* **40** (1978) 279–282.

[8] M. S. Turner, *Windows on the Axion*, *Phys. Rept.* **197** (1990) 67–97.

[9] J. E. Kim, *Light Pseudoscalars, Particle Physics and Cosmology*, *Phys.Rept.* **150** (1987) 1–177.

[10] J. E. Kim, *Weak Interaction Singlet and Strong CP Invariance*, *Phys. Rev. Lett.* **43** (1979) 103.

[11] M. A. Shifman, A. I. Vainshtein, and V. I. Zakharov, *Can Confinement Ensure Natural CP Invariance of Strong Interactions?*, *Nucl. Phys.* **B166** (1980) 493.

[12] M. Dine, W. Fischler, and M. Srednicki, *A Simple Solution to the Strong CP Problem with a Harmless Axion*, *Phys. Lett.* **B104** (1981) 199.

[13] A. R. Zhitnitsky, *On Possible Suppression of the Axion Hadron Interactions. (In Russian)*, *Sov. J. Nucl. Phys.* **31** (1980) 260.

[14] P. Sikivie, *Experimental tests of the invisible axion*, *Phys. Rev. Lett.* **51** (1983) 1415.

[15] G. Raffelt and L. Stodolsky, *Mixing of the Photon with Low Mass Particles*, *Phys.Rev.* **D37** (1988) 1237.

[16] L. Maiani, R. Petronzio, and E. Zavattini, *Effects of nearly massless, spin zero particles on light propagation in a magnetic field*, *Phys.Lett.* **B175** (1986) 359.

[17] G. G. Raffelt, *Particle Physics from Stars*, *Ann. Rev. Nucl. Part. Sci.* **49** (1999) 163–216, [`hep-ph/9903472`].

[18] P. Gondolo and G. Raffelt, *Solar neutrino limit on axions and keV-mass bosons*, *Phys.Rev.* **D79** (2009) 107301, [`arXiv:0807.2926`].

[19] G. G. Raffelt, *Astrophysical axion bounds diminished by screening effects*, *Phys. Rev.* **D33** (1986) 897.

[20] N. Viaux, M. Catelan, P. B. Stetson, G. G. Raffelt, J. Redondo, A. A. R. Valcarce, and A. Weiss, *Neutrino and axion bounds from the globular cluster m5 (ngc 5904)*, . in preparation. See talk at 9th Patras Workshop on Axions, WIMPs and WISPs (2013).

[21] A. Friedland, M. Giannotti, and M. Wise, *Constraining the Axion-Photon Coupling with Massive Stars*, *Phys.Rev.Lett.* **110** (2013) 061101, [`arXiv:1210.1271`].

[22] G. G. Raffelt, *Axion constraints from white dwarf cooling times*, *Phys. Lett.* **B166** (1986) 402.

[23] J. Isern, E. Garcia-Berro, S. Torres, and S. Catalan, *Axions and the cooling of white dwarf stars*, *Astrophys.J* **682** (2008) L109, [`arXiv:0806.2807`].

[24] J. Isern, S. Catalan, E. Garcia-Berro, and S. Torres, *Axions and the white dwarf luminosity function*, *J.Phys.Conf.Ser.* **172** (2009) 012005, [`arXiv:0812.3043`].

[25] B. E. Melendez and M. M. M. Bertolami, *Revisiting the impact of axions in the cooling of white dwarfs*, . in preparation.

[26] G. G. Raffelt, *Astrophysical axion bounds*, *Lect.Notes Phys.* **741** (2008) 51–71, [`hep-ph/0611350`].

[27] H. Umeda, N. Iwamoto, S. Tsuruta, L. Qin, and K. Nomoto, *Axion mass limits from cooling neutron stars*, `astro-ph/9806337`.

[28] J. Keller and A. Sedrakian, *Axions from cooling compact stars*, *Nucl.Phys.* **A897** (2013) 62–69, [`arXiv:1205.6940`].

[29] **Planck** Collaboration, P. Ade *et. al.*, *Planck 2013 results. XVI. Cosmological parameters*, `arXiv:1303.5076`.

[30] H. Baer, A. Lessa, and W. Sreethawong, *Coupled Boltzmann calculation of mixed axion/neutralino cold dark matter production in the early universe*, *JCAP* **1201** (2012) 036, [`arXiv:1110.2491`].

[31] K. J. Bae, H. Baer, and A. Lessa, *Implications of mixed axion/neutralino dark matter for the Cosmic Frontier: a Snowmass whitepaper*, `arXiv:1306.2986`.

[32] O. Erken, P. Sikivie, H. Tam, and Q. Yang, *Cosmic axion thermalization*, *Phys.Rev.* **D85** (2012) 063520, [`arXiv:1111.1157`].

[33] P. Sikivie, *Evidence for ring caustics in the Milky Way*, *Phys.Lett.* **B567** (2003) 1–8, [`astro-ph/0109296`].

[34] S. Hannestad, A. Mirizzi, G. G. Raffelt, and Y. Y. Wong, *Neutrino and axion hot dark matter bounds after WMAP-7*, *JCAP* **1008** (2010) 001, [`arXiv:1004.0695`].

[35] M. Archidiacono, S. Hannestad, A. Mirizzi, G. Raffelt, and Y. Y. Y. Wong, *Axion hot dark matter bounds after Planck*, `arXiv:1307.0615`.

[36] P. Sikivie, *Axion cosmology*, *Lect.Notes Phys.* **741** (2008) 19–50, [`astro-ph/0610440`].

[37] O. Wantz and E. P. S. Shellard, *Axion Cosmology Revisited*, *Phys. Rev.* **D82** (2010) 123508, [`arXiv:0910.1066`].

[38] K. J. Bae, J.-H. Huh, and J. E. Kim, *Update of axion CDM energy*, *JCAP* **0809** (2008) 005, [`arXiv:0806.0497`].

[39] L. Visinelli, *Axions in Cold Dark Matter and Inflation Models*, `arXiv:1111.5281`.

[40] M. Tegmark, A. Aguirre, M. Rees, and F. Wilczek, *Dimensionless constants, cosmology and other dark matters*, *Phys.Rev.* **D73** (2006) 023505, [`astro-ph/0511774`].

[41] C. Hagmann, S. Chang, and P. Sikivie, *Axion radiation from strings*, *Phys.Rev.* **D63** (2001) 125018, [`hep-ph/0012361`].

[42] T. Hiramatsu, M. Kawasaki, K. Saikawa, and T. Sekiguchi, *Production of dark matter axions from collapse of string-wall systems*, *Phys.Rev.* **D85** (2012) 105020, [`arXiv:1202.5851`].

[43] A. D. Linde, *Inflation and axion cosmology*, *Phys. Lett.* **B201** (1988) 437.

[44] M. P. Hertzberg, M. Tegmark, and F. Wilczek, *Axion cosmology and the energy scale of inflation*, *Phys. Rev.* **D78** (2008) 083507, [`arXiv:0807.1726`].

[45] L. Visinelli and P. Gondolo, *Axion cold dark matter in nonstandard cosmologies*, *Physical Review D* **81** (Mar., 2010).

[46] P. Arias, D. Cadamuro, M. Goodsell, J. Jaeckel, J. Redondo, *et. al.*, *WISPy Cold Dark Matter*, *JCAP* **1206** (2012) 013, [`arXiv:1201.5902`].

[47] J. Jaeckel and A. Ringwald, *The Low-Energy Frontier of Particle Physics*, *Annual Review of Nuclear and Particle Science* **60** (Nov., 2010) 405–437.

[48] E. Masso and R. Toldra, *On a Light Spinless Particle Coupled to Photons*, *Phys. Rev.* **D52** (1995) 1755–1763, [`hep-ph/9503293`].

[49] A. Ringwald, *Exploring the Role of Axions and Other WISPs in the Dark Universe*, *Phys.Dark Univ.* **1** (2012) 116–135, [`arXiv:1210.5081`].

[50] A. Arvanitaki, S. Dimopoulos, S. Dubovsky, N. Kaloper, and J. March-Russell, *String Axiverse*, *Phys.Rev.* **D81** (2010) 123530, [`arXiv:0905.4720`].

[51] M. Cicoli, M. Goodsell, A. Ringwald, M. Goodsell, and A. Ringwald, *The type IIB string axiverse and its low-energy phenomenology*, *JHEP* **1210** (2012) 146, [`arXiv:1206.0819`].

[52] A. Ringwald, *Searching for axions and ALPs from string theory*, `arXiv:1209.2299`.

[53] L. Okun, *Limits Of Electrodynamics: Paraphotons?*, *Sov.Phys.JETP* **56** (1982) 502.

[54] B. Holdom, *Two U(1)'s and Epsilon Charge Shifts*, *Phys.Lett.* **B166** (1986) 196.

[55] S. Davidson and M. E. Peskin, *Astrophysical bounds on millicharged particles in models with a paraphoton*, *Phys. Rev.* **D49** (1994) 2114–2117, [`hep-ph/9310288`].

[56] S. M. Carroll, *Quintessence and the rest of the world*, *Phys. Rev. Lett.* **81** (1998) 3067–3070, [`astro-ph/9806099`].

[57] P. Brax and K. Zioutas, *Solar Chameleons*, *Phys. Rev.* **D82** (2010) 043007, [`arXiv:1004.1846`].

[58] K. Ehret, M. Frede, S. Ghazaryan, M. Hildebrandt, E.-A. Knabbe, *et. al.*, *New ALPS Results on Hidden-Sector Lightweights*, *Phys.Lett.* **B689** (2010) 149–155, [`arXiv:1004.1313`].

[59] **CAST** Collaboration, S. Andriamonje *et. al.*, *An improved limit on the axion-photon coupling from the CAST experiment*, *JCAP* **0704** (2007) 010, [hep-ex/0702006].

[60] **CAST** Collaboration, E. Arik *et. al.*, *Probing eV-scale axions with CAST*, *JCAP* **0902** (2009) 008, [arXiv:0810.4482].

[61] **CAST** Collaboration, E. Arik *et. al.*, *Search for sub-ev mass solar axions by the cern axion solar telescope with* ^{3}He *buffer gas*, *Phys. Rev. Lett.* **107** (Dec, 2011) 261302.

[62] M. Arik, S. Aune, K. Barth, A. Belov, S. Borghi, *et. al.*, *CAST solar axion search with* ^{3}*He buffer gas: Closing the hot dark matter gap*, arXiv:1307.1985.

[63] S. Chang and K. Choi, *Hadronic axion window and the big bang nucleosynthesis*, *Phys.Lett.* **B316** (1993) 51–56, [hep-ph/9306216].

[64] M. A. Bershady, M. T. Ressell, and M. S. Turner, *Telescope search for multi-eV axions*, *Phys.Rev.Lett.* **66** (1991) 1398–1401.

[65] M. T. Ressell, *Limits to the radiative decay of the axion*, *Phys.Rev.* **D44** (1991) 3001–3020.

[66] M. Meyer, D. Horns, and M. Raue, *First lower limits on the photon-axion-like particle coupling from very high energy gamma-ray observation*, *Phys.Rev.* **D87** (2013) 035027, [arXiv:1302.1208].

[67] **HESS** Collaboration, A. Abramowski *et. al.*, *Constraints on axion-like particles with H.E.S.S. from the irregularity of the PKS 2155-304 energy spectrum*, *Phys.Rev.* **D** (2013) Submitted.

[68] **HESS** Collaboration, A. Abramowski *et. al.*, *Measurement of the extragalactic background light imprint on the spectra of the brightest blazars observed with H.E.S.S*, *Astron. Astrophys.* **550** (2013) [arXiv:1212.3409].

[69] **Fermi-LAT** Collaboration, M. Ackermann *et. al.*, *The Imprint of The Extragalactic Background Light in the Gamma-Ray Spectra of Blazars*, *Science* **338** (2012) 1190–1192, [arXiv:1211.1671].

[70] A. De Angelis, G. Galanti, and M. Roncadelli, *Relevance of axion-like particles for very-high-energy astrophysics*, *Phys.Rev.* **D84** (2011) 105030, [arXiv:1106.1132].

[71] D. Horns and M. Meyer, *Indications for a pair-production anomaly from the propagation of VHE gamma-rays*, *JCAP* **1202** (2012) 033, [arXiv:1201.4711].

[72] **HESS** Collaboration, F. Aharonian *et. al.*, *A Low level of extragalactic background light as revealed by gamma-rays from blazars*, *Nature* **440** (2006) 1018–1021, [astro-ph/0508073].

[73] **MAGIC** Collaboration, M. Teshima *et. al.*, *Discovery of Very High Energy Gamma-Rays from the Distant Flat Spectrum Radio Quasar 3C 279 with the MAGIC Telescope*, arXiv:0709.1475.

[74] **MAGIC** Collaboration, E. Aliu *et. al.*, *Very-High-Energy Gamma Rays from a Distant Quasar: How Transparent Is the Universe?*, *Science* **320** (2008) 1752, [arXiv:0807.2822].

[75] W. Essey and A. Kusenko, *A new interpretation of the gamma-ray observations of active galactic nuclei*, *Astropart.Phys.* **33** (2010) 81–85, [arXiv:0905.1162].

[76] D. S. Gorbunov, P. G. Tinyakov, I. I. Tkachev, and S. V. Troitsky, *Testing the correlations between ultra-high-energy cosmic rays and BL Lac type objects with HiRes stereoscopic data*, *JETP Lett.* **80** (2004) 145–148, [astro-ph/0406654].

[77] **HiRes** Collaboration, R. U. Abbasi *et. al.*, *Search for Cross-Correlations of Ultra–High-Energy Cosmic Rays with BL Lacertae Objects*, *Astrophys. J.* **636** (2006) 680–684, [astro-ph/0507120].

[78] C. Csaki, N. Kaloper, M. Peloso, and J. Terning, *Super-GZK photons from photon axion mixing*, *JCAP* **0305** (2003) 005, [hep-ph/0302030].

[79] A. De Angelis, O. Mansutti, M. Persic, and M. Roncadelli, *Photon propagation and the VHE gamma-ray spectra of blazars: how transparent is really the Universe?*, arXiv:0807.4246.

[80] M. Roncadelli, A. De Angelis, and O. Mansutti, *Evidence for a new light boson from cosmological gamma-ray propagation?*, *AIP Conf. Proc.* **1018** (2008) 147–156, [arXiv:0902.0895].

[81] M. Simet, D. Hooper, and P. D. Serpico, *The Milky Way as a Kiloparsec-Scale Axionscope*, *Phys. Rev.* **D77** (2008) 063001, [arXiv:0712.2825].

[82] M. Fairbairn, T. Rashba, and S. V. Troitsky, *Photon-axion mixing in the Milky Way and ultra-high-energy cosmic rays from BL Lac type objects - Shining light through the Universe*, arXiv:0901.4085.

[83] I. F. M. Albuquerque and A. Chou, *A Faraway Quasar in the Direction of the Highest Energy Auger Event*, *JCAP* **1008** (2010) 016, [arXiv:1001.0972].

[84] A. Mirizzi and D. Montanino, *Stochastic conversions of TeV photons into axion-like particles in extragalactic magnetic fields*, *JCAP* **0912** (2009) 004, [arXiv:0911.0015].

[85] D. Wouters and P. Brun, *Irregularity in gamma ray source spectra as a signature of axionlike particles*, *Phys.Rev.* **D86** (2012) 043005, [arXiv:1205.6428].

[86] D. Wouters and P. Brun, *Constraints on Axion-like Particles from X-Ray Observations of the Hydra Galaxy Cluster*, *Astrophys.J.* **772** (2013) 44, [arXiv:1304.0989].

[87] C. Burrage, A.-C. Davis, and D. J. Shaw, *Active Galactic Nuclei Shed Light on Axion-like- Particles*, *Phys. Rev. Lett.* **102** (2009) 201101, [arXiv:0902.2320].

[88] G. W. Pettinari and R. Crittenden, *On the Evidence for Axion-like Particles from Active Galactic Nuclei*, *Phys. Rev.* **D82** (2010) 083502, [arXiv:1007.0024].

[89] A. Payez, J. R. Cudell, and D. Hutsemekers, *Axions and polarisation of quasars*, *AIP Conf. Proc.* **1038** (2008) 211–219, [arXiv:0805.3946].

[90] N. Bassan, A. Mirizzi, and M. Roncadelli, *Axion-like particle effects on the polarization of cosmic high-energy gamma sources*, *JCAP* **1005** (2010) 010, [arXiv:1001.5267].

[91] A. Payez, J. Cudell, and D. Hutsemekers, *New polarimetric constraints on axion-like particles*, *JCAP* **1207** (2012) 041, [arXiv:1204.6187].

[92] A. H. Corsico, L. G. Althaus, M. M. M. Bertolami, A. D. Romero, E. Garcia-Berro, *et. al.*, *The rate of cooling of the pulsating white dwarf star G117−B15A: a new asteroseismological inference of the axion mass*, arXiv:1205.6180.

[93] A. H. Corsico, L. G. Althaus, A. D. Romero, A. S. Mukadam, E. Garcia-Berro, *et. al.*, *An independent limit on the axion mass from the variable white dwarf star R548*, *JCAP* **1212** (2012) 010, [arXiv:1211.3389].

[94] J. Hewett, H. Weerts, R. Brock, J. Butler, B. Casey, *et. al.*, *Fundamental Physics at the Intensity Frontier*, arXiv:1205.2671. Report of the Workshop on the Intensity Frontier held December 2011 in Rockville, MD.

[95] G. G. Raffelt, J. Redondo, and N. V. Maira, *The meV mass frontier of axion physics*, *Phys.Rev.* **D84** (2011) 103008, [arXiv:1110.6397].

[96] S. J. Asztalos *et. al.*, *Large-scale microwave cavity search for dark-matter axions*, *Phys. Rev.* **D64** (2001) 092003.

[97] S. J. Asztalos *et. al.*, *An Improved RF Cavity Search for Halo Axions*, *Phys. Rev.* **D69** (2004) 011101, [astro-ph/0310042].

[98] S. Asztalos, R. Bradley, G. Carosi, J. Clarke, C. Hagmann, *et. al.*, *The axion dark-matter eXperiment: Results and plans*, .

[99] A. Martin, O. Baker, J. Hirshfield, Y. Jiang, S. Kazakov, *et. al.*, *Preliminary results from the Yale microwave cavity experiment*, .

[100] O. K. Baker, M. Betz, F. Caspers, J. Jaeckel, A. Lindner, A. Ringwald, Y. Semertzidis, P. Sikivie, and K. Zioutas, *Prospects for searching axionlike particle dark matter with dipole, toroidal, and wiggler magnets*, *Phys. Rev. D* **85** (Feb, 2012) 035018.

[101] I. G. Irastorza and J. A. Garcia, *Direct detection of dark matter axions with directional sensitivity*, *JCAP* **1210** (2012) 022, [arXiv:1207.6129].

[102] D. Horns, J. Jaeckel, A. Lindner, A. Lobanov, J. Redondo, *et. al.*, *Searching for WISPy Cold Dark Matter with a Dish Antenna*, *JCAP* **1304** (2013) 016, [arXiv:1212.2970].

[103] K. van Bibber, P. M. McIntyre, D. E. Morris, and G. G. Raffelt, *Design for a practical laboratory detector for solar axions*, *Phys. Rev.* **D39** (1989) 2089.

[104] W. Buchmüller and F. Hoogeveen, *Coherent production of light scalar particles in Bragg scattering*, *Phys.Lett.* **B237** (1990) 278.

[105] E. A. Paschos and K. Zioutas, *A Proposal for solar axion detection via Bragg scattering*, *Phys. Lett.* **B323** (1994) 367–372.

[106] R. J. Creswick *et. al.*, *Theory for the direct detection of solar axions by coherent Primakoff conversion in germanium detectors*, *Phys. Lett.* **B427** (1998) 235–240, [hep-ph/9708210].

[107] **SOLAX** Collaboration, I. Avignone, F. T. *et. al.*, *Experimental Search for Solar Axions via Coherent Primakoff Conversion in a Germanium Spectrometer*, *Phys. Rev. Lett.* **81** (1998) 5068–5071, [astro-ph/9708008].

[108] **COSME** Collaboration, A. Morales *et. al.*, *Particle Dark Matter and Solar Axion Searches with a small germanium detector at the Canfranc Underground Laboratory*, *Astropart. Phys.* **16** (2002) 325–332, [hep-ex/0101037].

[109] R. Bernabei *et. al.*, *Search for solar axions by Primakoff effect in NaI crystals*, *Phys. Lett.* **B515** (2001) 6–12.

[110] **CDMS** Collaboration, Z. Ahmed *et. al.*, *Search for Axions with the CDMS Experiment*, *Phys. Rev. Lett.* **103** (2009) 141802, [arXiv:0902.4693].

[111] E. Armengaud, Q. Arnaud, C. Augier, A. Benoit, A. Benoit, *et. al.*, *Axion searches with the EDELWEISS-II experiment*, arXiv:1307.1488.

[112] S. Cebrián *et. al.*, *Prospects of solar axion searches with crystal detectors*, *Astropart. Phys.* **10** (1999) 397–404, [astro-ph/9811359].

[113] F. T. Avignone, III, R. J. Creswick, and S. Nussinov, *The experimental challenge of detecting solar axion-like particles to test cosmological ALP-photon oscillation hypothesis*, arXiv:1002.2718.

[114] J. Redondo and A. Ringwald, *Light shining through walls*, *Contemp. Phys.* **52** (2011) 211–236, [arXiv:1011.3741].

[115] G. Mueller, P. Sikivie, D. B. Tanner, and K. van Bibber, *Detailed design of a resonantly-enhanced axion-photon regeneration experiment*, *Phys. Rev.* **D80** (2009) 072004, [arXiv:0907.5387].

[116] R. Bähre, B. Döbrich, J. Dreyling-Eschweiler, S. Ghazaryan, R. Hodajerdi, *et. al.*, *Any Light Particle Search II – Technical Design Report*, arXiv:1302.5647.

[117] A. Ljubicic, D. Kekez, Z. Krecak, and T. Ljubicic, *Search for hadronic axions using axioelectric effect*, *Phys.Lett.* **B599** (2004) 143–147, [hep-ex/0403045].

[118] A. Derbin, A. Kayunov, V. Muratova, D. Semenov, and E. Unzhakov, *Constraints on the axion-electron coupling for solar axions produced by Compton process and bremsstrahlung*, *Phys.Rev.* **D83** (2011) 023505, [arXiv:1101.2290].

[119] A. Derbin, V. Muratova, D. Semenov, and E. Unzhakov, *New limit on the mass of 14.4-keV solar axions emitted in an M1 transition in Fe-57 nuclei*, *Phys.Atom.Nucl.* **74** (2011) 596–602.

[120] A. Derbin, I. Drachnev, A. Kayunov, and V. Muratova, *Search for solar axions produced by Compton process and bremsstrahlung using axioelectric effect*, *JETP Lett.* **95** (2012) 379, [arXiv:1206.4142].

[121] S. Moriyama, *A Proposal to search for a monochromatic component of solar axions using Fe-57*, *Phys.Rev.Lett.* **75** (1995) 3222–3225, [hep-ph/9504318].

[122] M. Krcmar, Z. Krecak, M. Stipcevic, A. Ljubicic, and D. Bradley, *Search for invisible axions using Fe-57*, *Phys.Lett.* **B442** (1998) 38, [nucl-ex/9801005].

[123] M. Krcmar, Z. Krecak, A. Ljubicic, M. Stipcevic, and D. Bradley, *Search for solar axions using Li-7*, *Phys.Rev.* **D64** (2001) 115016, [hep-ex/0104035].

[124] **CAST** Collaboration, S. Andriamonje *et. al.*, *Search for 14.4-keV solar axions emitted in the M1-transition of Fe-57 nuclei with CAST*, *JCAP* **0912** (2009) 002, [arXiv:0906.4488].

[125] A. Derbin, S. Bakhlanov, A. Egorov, I. Mitropolsky, V. Muratova, *et. al.*, *Search for Solar Axions Produced by Primakoff Conversion Using Resonant Absorption by Tm-169 Nuclei*, *Phys.Lett.* **B678** (2009) 181–185, [arXiv:0904.3443].

[126] **Borexino** Collaboration, G. Bellini *et. al.*, *Search for Solar Axions Produced in* $p(d,{}^3\mathrm{He})\mathrm{A}$ *Reaction with Borexino Detector*, *Phys.Rev.* **D85** (2012) 092003, [arXiv:1203.6258].

[127] M. Schwarz, A. Lindner, J. Redondo, A. Ringwald, G. Wiedemann, *et. al.*, *Solar Hidden Photon Search*, arXiv:1111.5797.

[128] T. Mizumoto, R. Ohta, T. Horie, J. Suzuki, Y. Inoue, *et. al.*, *Experimental search for solar hidden photons in the eV energy range using kinetic mixing with photons*, arXiv:1302.1000.

[129] G. Rybka, M. Hotz, L. Rosenberg, S. Asztalos, G. Carosi, *et. al.*, *A Search for Scalar Chameleons with ADMX*, *Phys.Rev.Lett.* **105** (2010) 051801, [arXiv:1004.5160].

[130] H. An, M. Pospelov, and J. Pradler, *Dark Matter Detectors as Dark Photon Helioscopes*, arXiv:1304.3461.

[131] G. Carosi (coord.) *et. al.*, *Report of the Workshop Vistas on Axion Physics, held April 2012 in Seattle*, *to be published in Review of Modern Physics* (2013).

[132] B. Döbrich (coord.) *et. al.*, *Fundamental physics at low energies – The quest for axions and other new light particles*, *Input to the Open Call to the European Strategy for Particle Physics* (2012). Available at `https://indico.cern.ch/contributionDisplay.py?contribId=105&confId=175067`.

[133] J. Redondo, *paper in preparation*, .

[134] K. Barth, A. Belov, B. Beltran, H. Brauninger, J. Carmona, *et. al.*, *CAST constraints on the axion-electron coupling*, *JCAP* **1305** (2013) 010, [`arXiv:1302.6283`].

[135] **CAST** Collaboration, K. Zioutas *et. al.*, *First results from the CERN Axion Solar Telescope (CAST)*, *Phys. Rev. Lett.* **94** (2005) 121301, [`hep-ex/0411033`].

[136] D. M. Lazarus *et. al.*, *A Search for solar axions*, *Phys. Rev. Lett.* **69** (1992) 2333–2336.

[137] Y. Inoue *et. al.*, *Search for sub-electronvolt solar axions using coherent conversion of axions into photons in magnetic field and gas helium*, *Phys. Lett.* **B536** (2002) 18–23, [`astro-ph/0204388`].

[138] S. Moriyama *et. al.*, *Direct search for solar axions by using strong magnetic field and X-ray detectors*, *Phys. Lett.* **B434** (1998) 147, [`hep-ex/9805026`].

[139] Y. Inoue *et. al.*, *Search for solar axions with mass around 1 eV using coherent conversion of axions into photons*, *Phys. Lett.* **B668** (2008) 93–97, [`arXiv:0806.2230`].

[140] K. Zioutas *et. al.*, *A decommissioned LHC model magnet as an axion telescope*, *Nucl. Instrum. Meth.* **A425** (1999) 480–489, [`astro-ph/9801176`].

[141] M. Kuster *et. al.*, *The X-ray Telescope of CAST*, *New J. Phys.* **9** (2007) 169, [`physics/0702188`].

[142] P. Abbon *et. al.*, *The Micromegas detector of the CAST experiment*, *New J. Phys.* **9** (2007) 170, [`physics/0702190`].

[143] I. G. Irastorza, F. Avignone, S. Caspi, J. Carmona, T. Dafni, *et. al.*, *Towards a new generation axion helioscope*, *JCAP* **1106** (2011) 013, [`arXiv:1103.5334`].

[144] **ATLAS** Collaboration, *ATLAS endcap toroids: Technical design report*, .

[145] H. H. J. ten Kate, *The atlas superconducting magnet system at the large hadron collider*, *Physica C* **468** (2008), no. 15-20 2137–2142.

[146] H. H. J. ten Kate, *Atlas magnet system nearing completion*, *IEEE Trans. Appl. Supercond.* **18** (2008), no. 2 352–355.

[147] A. Hervé, D. Campi, B. Curé, P. Fabbricatore, A. Gaddi, F. Kircher, and S. Sgobba, *Experience gained from the construction, test and operation of the large 4-t cms coil*, *IEEE Trans. Appl. Supercond.* **18** (2008), no. 2 346–351.

[148] A. Ballarino, *Hts current leads: Performance overview in different operating modes*, *Applied Superconductivity, IEEE Transactions on* **17** (2007), no. 2 2282–2285.

[149] R. Petre and P. J. Serlemitsos, *Conical imaging mirrors for high-speed x-ray telescopes*, *Applied Optics* **24** (1985) 1833–1837.

[150] P. J. Serlemitsos, L. Jalota, Y. Soong, H. Kunieda, Y. Tawara, and many more, *The x-ray telescope on board asca*, *Publications of the Astronomical Society of Japan* **47** (1995) 105–114.

[151] F. E. Christensen, B. Madsen, A. Hornstrup, S. Abdali, P. Frederiksen, and many more, *X-ray calibration of the sodart flight telescopes*, *Proceedings of the SPIE* **3113** (1997) 294–306.

[152] Y. Ogasaka, J. Tueller, K. Yamashita, P. Serlemitsos, R. Shibata, K. Tamura, A. Furuzawa, T. Miyazawa, R. Takahashi, M. Sakashita, K. Shimoda, Y. Tawara, H. Kunieda, T. Okajima, H. Krimm, S. Barthelmy, Y. Soong, K.-W. Chan, S. Owens, M. Rex, E. Chapin, and M. Devlin, *First light of a hard-x-ray imaging experiment: the infocus balloon flight*, *Proceedings of the SPIE* **5900** (2005) 59000R–59000R–8.

[153] P. Serlemitsos, Y. Soong, K.-W. Chan, T. Okajima, J. Lehan, and many more, *The x-ray telescope onboard suzaku*, *Publications of the Astronomical Society of Japan* **59** (2007) 9–21.

[154] Y. Ogasaka, H. Kunieda, T. Miyazawa, P. Serlemitsos, Y. Soong, and many more, *The next x-ray telescope system: status update*, *Proceedings of the SPIE* **7011** (2008) 70110P–1–8.

[155] S. Labov, *Figured grazing incidence mirrors from reheated float glass*, *Applied Optics* **27** (1988) 1465–1469.

[156] F. A. Harrison, F. E. Christensen, W. Craig, C. Hailey, and m. more, *Development of the heft and nustar focusing telescopes*, *Experimental Astronomy* **20** (2005) 131.

[157] F. A. Harrison, W. W. Craig, F. E. Christensent, C. J. Hailey, and m. more, *The nuclear spectroscopic telescope array (nustar) high-energy x-ray mission*, *Astrophysical Journal* **770** (2013) 103.

[158] A. Winter, M. Vongehr, and P. Friedrich, *Light weight optics made by glass thermal forming for future x-ray telescopes*, *Proceedings of the SPIE* **7732** (2010) 77320B–1–7.

[159] W. W. Zhang, M. Atanassova, M. Biskach, P. N. Blake, G. Byron, K. W. Chan, and many more, *Mirror technology development for the international x-ray observatory mission (ixo)*, *Proceedings of the SPIE* **7732** (2010) 77321G–1–8.

[160] M. J. Collon, R. Gunther, M. Ackermann, R. Partapsing, G. Vacanti, and many more, *Silicon pore x-ray optics for ixo*, *Proceedings of the SPIE* **7732** (2010) 77321F–1–6.

[161] F. Jansen, D. Lumb, B. Altieri, J. Clavel, M. Ehle, and many more, *Xmm-newton observatory - i. the spacecraft and operations*, *Astronomy and Astrophysics* **365** (2001) L1–L61.

[162] O. Citterio *et. al.*, *Optics for the x-ray imaging concentrators aboard the x-ray astronomy satellite SAX*, *App Opt* **27** (1988) 1470–1475.

[163] W. J. Egle, J. Altmann, P. Kaufmann, H. Muenker, and G. Derst, *Mirror system for the german x-ray satellite abrixas: Ii. design and mirror development*, *Proceedings of the SPIE* **3444** (1998) 359–368.

[164] B. D. Ramsey *et. al.*, *First images from HERO, a hard x-ray focusing telescope*, *Astrophys J* **568** (2002) 432–435.

[165] R. Giacconi *et. al.*, *The Einstein (HEAO 2) x-ray observatory*, *Astrophys J* **230** (1979) 540–550.

[166] J. Trumper, *The rosat mission*, *Advances in Space Research* **2** (1983) 241–249.

[167] M. Weisskopf, H. D. Tananbaumb, L. V. Van Speybroeck, and S. L. O'Dell, *Chandra x-ray observatory (cxo): overview*, *Proceedings SPIE* **4012** (2000) 2–16.

[168] K. K. Madsen, F. Harrison, P. H. Mao, F. E. Christensen, C. P. Jensen, N. Brjenholt, J. Koglin, and M. J. Pivovaroff, *Optimizations of pt/sic and w/si multilayers for the nuclear spectroscopic telescope array*, *Proceedings of the SPIE* **7437** (2009) 743716–1.

[169] D. L. Windt, *IMD: Software for modeling the optical properties of multilayer films*, *Computers Phys* **12** (1998) 360–370.

[170] I. Irastorza, J. Castel, S. Cebrián, T. Dafni, G. Fanourakis, E. Ferrer-Ribas, D. Fortuo, L. Esteban, J. Galán, J. García, A. Gardikiotis, J. Garza, T. Geralis, I. Giomataris, H. Gómez, D. Herrera, F. Iguaz, G. Luzón, J. Mols, A. Ortiz, T. Papaevangelou, A. Rodríguez, J. Ruz, L. Segui, A. Tomás, T. Vafeiadis, and S. Yildiz, *Status of R&D on micromegas for rare event searches : The T-REX project*, *EAS Publications Series* **53** (0, 2012) 147–154.

[171] T. Dafni, S. Aune, S. Cebrian, G. Fanourakis, E. Ferrer-Ribas, *et. al.*, *Rare event searches based on micromegas detectors: The T-REX project*, *J.Phys.Conf.Ser.* **375** (2012) 022003.

[172] T. Dafni, S. Aune, J. Castel, S. Cebrián, G. Fanourakis, *et. al.*, *The T-REX project: Micromegas for rare event searches*, *J.Phys.Conf.Ser.* **347** (2012) 012030.

[173] Y. Giomataris, P. Rebourgeard, J. P. Robert, and G. Charpak, *MICROMEGAS: A high-granularity position-sensitive gaseous detector for high particle-flux environments*, *Nucl. Instrum. Meth.* **A376** (1996) 29–35.

[174] I. Giomataris *et. al.*, *Micromegas in a bulk*, *Nucl. Instrum. Meth.* **A560** (2006) 405–408, [`physics/0501003`].

[175] I. Giomataris and J. D. Vergados, *Neutrinos in a spherical box*, *Phys. Atom. Nucl.* **67** (2004) 1097–1106.

[176] S. Andriamonje, D. Attie, E. Berthoumieux, M. Calviani, P. Colas, *et. al.*, *Development and performance of Microbulk Micromegas detectors*, *JINST* **5** (2010) P02001.

[177] S. Cebrián *et. al.*, *Micromegas readouts for double beta decay searches*, *JCAP* **1010** (2010) 010, [`arXiv:1009.1827`].

[178] S. Cebrián *et. al.*, *Radiopurity of Micromegas readout planes*, *Astropart. Phys.* **34** (2011) 354–359, [`arXiv:1005.2022`].

[179] P. Baron, D. Calvet, E. Delagnes, X. de la Broise, A. Delbart, *et. al.*, *AFTER, an ASIC for the readout of the large T2K time projection chambers*, *IEEE Trans.Nucl.Sci.* **55** (2008) 1744–1752.

[180] P. Baron, S. Anvar, B. Blank, J. Chavas, E. Delagnes, F. Druillole, P. Hellmuth, L. Nalpas, J. Pedroza, J. Pibernat, E. Pollacco, A. Rebii, N. Usher, *et. al.*, *AGET, the Get Front-End ASIC, for the readout of the Time Projection Chambers used in Nuclear Physic Experiments*, *Nuclear Science Symposium Conference Record* (2011).

[181] J. Kaminski, C. Krieger, Y. Bilevych, T. Krautscheid, and K. Desch, *'GridPix as a candidate for the future of CAST', submitted to the conference proceedings of the sixth symposium on large TPCs for low energy rare event detection', 2012, Paris, published in JPCS*, .

[182] M. Chefdeville, H. van der Graaf, S. van der Putten, J. Timmermans, J. Visschers, *et. al.*, *An electron-multiplying 'Micromegas' grid made in silicon wafer post-processing technology*, *Nucl.Instrum.Meth.* **A556** (2006) 490–494.

[183] X. Llopart, R. Ballabriga, M. Campbell, L. Tlustos, and W. Wong, *Timepix, a 65k programmable pixel readout chip for arrival time, energy and/or photon counting measurements*, *Nuclear Instruments and Methods in Physics Research Section A: Accelerators, Spectrometers, Detectors and Associated Equipment* **581** (2007), no. 1–2 485 – 494. Proceedings of the 11th International Vienna Conference on Instrumentation VCI 2007.

[184] C. Krieger, J. Kaminski, and K. Desch, *'InGrid-based X-ray detector for low background searches', submitted to Nucl. Instr. and Meth.*, .

[185] K. Irwin and G. Hilton, *Transition-edge sensors*, in *Cryogenic Particle Detection*, vol. 99 of *Topics in Applied Physics*, pp. 63–149. Springer-Verlag Berlin, Heidelberger Platz 3, D-14197 Berlin, Germany, 2005.

[186] A. Miller, S. Nam, J. Martinis, and A. Sergienko, *Demonstration of a low-noise near-infrared photon counter with multiphoton discrimination*, *Applied Physics Letters* **83** (Jul 28, 2003) 791–793.

[187] A. E. Lita, A. J. Miller, and S. W. Nam, *Counting near-infrared single-photons with 95% efficiency*, *Optics Express* **16** (MAR 3, 2008) 3032–3040.

[188] G. Angloher, M. Bauer, I. Bavykina, A. Bento, A. Brown, C. Bucci, C. Ciemniak, C. Coppi, G. Deuter, F. von Feilitzsch, D. Hauff, S. Henry, P. Huff, J. Imber, S. Ingleby, C. Isaila, J. Jochum, M. Kiefer, M. Kimmerle, H. Kraus, J. C. Lanfranchi, R. F. Lang, B. Majorovits, M. Malek, R. McGowan, V. B. Mikhailik, E. Pantic, F. Petricca, S. Pfister, W. Potzel, F. Proebst, W. Rau, S. Roth, K. Rottler, C. Sailer, K. Schaeffner, J. Schmaler, S. Scholl, W. Seidel, L. Stodolsky, A. J. B. Tolhurst, I. Usherov, and W. Westphal, *Commissioning run of the CRESST-II dark matter search*, *Astroparticle Physics* **31** (MAY, 2009) 270–276.

[189] P. De Korte, H. Hoevers, J. Den Herder, J. Bleeker, W. Bergmann Tiest, M. Bruijn, M. Ridder, R. Wiegerink, J. Kaastra, J. Van der Kuur, and W. Mels, *A tes x-ray microcalorimeter-array for imaging spectroscopy*, in *Proceedings of SPIE - The International Society for Optical Engineering*, vol. 4851, (Bellingham, WA, USA), pp. 779–789, The International Society for Optical Engineering, August, 2002.

[190] S. J. Smith, S. R. Bandler, R. P. Brekosky, A.-D. Brown, J. A. Chervenak, M. E. Eckart, E. Figueroa-Feliciano, F. M. Finkbeiner, R. L. Kelley, C. A. Kilbourne, F. S. Porter, and J. E. Sadleir, *Development of Position-Sensitive Transition-Edge Sensor X-Ray Detectors*, *IEEE Transactions on Applied Superconductivity* **19** (JUN, 2009) 451–455. Applied Superconductivity Conference, Chicago, IL, AUG 17-22, 2008.

[191] **DAMIC** Collaboration, J. Barreto *et. al.*, *Direct Search for Low Mass Dark Matter Particles with CCDs*, *Phys.Lett.* **B711** (2012) 264–269, [`arXiv:1105.5191`].

[192] K. Baker, A. Lindner, A. Upadhye, and K. Zioutas, *A chameleon helioscope*, `arXiv:1201.0079`.

[193] J. Isern, M. Hernanz, and E. Garcia-Berro, *Axion cooling of white dwarfs*, *Astrophys.J* **392** (1992) L23–L25.

[194] J. Isern, E. Garcia-Berro, L. Althaus, and A. Corsico, *Axions and the pulsation periods of variable white dwarfs revisited*, *Astron. Astrophys.* **512** (2010), no. A86 86, [`arXiv:1001.5248`].

[195] J. Isern, L. Althaus, S. Catalan, A. Corsico, E. Garcia-Berro, *et. al.*, *White dwarfs as physics laboratories: the case of axions*, `arXiv:1204.3565`.

[196] B. Melendez, M. M. Bertolami, and L. Althaus, *Revisiting the Impact of Axions in the Cooling of White Dwarfs*, `arXiv:1210.0263`.

[197] G. G. Raffelt, *Core mass at the helium flash from observations and a new bound on neutrino electromagnetic properties*, *Astrophys.J.* **365** (1990) 559.

[198] G. Raffelt and A. Weiss, *Red giant bound on the axion - electron coupling revisited*, *Phys.Rev.* **D51** (1995) 1495–1498, [`hep-ph/9410205`].

[199] S. N. Gninenko and J. Redondo, *On search for eV hidden sector photons in Super-Kamiokande and CAST experiments*, *Phys.Lett.* **B664** (2008) 180–184, [`arXiv:0804.3736`].

[200] P. Brax, A. Lindner, and K. Zioutas, *Detection prospects for solar and terrestrial chameleons*, *Phys.Rev.* **D85** (2012) 043014, [`arXiv:1110.2583`].

[201] J. P. Conlon and M. C. D. Marsh, *The Cosmophenomenology of Axionic Dark Radiation*, `arXiv:1304.1804`.

[202] J. Jaeckel and J. Redondo, *An Antenna for Directional Detection of WISPy Dark Matter*, `arXiv:1307.7181`.

[203] M. Betz and F. Caspers, *A microwave paraphoton and axion detection experiment with 300 dB electromagnetic shielding at 3 GHz*, *Conf.Proc. IPAC 2012* (2012) 3320–3322, [`arXiv:1207.3275`].

[204] M. Cicoli, J. P. Conlon, and F. Quevedo, *Dark Radiation in LARGE Volume Models*, *Phys.Rev.* **D87** (2013) 043520, [`arXiv:1208.3562`].

[205] T. Higaki and F. Takahashi, *Dark Radiation and Dark Matter in Large Volume Compactifications*, *JHEP* **1211** (2012) 125, [`arXiv:1208.3563`].

[206] T. Higaki, K. Nakayama, and F. Takahashi, *Cosmological constraints on axionic dark radiation from axion-photon conversion in the early Universe*, `arXiv:1306.6518`.

[207] J. P. Conlon and M. C. D. Marsh, *Searching for a 0.1-1 keV Cosmic Axion Background*, `arXiv:1305.3603`.